Constraints on Cr-PGE Mineralisation Models: Geochemical and Petrological Studies in the Middle Group 1 and 3 Chromitites, Western Limb, Bushveld Complex, South Africa

A thesis

submitted in fulfilment of the requirements for the degree of

Master of Science

Of

Rhodes University

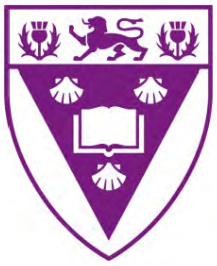

By

Yogendran Arunachellan

BSc. Hons (Rhodes University)

Abstract

The Bushveld Complex in South Africa has been of interest in various research groups for decades, along with diverse theories regarding its origin, formation, and emplacement. These theories include magma mixing, contamination, and changes in the chamber's ephemeral parameters. Of interest for our current study is the formation of the middle group chromitite layers in the Western Limb. In this research, we aimed to determine the emplacement mechanism of the MG group chromitites by scrutinising the MG 1 and MG 3 layers. In core KD 151, the focus was placed on the MG 3 and MG 1 chromitite layers and their associated silicate rocks; on these regions of the core, time was spent for detailed observations. The differences and similarities of these layers were explored as the study advanced. The objectives were to determine the *in-situ* or proximal crystallisation of the chromitite by evaluating mineral textures and compositions. This required that we determine the characteristics of the immediate HW (hanging wall) and FW (footwall) to these chromitites, with insights into the relationship that anorthositic zones may offer and examine the PGE profiles of the chromitites in contrasting lithological settings. The sampled borehole was in the Western Limb of the Bushveld Complex; the immediate HW, chromitite layers and FW were divided into sections (2.5 x 5 cm) along selected horizons for a microscale study.

The preliminary results of a study on the sub-economic Middle Group (MG) layers within the Critical Zone (CZ), contrasting the MG 1 (Lower CZ) and MG 3 (Upper CZ) chromitite layers of the Rustenburg Layered Suite of the Bushveld Complex, South Africa were analysed. The MG 3 and 1 suites of silicate rocks show disequilibrium textures between the pyroxenes and plagioclase, forming discontinuous olivine rims. These reaction rims are interpreted as products of magmatic aqueous fluid-facilitated reactions with minerals in a sub-solidus state. Deformation of the plagioclase was also noted in MG 1; this fracturing indicates either the transportation of these minerals or compaction by an overlying crystal mush.

The MG 3 package of plagioclase, pyroxene and chromite compositions range from An_{67-78}, En_{71-86} and Cr# of 68-84, respectively. The MG 1 package of plagioclase, pyroxene and chromite compositions are An_{64-91}, En_{79-88} and Cr# of 70-80, respectively. The Cu/Pd ratio decreases from the base of the FW as it approaches the base of the chromitite, then remains low within the chromitite layer and finally increases upwards in the HW. These trends are observed in both the MG 3 and 1 package, therefore not influenced by the sulphide control.

There is a decrease in both IPGE and PPGE upwards as the HW progresses into the chromitite. The FW levels of Ir and Ru increase upwards immediately adjacent to the FW contact, while Pd and Rh concentrations decrease. The whole-rock Mg# indicates a decrease in the MG 3 with a uniform increase in the HW and an erratic upward increase observed in the FW. The chondrite normalised PGE plots show a bell-shaped curve which is evident for the En content of the pyroxenes and the content of plagioclase with the highest values in the chromitite layer itself. The Cr# of the chromite decreases upwards with the highest values along the FW. The Cu/Pd ratio for MG 1 indicates chromitite control rather than sulphide control of the PGE. The whole-rock Mg# decreases in MG 1 with higher uniform values observed in the HW and FW.

The geochemical and petrological data from the MG group study revealed that in situ fractional crystallisation seems unlikely as the sole mechanism for their formation in the CZ. A model is suggested in which the migration and transport of a magmatic slurry type suspension with accompanying hydrous fluids would likely have resulted in the emplacement of these chromitite packages along with the PGE mineralisation of the chromitites.

Table of Contents

Dedication

Thank you, Iviwe Cwaita,

Melody Olivine Lunathi and

Mica Harvey Elinathi

Acknowledgements

I would like to thank the following people/institutes:

- Steve Prevec for being patient, secondly for providing the opportunity to follow a passion for research and thirdly for greatly assisting with the layout, interpretation and understanding of the data and the work we were doing
- Rhodes University slides preparation staff for providing good quality thin sections that allowed for accurate observations and analysis
- Geo Labs geoscience labs for good quality and timeous XRF and ICP-MS data
- Kea for her patience and great assistance in the running and understanding of E.M.P. samples
- Gelu Costin for his assistance with geochemical interpretations
- Xstrata Metals and Alloys for providing the core for sampling, access to the operations and industry knowledge
- Goonie Marsh for being a sounding board for some geochemical thoughts
- Rhodes University Geology Department for the administrative assistance and resources, along with coffee
- Rhodes University for the opportunity to complete this thesis
- Iviwe Arunachellan for her dedicated editing work and motivation
- The Almighty, for His guidance

Abbreviations

Mg#	Magnesium number	La	Lanthanum
An	Anorthite	Sm	Samarium
An#	Anorthite number	WR	Whole-rock
ICP-MS	Inductively coupled plasma mass spectrometry	Ppm	Parts per million
EPMA	Electron probe microanalysis	Ppb	Parts per billion
XRF	X-ray fluorescence	Fo	Forsterite
RLS	Rustenburg Layered Suite	Cr	Chromium
MORB	Mid Oceanic Ridge Basalt	REE	Rare earth elements
PGE	Platinum Group Elements	PGM	Platinum-group minerals
Pt	Platinum		
Pd	Palladium		
GDP	Gross Domestic Product		
opx	Orthopyroxene		
cpx	Clinopyroxene		
Os	Osmium		
Ir	Iridium		
Au	Gold		
S	Sulphur		
As	Arsenic		
Te	Tellurium		
En	Enstatite		
FW	Footwall		
HW	Hanging wall		
MG	Middle Group		
CZ	Critical Zone		
UCZ	Upper Critical Zone		
LCZ	Lower Critical Zone		

List of Figures

List of Tables

Chapter 1

Introduction

Being the most extensive layered igneous intrusion globally and endowed with mineral reserves, the Bushveld Complex has attracted the scientifically curious and economically motivated since its discovery. The Bushveld Complex has had geological scholars divided into various schools of thought regarding its source, the emplacement of its reefs and the formation of its world-class mineral deposits (Prevec, 2018). The country rocks of the Bushveld Complex are sedimentary, with ages ranging from 2.1-2.3 Ga (Eales and Cawthorn, 1996). This forms part of the Pretoria Group suite of rocks composed primarily of shales, conglomerates, and quartzites with volumetrically minor amounts of volcanic rocks (Kinnaird *et al.,* 2002). The areal coverage of the layered intrusion is ~400 x 300 km with an approximate thickness of 7-8 km (SACS, 1980). The complex is subdivided into the Rooiberg Group, the Rustenburg Layered Suite (RLS), the Rashoop Granophyre Suite and the Lebowa Granite Suite, as shown in Table 1.

Table 1. Sub-divisions and nomenclature of the Bushveld Complex. It is adapted from Johnson et al. (2006).

Main lithological unit	
Lebowa granite suite	Nebo, Makhutso, Klipkloof, Bobbejaankop and Verena Granites.
Rashoop granophyre suite	Stavoren and Diepkloof Granophyres, Rooikop Porphyritic Granite, Zwartbank Pseudogranophyre.
Rustenberg layered suite (RLS)	Upper Zone Main Zone Critical Zone Lower Zone Marginal Zone
Rooiberg group	Schrikkloof Formation, Kwaggasnek Formation, Damwal Formation, and the Dullstroom Formation

While all subdivisions make exciting studies, the RLS is of primary interest in this current study, wherein the suite comprises rock types that range from dunites and pyroxenites, gabbro and anorthosite to magnetite- and apatite-rich diorites (Johnson *et al.*, 2006). The RLS is divided spatially into limbs (or lobes): the northern, eastern, south-eastern, western, and far-western limbs. The RLS is further subdivided into five stratigraphic zones, as shown in Figure 1. These consist of the Marginal (0-800 m thick norite), Lower (800-1300 m of cyclic units of harzburgites, dunites and pyroxenites), Critical (1300-1800 m cyclic units of chromitites, pyroxenite, norites and anorthosites), Main (3000-3400 m norites, gabbronorites and anorthosites) and the Upper (2000-2800 m of magnetites, gabbronorites, anorthosites and diorites) Zones. The Critical Zone is further differentiated into the Lower and Upper Critical Zone. The Lower Critical Zone (LCZ) consists of 8 cyclic chromitite layers with related pyroxenites and harzburgites ranging from LG 1-7 and MG 1. The Upper Critical Zone (UCZ) is marked by cumulus plagioclase's first appearance, resulting in anorthositic layers. The UCZ also consists of 8 cyclic units of chromitites, pyroxenite and norites. The economic PGE bearing reefs occur between the UG 1 and Main Zone layer. The UG 2 and the Merensky Reef are mined.

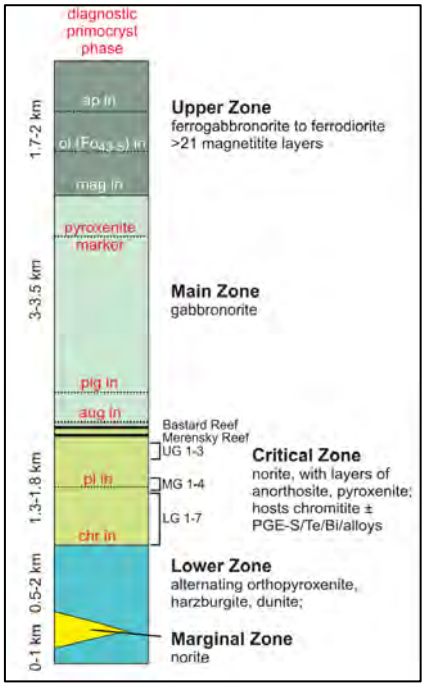

Figure 1. Simplified stratigraphy of the Bushveld Complex, showing the associated reefs and lithostratigraphic zones. Diagram is adapted from Prevec (2018).

1.1 Economic importance of the Bushveld Complex

The earliest recorded scientific evidence of PGE from the Bushveld Complex was in 1906, written by William Bettel (Cawthorn, 2006). This discovery was preceded by the announcement of chromium and iron ore by state geologist Prof GAP Molengraaf in an annual report in 1898 (Gräbe, 2014). The discovery of the Bushveld Complex piqued the interest of the academic community in South Africa and largely contributed to the economy. The role of the Bushveld Complex in South Africa's economy is and remains essential due to the mining contribution to GDP and employment figures (Lehohla, 2015). The ultramafic and mafic portion of the Bushveld Complex is conservatively estimated to have 68 % of the world's reserve of chromite and 56 % of platinum group elements with significant iron, nickel, and vanadium (Wilson, 1998). The felsic portion of the complex contains significant reserves of tin, fluorite, copper, magnesite and dimension stones (Wilson, 1998). The principal use of chromium is in the metallurgical industry. This accounts for 79 % of the total production, whereas the chemical industry uses 13 %, and the refractory industry uses 8 % (Papp and Lipin, 2011). Figure 2 shows that South Africa is a global leader in resources and reserves of chromitite, with a steady increase in chromium production worldwide (Figure 3). The source for these reserves originates from the Bushveld Complex.

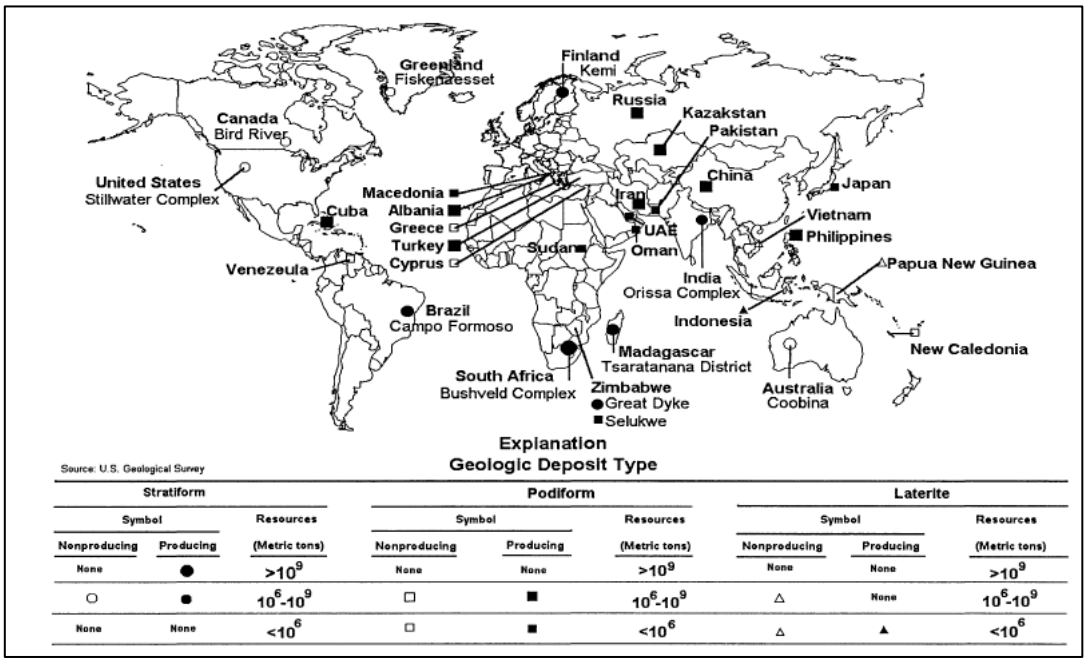

Stratiform			Podiform			Laterite		
Symbol		Resources	Symbol		Resources	Symbol		Resources
Nonproducing	Producing	(Metric tons)	Nonproducing	Producing	(Metric tons)	Nonproducing	Producing	(Metric tons)
None	●	$>10^9$	None	None	$>10^9$	None	None	$>10^9$
○	●	10^6-10^9	□	■	10^6-10^9	△	None	10^6-10^9
None	None	$<10^6$	□	■	$<10^6$	△	▲	$<10^6$

Figure 2. Geographical distribution of chromium resources. Modified after Papp & Lipin (2011).

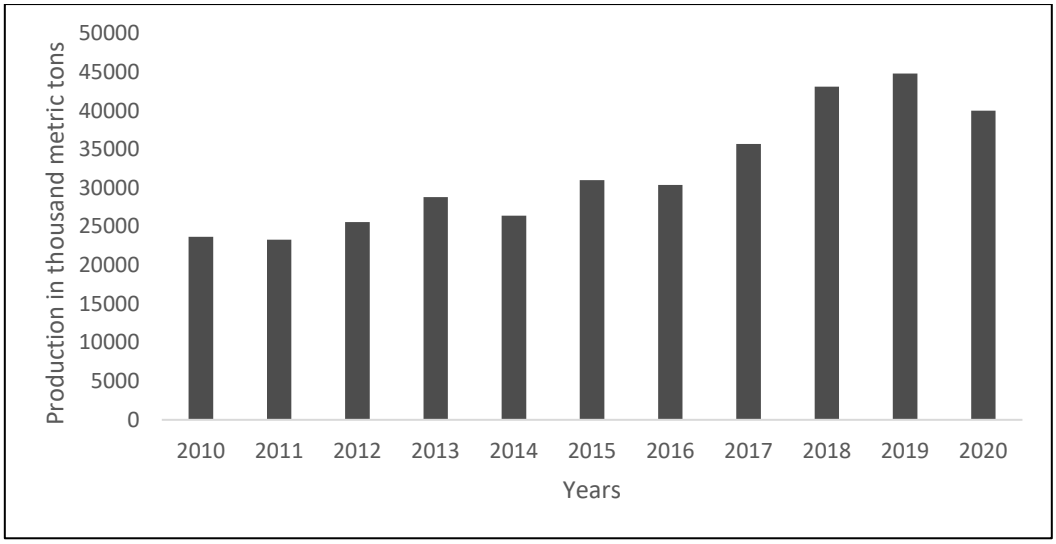

Figure 3. Chromium worldwide production from 2010-2020. The plot was modified after Statista (2021).

The benefits of chromitite contribute to not only the form of extraction but also beneficiation, as shown in Table 2, which demonstrates the processes involved in the beneficiation of the ore from either mafic or ultramafic sources. Table 3 shows the world resource estimate and mine production for the past two years for shipping grade (45 % Cr_2O_3) chromite. According to studies conducted by Papp (2017), the demand for chromite will be sufficiently met in the coming decades.

Table 2. Factors used to characterise chromite deposits and mining, beneficiation and processing methods applied to chromite deposits. Table modified after Papp (2017).

Mineral	**Appearance in ore**	**Deposit type**	**Host rock**	**Mining method**	**Beneficiation methods**	**Processing method**
Chromitite	Massive Disseminated	Stratiform Podiform	Mafic Ultramafic	Surface Sub-surface	Hand Sorting Screening	Sizing Roasting and Dissolution
					Gravity concentrator. Electromagnetic separation Heavy media separation	

Table 3. World production and reserves for chromium. Table modified after Papp (2017).

	Mine production ('000 t)		Reserves ('000 t)
	2015	**2016**	**2017**
South Africa	14 000	14 000	200 000
Kazakhstan	5490	5500	230 000
Other	4220	4200	N/A
Turkey	3500	3500	12 000
India	5490	3200	54 000
USA	-	-	620

1.2 Study location

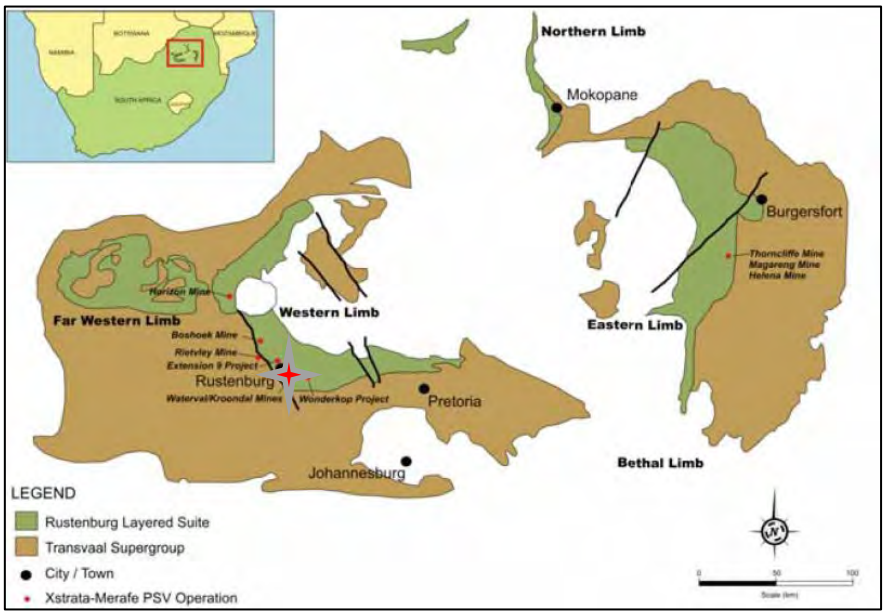

Figure 11. Location map showing Waterval Mine (indicated by the red star), modified after Gräbe (2015).

The typical vertical scale of the Critical Zone is 1500 m in thickness (Kinnaird *et al.*,2002) and divided into limbs in a typical mine such as the Waterval Mine, shown in Figure 12. The majority of the chromitite is hosted within the LG, MG and UG (Figure 13). The chromitite within the lower portion of the CZ is hosted amongst pyroxenites and dunites (Eales *et al.*,

1993). The MG layers are identified by plagioclase appearing as a phase; the lower MG chromitites are hosted in pyroxenites and harzburgites, with the upper MG layers being hosted in norites and anorthosites with cumulus plagioclase (Teigler *et al.*, 1992). The western limb of the complex towards the upper portion has two primary chromitite layers, the UG1 and UG 2; along the eastern lobe, there is often a UG 3 above the UG 2 (Teigler *et al.*, 1992). There is also "the pseudoreef" somewhere up there, too, in the western lobe. The Bastard 'Cyclic Unit' overlies the MR and contains measurable PGE associated with thin chromitites (Eales *et al.*, 1993).

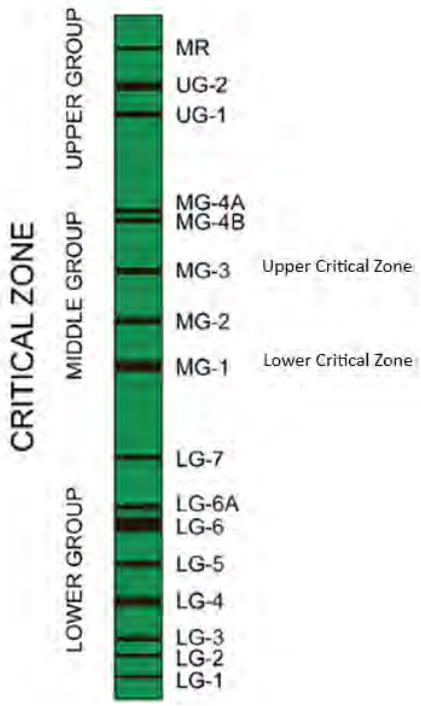

Figure 12. Simplified stratigraphy of the Critical Zone showing the positions and names of the significant chromitite layers. Modified after Oberthür et al. (2015).

1.3 Aim and objectives of the study

This current study focuses on the emplacement mechanism of the MG group chromitites by scrutinising the MG 1 and MG 3 layers. In core KD 151, the focus was placed on the MG 3 and MG 1 chromitite layers and their associated silicate rocks; these regions of the core time were spent for detailed observations. The differences and similarities of these layers will be explored as the study advances. The objectives of the study, as well as the primary aims, were to:

- First, determine the mineralogical, textural, and compositional characteristics of the HW and FW to the MG 1 and MG 3 layers.

- Secondly, to examine the PGE profiles of the hangingwall and footwall in contrasting lithological settings of the MG 1 and MG 3 layers.
- Finally, by evaluating mineral textures and compositions, evaluate the mechanism of formation or emplacement of the chromitites and their relationships with their host rocks.

The objectives listed above will feed into the primary aim of determining the emplacement model of these chromitite layers and their association with the PGE enrichments. The reason for choosing MG 1 and MG 3 specifically as targets for comparison is that MG 2 represents the typical first appearance of cumulus plagioclase in the stratigraphy. Hence, the MG 1 is the uppermost chromitite layer hosted in a pyroxenite hangingwall and footwall. In contrast, the MG 3 chromitite, only a few metres above it, displays the anorthositic footwall and pyroxenitic hangingwall, characterising the lithological style of all the overlying chromitites through the MG and UG sequence up to the top of the Critical Zone. It, therefore, represents a critical horizon petrographically but with a few other variables as different as possible. The MG 2 was not used for comparison because it was not well preserved in this part of the western Bushveld sequence.

Chapter 2

Review of magmatic chromitite petrogenetic concepts

2.1 Formation of the chromitite layers

Various origin models are contributed to the realities of the formation of the chromitite layers. These include fractional crystallisation, density sorting and settling, immiscibility of Cr-rich liquid, increased oxygen fugacity, contamination by siliceous materials, mixing of magmas and pressure changes. Each of these theories has been challenged, discounted, or complicated due to lack or the emergence of specific evidence; however, all contribute to a better understanding of the critical formation of the chromitite layers.

2.1.1 Fractional crystallisation, density sorting and settling

The solidification of magma results in mineral grains of different densities settling out and forming layers (Wager *et al.*, 1960). Some of the inconsistencies noted by Campbell (1978) are the mafic-felsic rhythmic layering, potential mineral density inversions, evidence for chemical sorting of minerals rather than mechanical when it comes to some textures, the assumption that nucleation is homogenous in magma and the buoyancy characteristics of felsic minerals in Fe-rich magmas.

2.1.2 Increase in oxygen fugacity

The model is based on Ulmer (1969), whereby a proposed increase in the fO_2 would have resulted in the prolonged formation of spinel. Ephemeral changes to a basic magma system were investigated by Murck & Campbell (1986). The results revealed that with an increase in the temperature and decrease in fO_2, the Cr contents of the melts at chromite saturation increase. This change in fO_2 was proposed to be brought upon by mixing different magma pulses accompanied by a temperature decrease or fluctuations in the fO_2 itself (Murck & Campbell, 1986).

2.1.3 Mixing of magmas and crustal contamination

Magma mixing can involve the mixing of felsic and mafic magmas. The addition of granitoid crust can facilitate chromite-only crystallisation but needs less than 50 % crust. Adding Fe stabilises olivine relative to chromite and reduces the curvature of the olivine-chromite cotectic. Irvine (1977) involves mixing primitive and evolved and Sharpe and Irvine (1983) of U and A

type magmas. Evidence of crustal contamination such as alkali inclusions in chromites and isotopic evidence for radiogenic enrichment and xenoliths of roof rocks in chromitites.

2.1.4 Pressure changes

The changes in the pressure of the magma system were considered by Lipin (1992) when working on the Stillwater Complex. Mafic magma in a shallow chamber is thought to be saturated with CO_2 due to its low solubility (Lowenstern, 2001). In Figure 4, it was observed that with an increase in pressure, the crystallisation field of spinel shifts to become more prominent (Hatton & von Gruenewaldt, 1989). The temporal increase in the pressure was due to the release of CO_2 in the magma from new pulses by magma depressurisation during emplacement into the magma chamber.

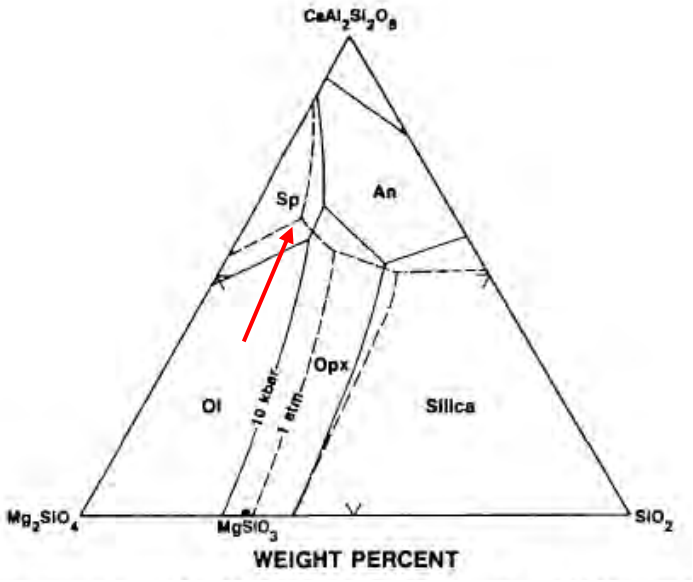

Figure 4. A pressure-induced shift in the stability field influences the compositional field of spinel stability as indicated by the red line. Plot modified after Lipin (1992).

2.2 Association of platinum group elements and chromitites

Chromitites occur as stratiform layers within the Critical Zone of the Bushveld Complex. The Lower Critical Zone features thick (decimetre to metre scale) chromitites hosted within orthpyroxenites. In contrast, the Upper Critical Zone hosts thinner (decimetre to centimetre scale) chromitites typically characteristically associated with a leucocratic to anorthositic footwall and a variably pegmatoidal feldspathic orthopyroxenitic hangingwall (Kruger, 2005).

The top, or end of the Lower Critical Zone, or more appropriately the base of the Upper Critical Zone, is taken as the first cumulus plagioclase within orthopyroxenite. The Lower Critical Zone

are IPGE (Ir, Os, Ru)/PPGE (Pd, Pt, Rh) (Mondal, 2011) enriched in comparison to the Upper Critical Zone, and the chromitite layers tend to be PPGE poor and dominated by IPGE (von Gruenewaldt & Merkle, 1995). The Upper Critical Zone magmas next emplacement, dominantly norite with orthopyroxenite and anorthosite layers. The Cr layers are richer in platinum group minerals and higher Pt + Pd + Rh / Ru + Ir + Os than the LCZ (Kruger, 2005). Reef-type PGE deposits primarily consist of Pt, Pd, Rh and other less abundant PGE. Associated deposit types can include stratiform chromitite (as seen in the Critical Zone), stratiform titanium vanadium oxides (as seen in the Upper Zone) and magmatic sulphide-rich nickel and copper deposits.

2.2.1 Magmatic fractionation and settling:

Several models for associated chromite and sulphides involve the saturation of these phases in magmatic liquids and their subsequent settling to the top of the cumulated pile underlying them; In these models, the exsolution of immiscible sulphide liquid from the mafic silicate melt collects the PGE, Cu and Ni, which prefer the sulphide liquid to the silicate melt (Haldar, 2018). The solubility of the sulphide in the magma is affected by the bulk magma composition, the temperature, pressure and fugacity of both oxygen and sulphur (Zientek, 2012). The fractionation of sulphide melts occurs during the crystallisation phase of Cu-Ni sulphides, common to mafic to ultramafic magmas. Therefore, the resultant evolved sulphide ores are more Cu and Ni-rich (Graham *et al.*, 2017). The mechanisms of fractionation and migration result in the concentration of these sulphides away from their residual components (Mungall and Brenan, 2014). During the crystallisation phase of the magma-sulphide system, the formation of highly PGE-rich sulphide-bearing layers results in stratiform deposits associated with modal layering in the silicates. Separation of the sulphides may occur during the crystallisation and settling phase. Note that typically sulphide-controlled PGE scavenging produces higher PPGE/IPGE, as seen in the Merensky, UG-2, and Stillwater reefs, while chromite-controlled scavenging (as in ophiolites) shows more IPGE/PPGE.

2.2.2 PGE solubility in magmatic fluids

An alternative model for PGE enrichment ties in with the crystallisation of chromitite without simultaneous magmatic sulphide immiscibility, resulting in the enrichment of Ru, Ir and Os at the expense of Ni, Cu, Pt, Pd and Au. Hydrothermal re-distribution of the PGE is less well understood because of the uncertainty about the compositions of the hydrothermal fluids at magmatic or near-magmatic temperatures and the PGE solubilities in those conditions. Potentially, this could involve a saline brine at ~600-800°C and ~1.5 kb pressure (Manning and

Aranovich, 2014). This type of fluid could dissolve Pt with a direct relationship of PGE solubility with temperature.

2.2.3 Petrological control of PGE minerals in chromitites

The normalised patterns of the Middle Group and Upper Lower Group chromitite show a slight positive-sloping pattern which suggests that they are BMS controlled. A Pt/ (Pt + Pd) plot shows a correlation between the thickness of the layer and the total PGE. Strong positive correlations observed in UG and MR indicate sulphide-controlled PGE accumulation. The upward increasing PGE content and ratios can indicate post-magmatic effects with sulphides. In Figure 5, it is seen that the MG 1 and 2 layers have a higher (Pt + Pd)/ (Os + Ir + Ru) than the Lower Group layers, but this ratio gets lower in MG 3 and 4 and then increases again in UG 2 and MR. the Pt/ (Pt + Pd) ratio is high (> 0,6) in LG and MG. A strongly positive-sloping pattern as the chromitite layers increase indicates that the Upper Critical Zone chromitite layers are more evolved, and flat patterns are from rocks that are more primitive (von Gruenewaldt and Merkle, 1995).

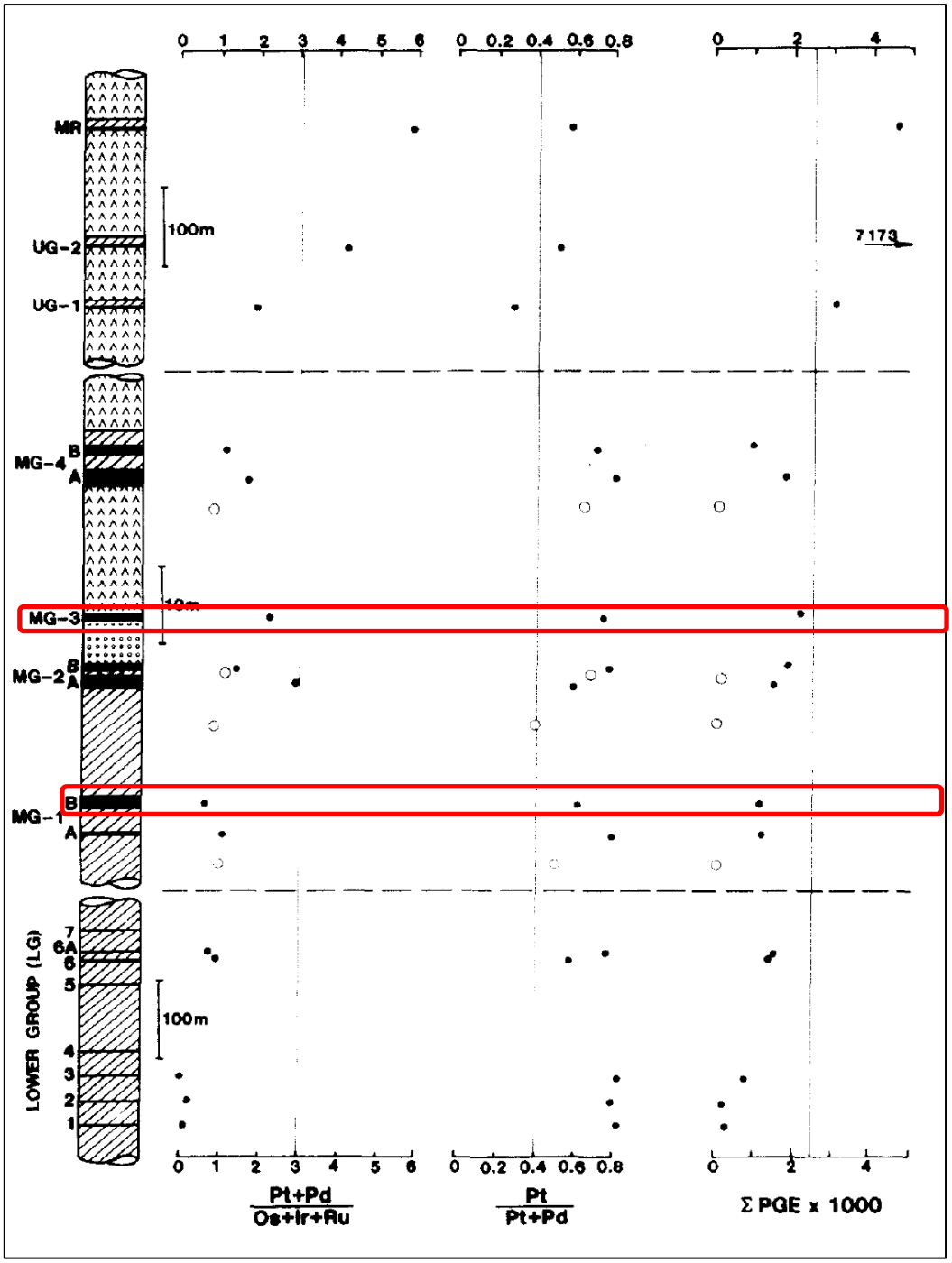

Figure 5. Variation of PGE ratios in the chromitite layers and the Critical Zone host rocks, red boxes indicate the MG 1 and MG 3 chromitites. Plot modified after von Gruenewaldt and Merkle (1995).

Von Gruenewaldt and Merkle (1995) argued that the significant factor in the accumulation of Pt and Pd was the initial presence of base metal-bearing sulphide within the chromitite. At the point of the Middle Group layers', cumulus plagioclase starts to appear, representing fountaining of a new magma input (Latypov *et al.*, 2020). Irvine (1977) suggested that the

mixing of primitive and evolved magmas could induce chromite precipitation. This process impedes the formation of olivine and orthopyroxene and promotes chromite formation. Many chromitites from layered complexes contain much higher proportions of Pt and Pd relative to Ru, Ir and Os than those from the ophiolite complexes. Within layered intrusions, the richest chromitites in PGE appear with the appearance of cumulus plagioclase. As chromitites cool, vacancies within the structure take up Fe from any associated BMS, causing a loss of sulphur to surrounding rocks; therefore, Cu, Ni and PGE increase in the remaining BMS (Naldrett and von Gruenewaldt, 1989).

2.2.4 Redox gradients along the melt-chromite interface for the formation of PGE

Chromite has been observed to be a concentrator of PGE, which is mainly observed as platinum group minerals encircled by chromitite grains. The model proposed for the formation of these minerals (Pt-Fe alloys & laurite, amongst others) can occur along the interface of the melt-chromite whereby a change in conditions such as the onset of recrystallisation or equilibrium is reached (Finnigan *et al.*, 2008).

As a result of the siderophile nature of PGE, the PGE has the potential to occur in magmas as metallic clusters of 50-100 atoms rather than cations or any molecular species (Tredoux *et al.*, 1995). Stabilisation of these clusters occurs by ligands (S, As and Te) through adsorption and are not bonded, as illustrated in Figure 6. In sulphide-rich environments, the PGE-ligand structures are included in the sulphide melt. The proportion of PGE-clusters that have not separated become inclusions in BMS. At lower temperatures, the structure of the BMS reorganises, resulting in the expulsion of the PGE as PGM. Sulphide-poor environments allow the clusters to remain suspended until their form alloys, Ir and Os should remain abundant due to higher stability temperature.

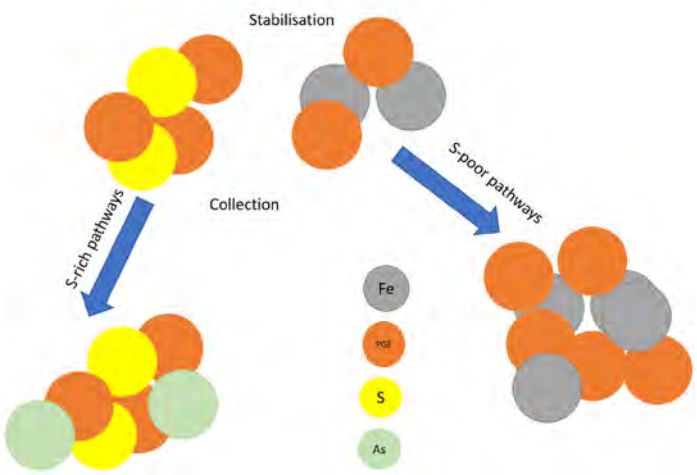

Figure 6. The mechanisms for sulphur collection of PGE. Modified after Tredoux et al. (1995).

Platinum group elements fractionate in order of descending melting points (in the order Os, Ir, Ru, Rh, Pt, Pd and Au) according to Barnes & Naldrett (1985). They suggest that possible mechanisms for the origin of this fractionation include alteration, partial melting, and crystal fractionation. The carbonate alteration affects Au and Pt, while hydrothermal alteration mobilises Pd (Tredoux et al., 1995); this suggests that PGE fractionation in silicate magmas is due to the solubility of the PGE. Pd, Pt and Rh are more soluble than Os and Ir, which form an alloy and Ru forms laurite. The fractionation phase is before Fe-Ni-Cu sulphide saturation. Alteration affects PGE mobility according to Ir<Os<Ru<Rh<Pt<Pd in terms of solubility in aqua regia. An unaltered rock would likely have a positively sloping normalised PGE profile pattern, whilst an altered rock should have a flatter pattern; altered rocks are not perceived to be a dominant process for PGE fractionation in these rocks.

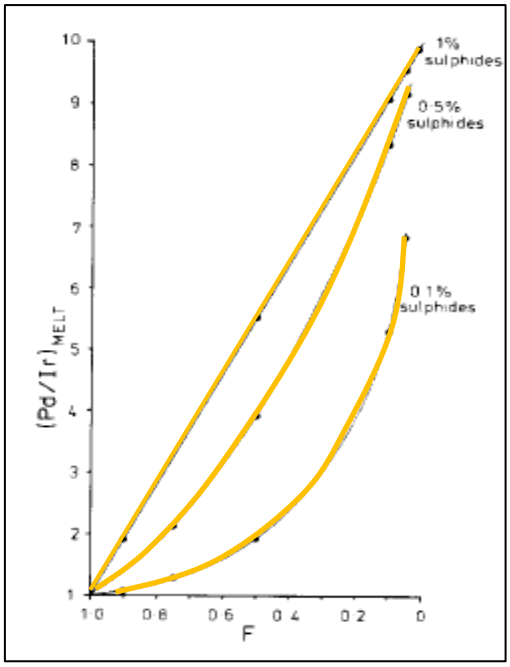

Figure 7. An increase in the Pd/Ir ratios with an increase in the sulphide content of the magma. Modified after Tredoux et al. (1995).

The crystal fractionation model suggests that PGE fractionation is brought about by removing IPGE from the magma in olivine, chromite, sulphides or PGMs. IPGE minerals are observed as inclusions in olivine. They also occur as either inclusions or solid solution substitutions in chromite (Barnes *et al.*, 1985).

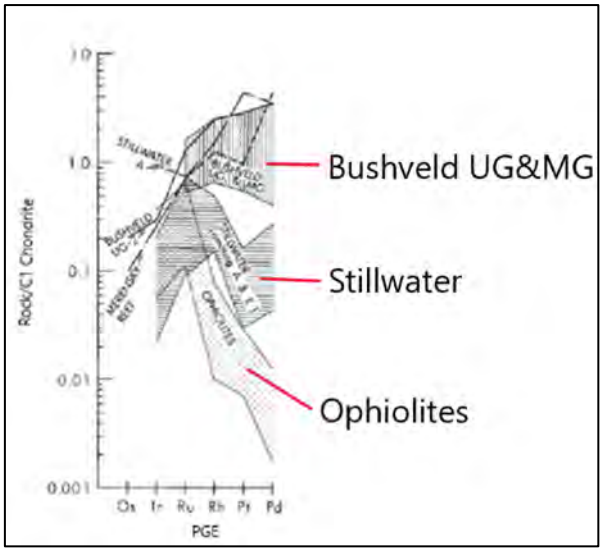

Figure 8. Typical Rock/Chondrite concentrations of PGE in typical layered intrusions. Modified from Barnes et al. (1985).

The importance of the R-factor (magma/sulphide) in the formation of PGE-enriched sulphides is shown in Figure 7. The R-factor is low if there is a small amount of magma and high sulphides so that the magma will be depleted in PGE, and the sulphides will have a low amount of PGE. If the R-factor is high, the magma will be less depleted, and the sulphides will be more highly concentrated in PGE. There are two reasons why the MG chromitites are relatively depleted in PGE: they may have a lower overall original sulphide content, and the sulphides themselves have been less enriched in PGE, possibly because of a lower R-factor process. Higher proportions of Pt and Pd in chromitites from layered intrusions are possibly due to higher sulphide content (Naldrett and Von Gruenewaldt, 1989). In Figure 8, a typical mix of rock and chondrite concentration is shown in commonly found layered intrusions.

Primary PGM occurs as euhedral crystals enclosed within chromite grains and are believed to have formed high-temperature magmatic systems. Secondary PGM occurs closely with serpentine, chlorite, and similar secondary phyllosilicates, formed at lower (sub-magmatic) temperatures, possibly due to hydrothermal activity (Zaccarini *et al.,* 2002). The collection of the PGE in chromitite layers of the Merensky Reef at the Rustenburg platinum mines occurred in two steps; some PGM crystallised from the magma during the formation of chromite and before sulphide saturation (Godel *et al.,* 2007). The second step involves forming an immiscible sulphide and the PGE collected by this liquid, which then descended into the existing chromitite crystal pile. In the silicate rocks at the cooling phase, the PGMs have been extracted from the MSS and ISS into chromitites and silicates (Godel *et al.,* 2007). Some magmatic sulphide deposits are zoned, locally enriched in Ir, Os, Ru and Rh, and Fe (concentrated in MSS), whilst the complementary regions are enriched in Pd, Pt, Cu and Au (concentrated in sulphide liquid); this is the Intermediate solid solution (Cu, Fe) S_{1-x} and Monosulphide solid solution (Fe, Ni) S_{1-x}. (Fleet *et al.*, 1994). The monosulphide solid solution ($Fe_{1-x}S$) has a structure informed by ordering vacancies on the Fe position. Ir^{3+} and Rh^{3+} could take up the sites for Fe^{3+} in MSS if the sulphur content increased. During MSS crystallisation under S-saturated conditions, Ir and Rh behave compatibly, contrasting with Cu, Pt, and Pd (Li *et al.*, 1995). The IPGE, Rh and Re are compatible in MSS relative to sulphide melt shown in Figure 10.

Conversely, Pd, Pt, Au, Ag, Pb and the chalcogens are incompatible with MSS. The collection of PGE was further investigated by Barnes and Maier (2002), and this process subsequently follows magma mixing within the chamber; the chromite and PGE enriched sulphides layers are then formed. The PGE enriched sulphide then interacts with the chromitites, thus inducing

a decrease in fugacity. This allows for the trapping of the platinum group minerals within the sulphide.

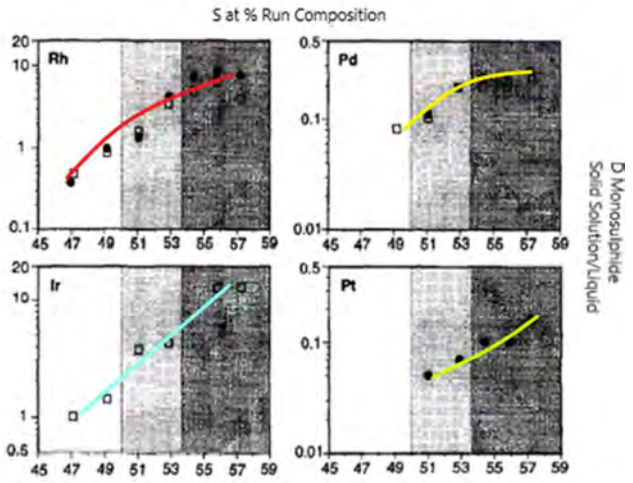

Figure 9. Plots show the effect of temperature and percentage sulphur in the melt and its effect on partitioning. Modified from Liu et al. (2015).

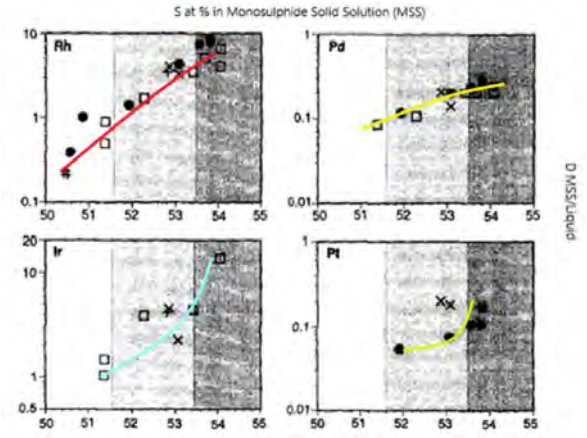

Figure 10. Plots show the effect of temperature and percentage sulphur in the melt and its effect on partitioning. Modified from Liu et al. (2015).

2.3 Emplacement of the chromitite layers

The emplacement of the chromitite layers has three potential models, namely, 1) the PGE-sulphide bearing (± chromite) reef emplaced into existing leucogabbronorite to norite sequence, 2) the separation of MSS from sulphide liquid to explain IPGE and PPGE separate and 3) upgrading/diffusion-driven concentration of PGE sulphides ± chromitite at reef margins, driven by thermal & chemical gradients facilitated by water. In this model, pegmatoid development was linked to PGE-sulphide enrichment.

2.3.1 Lateral growth within a magma chamber

The more mechanical chromitite formation models can first involve the magma movement down the chamber wall resulting in different fractionations due to the density and velocity proposed by Wager and Brown (1967). The second popular model involves a magma plume into a pre-existing chamber, settling out of crystals by density, potentially forming different layers and thicknesses (Kinnaird, 2002).

2.3.2 Injection of a chromitite slurry

Eales (2000) stated that the amount of chromium in chromitite layers, disseminated layers and the silicate in the Bushveld exceeds the experimentally determined solubility. He concluded that 3 wt.% chromite microphenocrysts had already enriched the chamber's magma from a deeper-seated magma chamber. The phenocrysts are either carried along by dissolving them in a more ultramafic magma (Eales & Costin, 2012) or being carried. It may have formed because of within-chamber contamination (plume-roof), syn-ascent contamination, or from the deeper (pre-emplacement). Alternatively, magma contamination consumes energy and stimulates crystallisation and enhances the dissolved water content (Prevec *et al.*, 2016). The addition of water stabilises oxides, resulting in the then possible curbing of the crystallisation path (Howarth & Prevec, 2013).

Chapter 3

Methodology

3.1 Sample material

The MG 3 chromitite layer is 101 cm thick with an immediate HW of 149 cm thickness and a 150 cm FW. The FW comprises of an anorthosite (110 cm) at the base, followed by a leuconorite (10 cm) layer, a chromitite stringer with undulating contacts (3 cm), and anorthosite (20 cm), then lastly, a 10 cm norite which forms a gradational and straight contact to the MG 3 chromitite. The HW to the chromitite is a norite (149 cm). The MG 1 chromitite is 61 cm thick with a 52 cm thick HW and FW. The FW has a melanoritic (45 cm) layer followed by a 5 cm thick pyroxenite, which becomes a 3 cm leuconorite that forms a gradational contact with the base of the MG 1 chromitite. The HW to the MG 1 chromitite is a 5 cm thick melanoritic layer with a gradational contact followed by a 3 cm thick pyroxenite, a 15 cm thick melanonorite, a 20 cm gabbronorite and a melanorite of 10 cm, forming the top of the sample range in the HW.

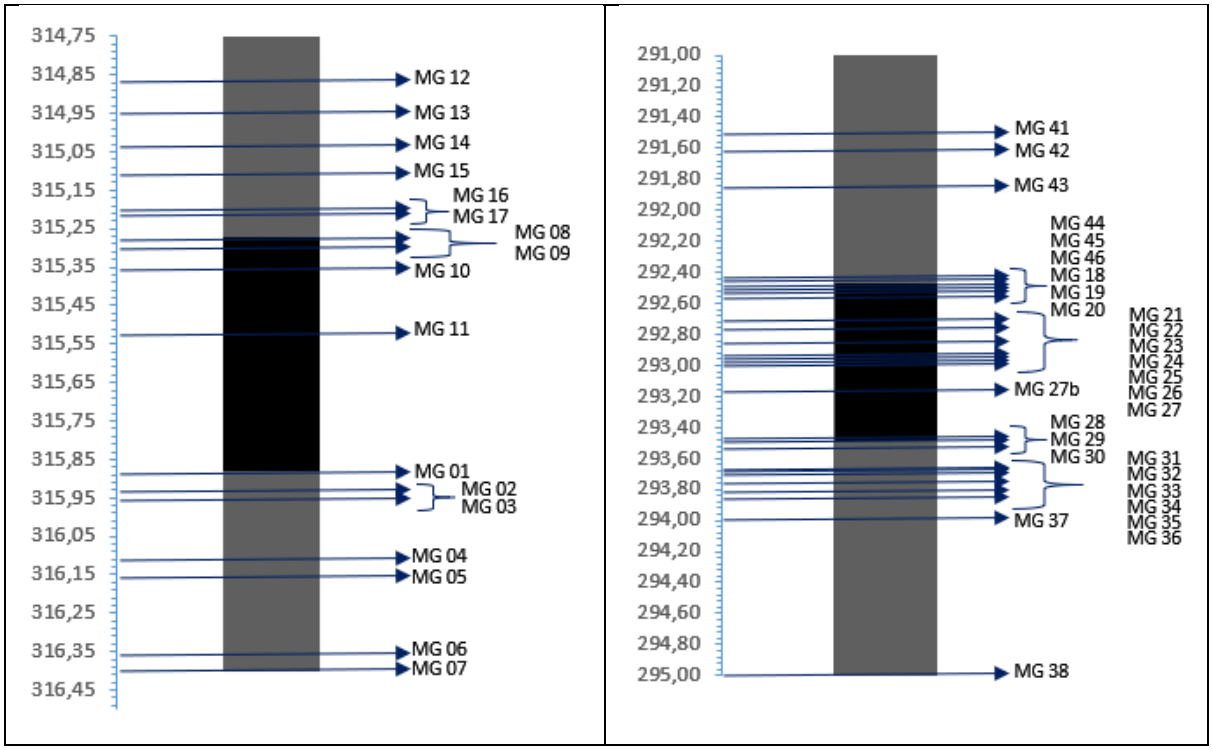

Figure 13. Sampling horizons from the chromitite-hosting sequence. MG 1 is shown on the left, with the MG 3 sequence on the right. The y-axis indicates stratigraphic depth in metres.

3.2 Sample collection and preparation

Glencore Xstrata Alloys kindly provided access to the drill core. After inspecting multiple core samples, Borehole KD151 was chosen due to its well-researched and documented sequence of MG chromitites that are well preserved and offer distinct footwall and hanging wall lithologies. The advantage of a single stratigraphic section is to prevent unnecessary complications to comparisons introduced by lateral variation effects in the layering (Maier and Barnes, 1998). The cores diameter was 38 mm with a total length of 26 m which was provided for sub-sampling. The core contained three chromitite sequences, MG 4 (259-269 m depth), MG 3 (291-303 m depth) and MG 1 (314.5-316.5 m depth) with an anorthositic layer (327-329 m depth). Core sequences for the MG 3 and MG 1 were logged on-site and then removed and studied in further detail at the Department of Geology at Rhodes University, where they were logged in detail and sampled for analysis (Sampling points along the core are shown in Figure 15). Subsamples of 5 cm length were cut from the core, where the sample depth corresponds to the top/bottom of the sampled length. The sample length was chosen to optimise the spatial resolution of the study whilst still providing sufficient representative material for analysis. A subsample of this core was cut for a thin section briquette, and the remainder was crushed for geochemical analysis.

Selected portions of the core were cut for thin and polished thin sections at the Rhodes University Geology Department. These sections were then used for petrographic microscopic evaluation. For geochemical characterisation, and the samples had to be powdered, the core was crushed utilising an Osborn-Massco jaw crusher. The crushed pieces were then milled to an average grain size of less than 400 mesh (estimated) using a Herzog swing mill. The prevention of cross-contamination during crushing was done with the thorough cleaning of all crushing surfaces with distilled water and acetone between samples. Pre-contamination of samples was not practical due to the small sizes of the samples collected, and quartz crushing between samples was avoided in this case to minimise the possibility of silica contamination in relatively ultramafic rocks, despite the slightly higher risk of between-sample contamination. Samples were crushed in order of sample number so that any effects of cross-contamination would effectively be minimised geologically by restricting it to neighbouring samples.

3.3 Analytical methods

3.3.1 Petrography

Leica binocular petrographic microscopes with both transmitted and reflected light capability were used for the petrographic characterisation, and point counting was conducted to estimate modal abundances of specific mineral phases by doing a count of 250 points per section (per sample) on a James Swift point counter., These modal abundances were then used to classify the rocks (Le Maitre *et al.*, 2002). Photomicrographs of the samples were taken with an EC high-resolution camera with post-processing completed on the Leica application suite.

3.3.2 XRF analyses

Major oxide analysis was conducted at the Ministry of Northern Development and Mines GeoLabs in Sudbury, Ontario (Canada) by XRF, according to the methods described by Keating and Burnham (2013): The method XRF-T02 was utilised for the analysis of trace elements with XRF-M01 being used for the major oxides and XRF-MOX being used for the custom elements analysis which included the chromitites. The detection limits for the analysis are listed in Appendix 8.1.

3.3.3 Electron Probe Microanalysis

EPMA data acquisition was performed at Rhodes University, Department of Geology, on a Jeol JXA 8230 Superprobe, using 4 WD spectrometers. Analytical conditions employed were acceleration voltage 15 kV, probe current 20 nA, beam size 1 micron, counting time 10 sec on peak and 5 secs on background (except Ni, where the counting time was 20 s and 10 s,

respectively). The standards used for measuring the characteristic Kα radiations were natural minerals: forsteritic olivine for Si and Mg in olivine; fayalite for Fe in all silicates (except phlogopite); diopside for Si and Mg in all silicates except olivine; diopside for Ca in olivine; almandine for Al in all silicates and Fe in phlogopite. In all analysed minerals, the following standards were used: chromite for Cr, rutile for Ti, rhodonite for Mn, orthoclase for K, and albite for Na. In most cases where an element concentration is below 5%, a large diffracting crystal with high sensitivity was used: LIFL for Ni and Mn in olivine and pyroxene; PETL for Ca in olivine, Ti and Cr in most silicates, V in chromite; TAPL for Na in pyroxene, phlogopite and serpentine. The ZAF matrix correction method was used for quantification (Costin, 2012). The detection limits for the analysis are listed in Appendix 8.2.

3.3.4 ICP-MS analyses

Trace elements were measured using ICP-MS analyses on the samples conducted after a closed vessel multi-acid digestion (IMC-100) technique (Burnham *et al.*, 2002) at the Ministry of Northern Development and Mines GeoLabs in Sudbury, Ontario (Canada).

3.3.5 NiS Fire Assay

ICP-MS also analysed the PGE at the MNDM GeoLabs. The PGE was first pre-concentrated using a Ni-S fire-assay preparation (Jackson *et al.*, 1990). The in-house IMP 200 method based on 15 g sample sizes was used but could not be utilised effectively for all the samples due to the limited amount of material available. The low-level sample preparation method NFA-100 was followed (Burnham, 2008).

Chapter 4

Results

4.1 Petrography

4.2 Microscopic Textures

The below chapter describes the textures observed in both the silicate and chromitite rocks from both sequences.

4.2.1 Silicate Rock Textures (Figures 14 and 15)

The pyroxenes ranged from being anhedral rounded grains to lath-shaped grains; the diameter of the anhedral grains was ~1 mm, with the length of the laths being ~2 mm. There appeared to be discontinuous clinopyroxene rims on orthopyroxene; the textures did not appear fresh but showed alterations. Some of the pyroxene grains showed exsolution lamellae; these favoured a specific orientation within the hosted grain, while others tended to have a "blotchy" texture. The plagioclase grains are interstitial and have an irregular shape; a few grains were noticed to have bent twinning from the MG 1 group samples. The plagioclase grains in MG 3 (MG 45D) and MG 1 appear to be strained and deformed (MG 03B).

4.2.2 Chromitite Textures

The sizes of the chromitite grains ranged from 0.05 to 1.5 mm, some of the grains were anhedral, whilst others showed either a pentagonal or hexagonal grain shape. The chromites show a 120°contact with their neighbouring grains, as seen in Figures 16 A, B & C. In Figure 16 D-G, the chromitites are not in contact with each other and are therefore subhedral to

anhedral and hardly any straight lines are observed between the attached chromitites. The chromitite showed sulphides within the grains and the boundaries; these sulphides are not typical and measured ~0.02 mm in size.

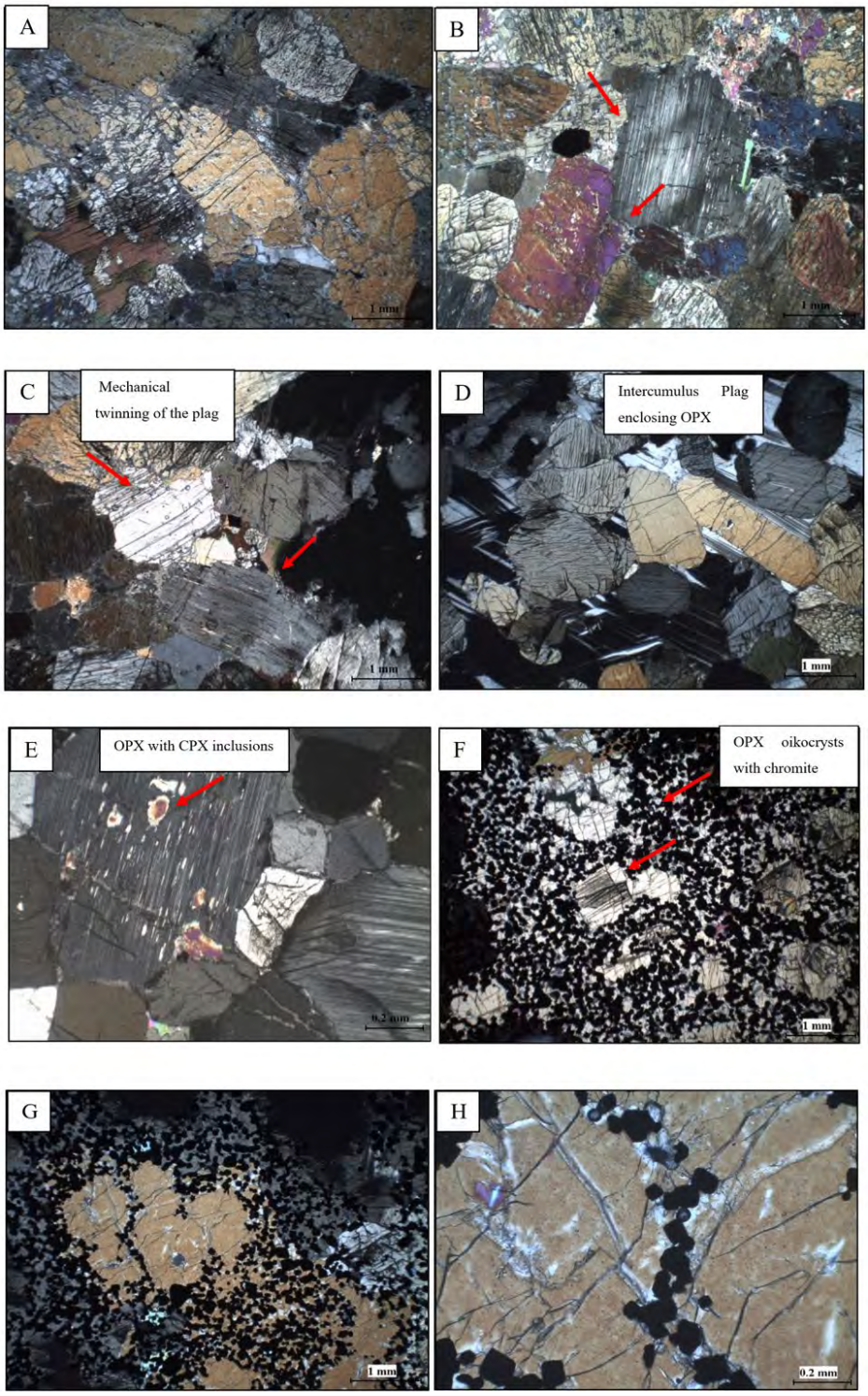

Figure 14. Images of borehole KD 151 showing microscopic textures associated with the MG 1 chromitite suite: A) OPX with some alteration, B) OPX and CPX both observed, C) Mechanical twinning/ deformational features associated with the plagioclase, D) Intercumulus plagioclase with OPX, E) OPX with CPX inclusions, F, G and H) OPX oikocrysts surrounded by chromite grains. All images except for F are taken in XPL. Red arrows indicate the position of the mentioned textures.

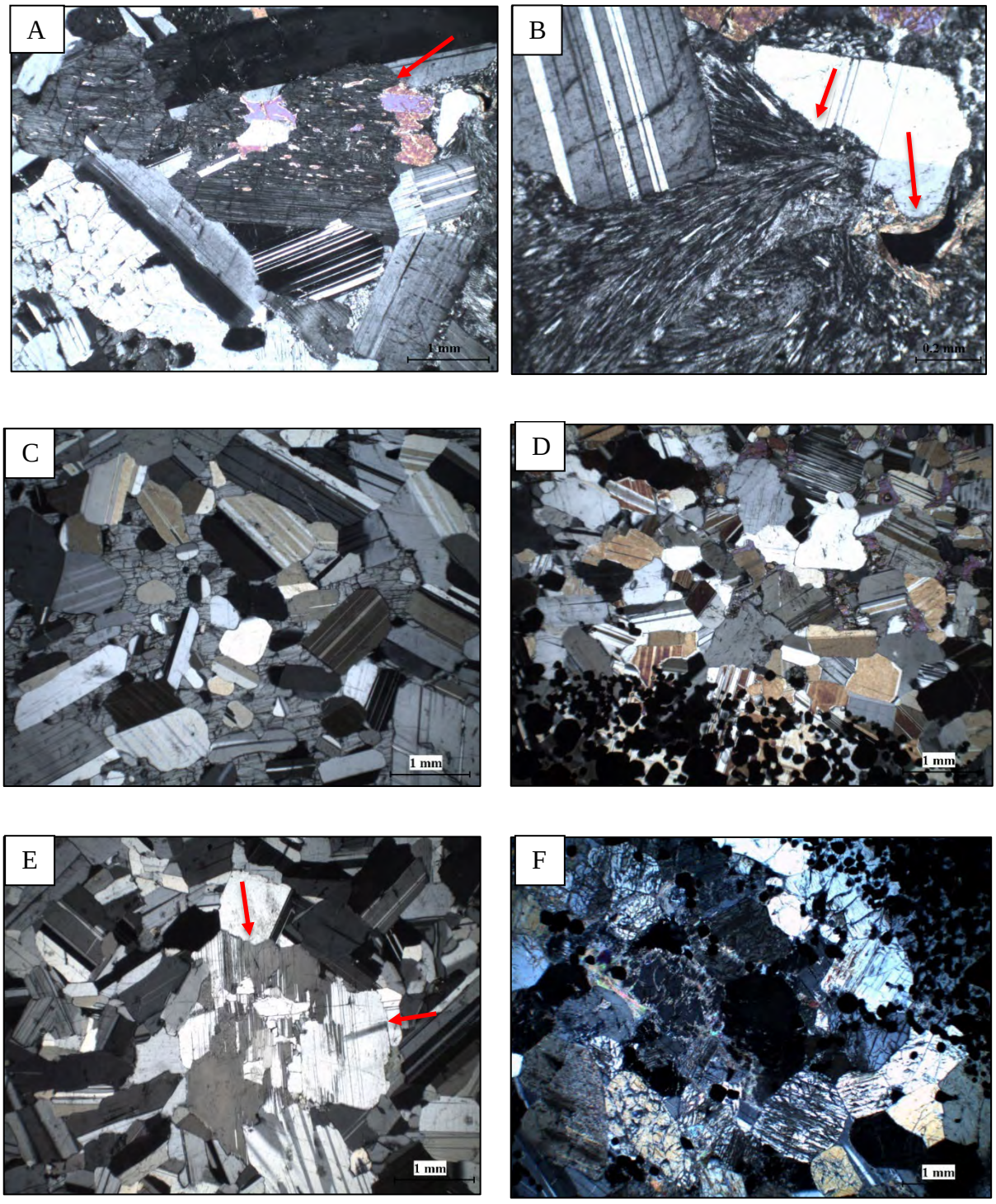

Figure 15. Images of borehole KD 151 showing microscopic textures associated with the MG 3 chromitite suite: A) CPX inclusions in an OPX, B) Alteration of the plagioclase resulting in horsehair textures, C) Intercumulus OPX with plagioclase, D) Typical cumulus texture with chromite present, E) Deformation of the plagioclase observed by differential twinning, F) Alteration textures of the OPX and plagioclase. All the images are taken in XPL. Red arrows indicate the position of the mentioned textures.

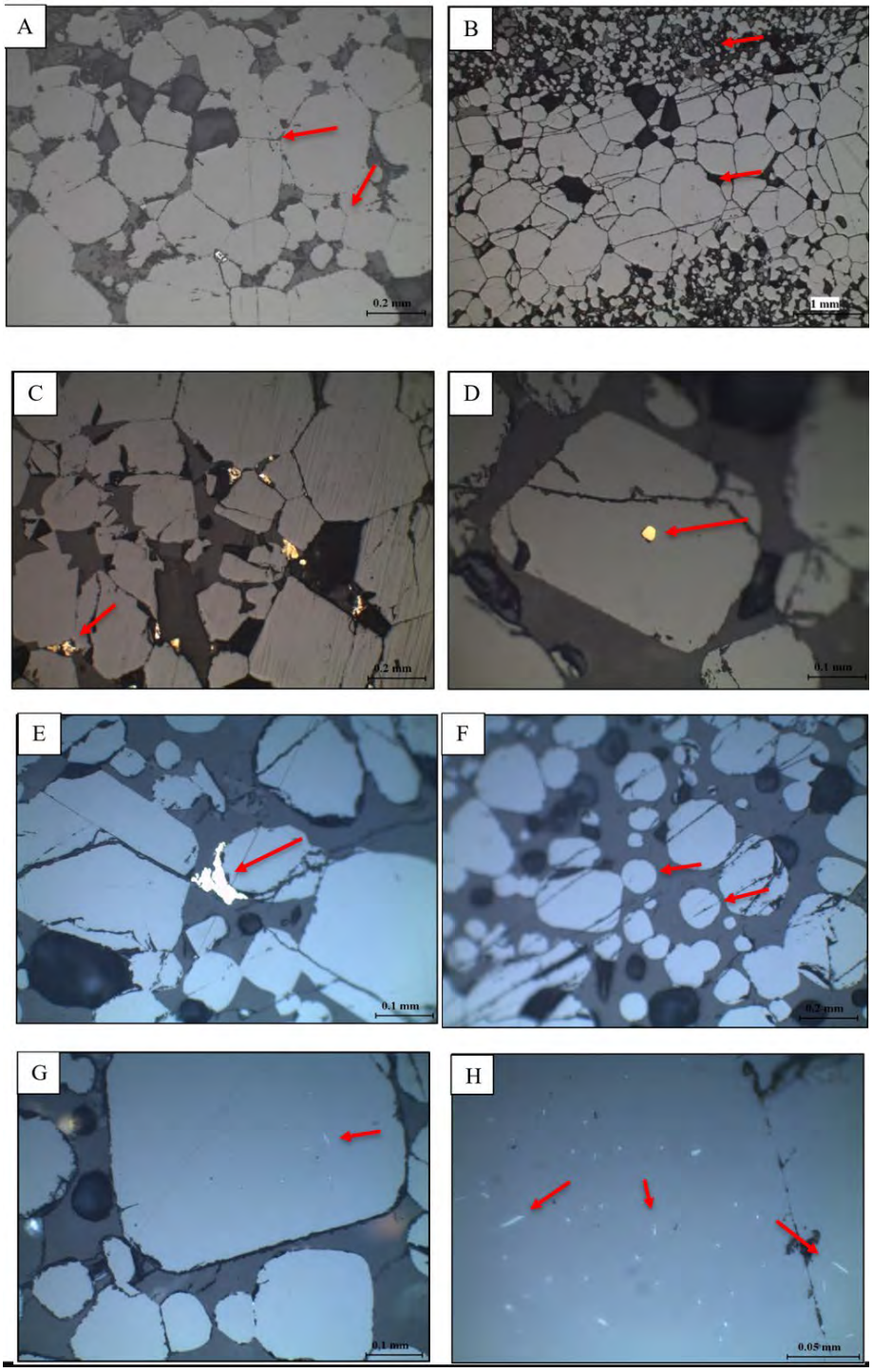

Figure 16. MG 1 and MG 3 chromite images: A) Triple junctions observed in the chromite grains with intercumulus silicates, B) Bi-modal grain size distribution of chromite grains, C) BMS at the boundaries of the chromite, D) BMS inclusion within chromite, E) BMS partially surrounding chromite, F) Rounded, globular chromite grains contrast with the angular straight-line grains, G) Chromite with ilmenite inclusions, H) The inclusions of ilmenite appear not to have a specific orientation. All images are taken in PPL. Red arrows indicate the position of the mentioned textures.

4.2.3 Disequilibrium Textures (Figure 17)

These textures were observed in both the MG 3 and MG 1 rocks, although MG 3 had the most noticeable embayed grains and rims. Disequilibrium during the progression of a magmatic system results in these textures; the intensity and affected areas are variable. The typical interpretations of these textures are thought to be variations in pressure, temperature or a compositional change that upset the balance of a magma body (Perugini *et al.*, 2003).

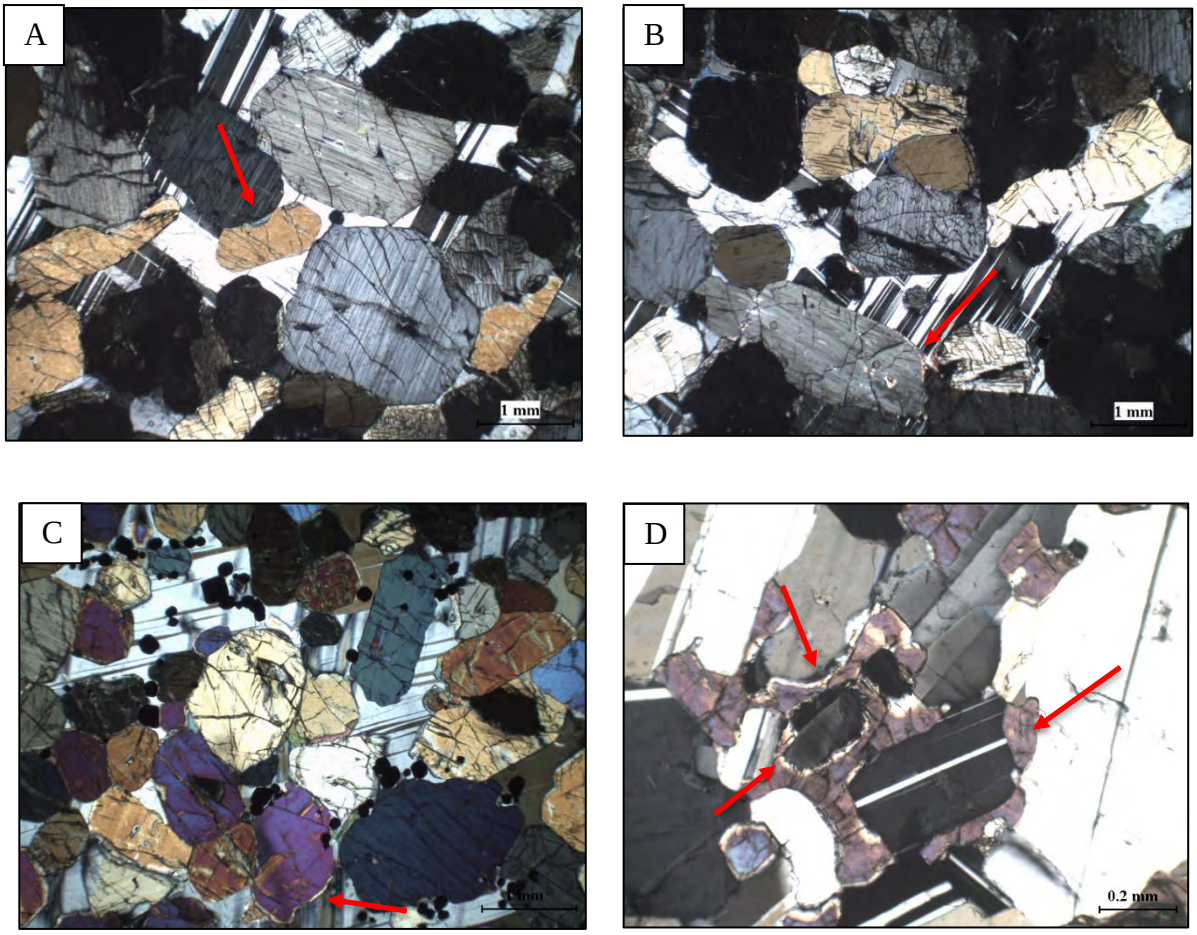

Figure 17. Images of MG 1 and MG 3 suite rocks showing disequilibrium textures: A, B, and C) OPX grains with rims of olivine D) A partially resorbed grain of plagioclase surrounded by olivine. All images are taken in XPL. Red arrows indicate the position of the mentioned textures.

4.3 Modal Classification

The classification of the rock types will be based on their mineral abundances determined during the point counting process. The method relies on determining the significant mineral phases present, and being significant means having a 5% and greater mode.

The MG 1 chromitite layer is situated in the LCZ and has a pyroxenite layer in the FW and HW in the eastern limb (Kottke-Levin, 2011). The MG 3 chromitite layer is in the UCZ, it has a HW of norite, whilst the FW is more leuconoritic due to the decrease in pyroxene.

Segments MG 41 to 46 represents the immediate HW to the MG 3 chromitite seam, with segments MG 30 to 38 representing the immediate FW. The MG 1 chromitite seam immediate HW and FW are represented by MG 01 to 07 and MG 12 to 17, respectively.

The immediate HW of the MG 3 suite shows approximately equal proportions of plagioclase and pyroxenes, and this is a similar trend seen in the immediate. The HW and FW's pyroxene content is significantly more than the plagioclase. There is more clinopyroxene in MG 1 suite than in the MG 3 suite, with the modal mineral proportions represented in Figures 18 and 19.

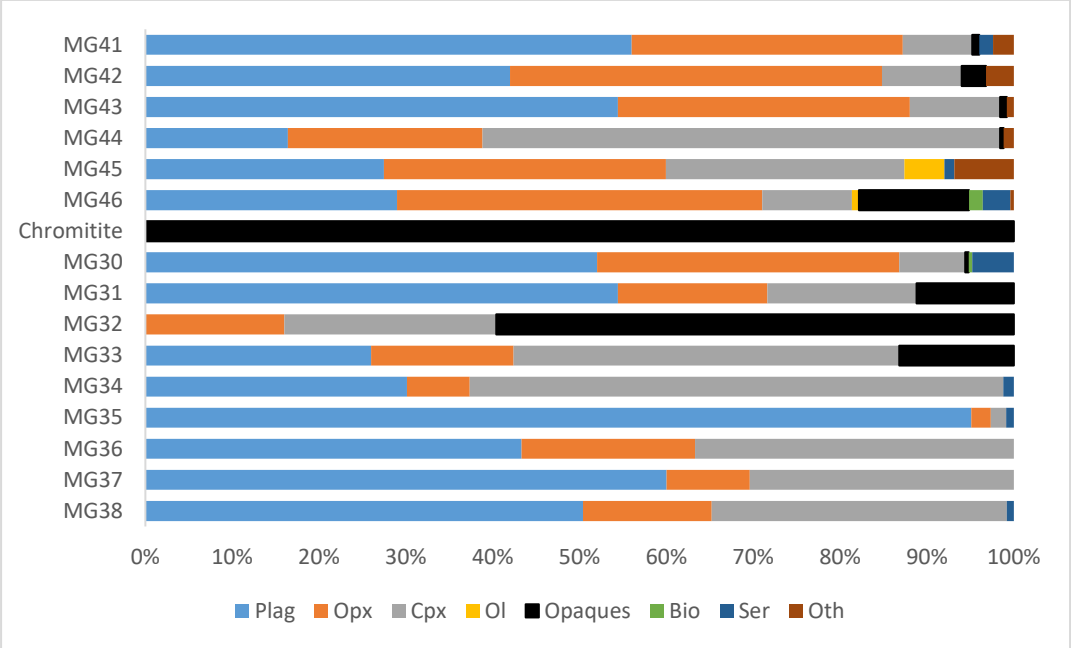

Figure 18. Modal proportions across the MG 3 chromitite suite.

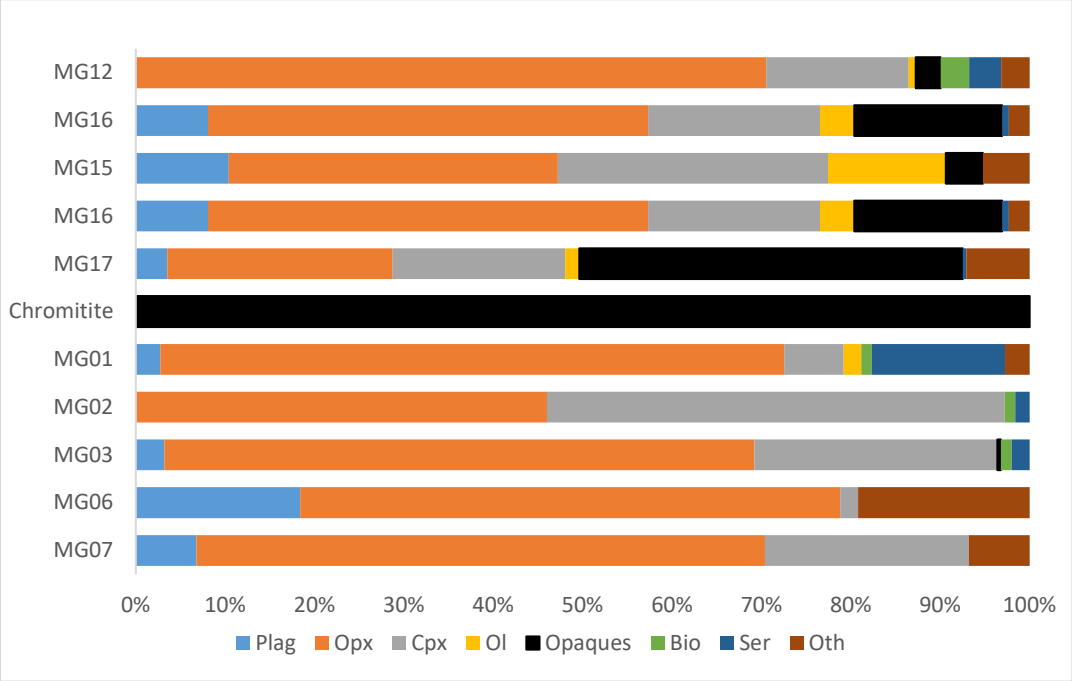

Figure 19. Modal proportions across the MG 1 chromitite suite.

The MG 3 chromitite has a noritic HW with the FW ranging from melanonorite sections to anorthosite to norite. The MG 1 HW is predominantly melanonorite with gabbronorite and norite sections present; the FW was determined to be melanonoritic with minor pyroxenite layers. Figure 20 shows how the rocks were classified on a smaller scale (5 cm widths) using thin sections compared to the core, which was field logged as a norite FW and HW for the MG 3 chromitite and a pyroxenite FW and HW for the MG 1 chromitite.

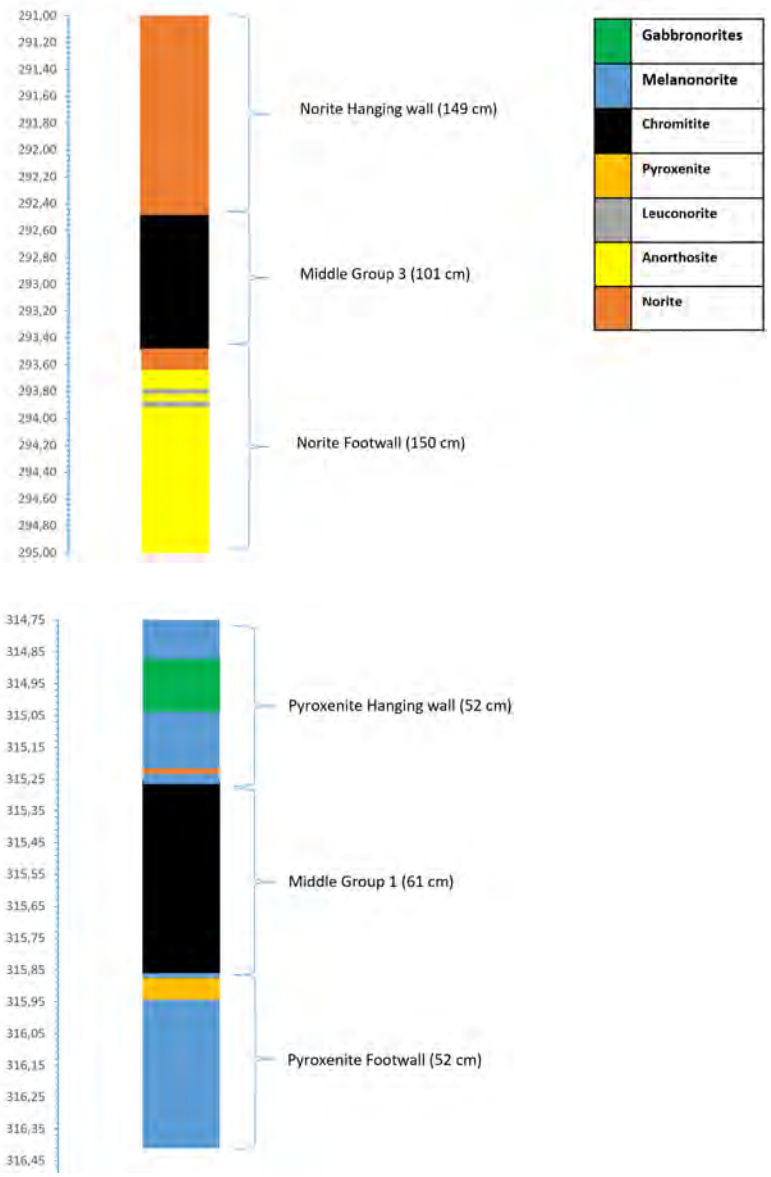

Figure 20. Stratigraphy determined from core KD 151 showing MG 3 & MG 1 chromitite layers with their associated HW (hangingwall) and FW (footwall).

4.4.1 Major and minor elements

There are positive straight-line correlations between SiO_2 vs MgO/Na_2O/CaO/MnO and MgO vs CaO and MnO plots, as seen in Figure 21; the MG 1 chromite layer has the lowest values of MgO with a spread of concentrations seen in the hangingwall along with the highest values recorded in the footwall. There are negative straight-line correlations observed in the SiO_2 vs Al_2O_3/TiO_2/FeO*/Cr_2O_3 and MgO vs Cr_2O_3/FeO*/Al_2O_3/TiO_2; the footwall samples in the plots mentioned above show the lowest concentrations for Al_2O_3, TiO_2, FeO* and Cr_2O_3. The MG 1 chromite layer has the highest concentrations, with a spread observed across the hangingwall samples. The K_2O and Na_2O concentrations follow along with the same trend for

both the SiO_2 and MgO Harker plots. The MG 1 chromite has the lowest concentrations of both oxides, with the hangingwall and footwall samples being spread out. The CaO plots reveal a gap in the footwall and hangingwall concentrations.

The MG 3 suite whole-rock samples are seen in Figure 22. There are bimodal positive straight-line correlations observed in the MgO vs FeO*/MnO/Cr_2O_3 and TiO_2, with the footwall samples having the lowest concentrations of those oxides with the hangingwall samples following a different trendline from the MG 3 chromite; the chromite trendline has the steeper slope gradient. There is a less pronounced positive correlation in the SiO_2 vs MgO/Al_2O_3/K_2O/Na_2O and CaO plots, with the footwall samples showing a general spread in concentrations with the hangingwall samples following a trendline linked to the MG 3 chromites. Negative bimodal straight-line correlations are observed in the MgO vs Cr_2O_3/Na_2O and CaO. One MG 3 chromite sample is trending with the footwall, whilst the remaining samples form a trend with the hangingwall.

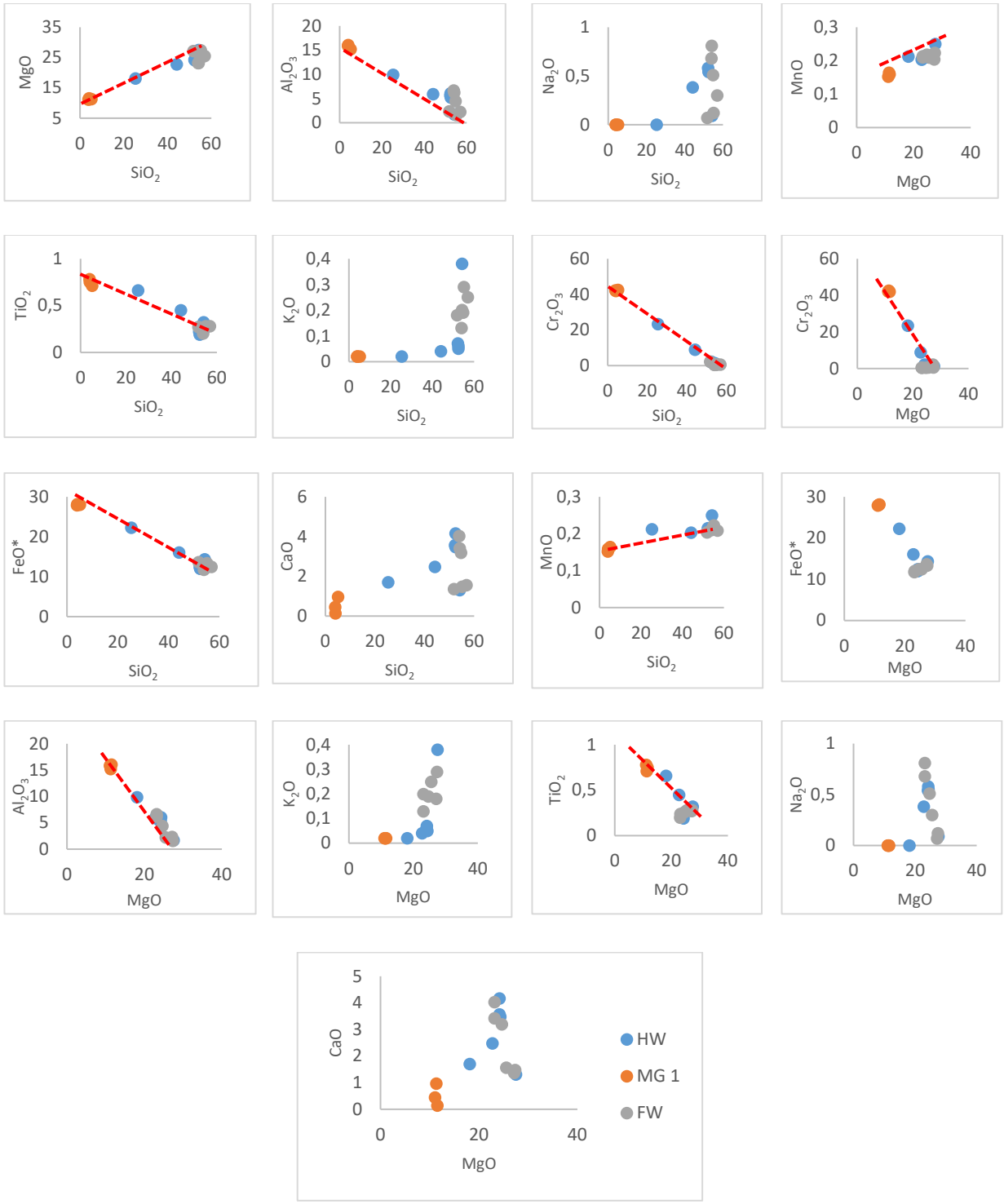

Figure 21. Whole-rock Harker diagrams across the MG 1 suite of rocks. All data in wt.% with the exception of FeO. FeO represents total Fe.*

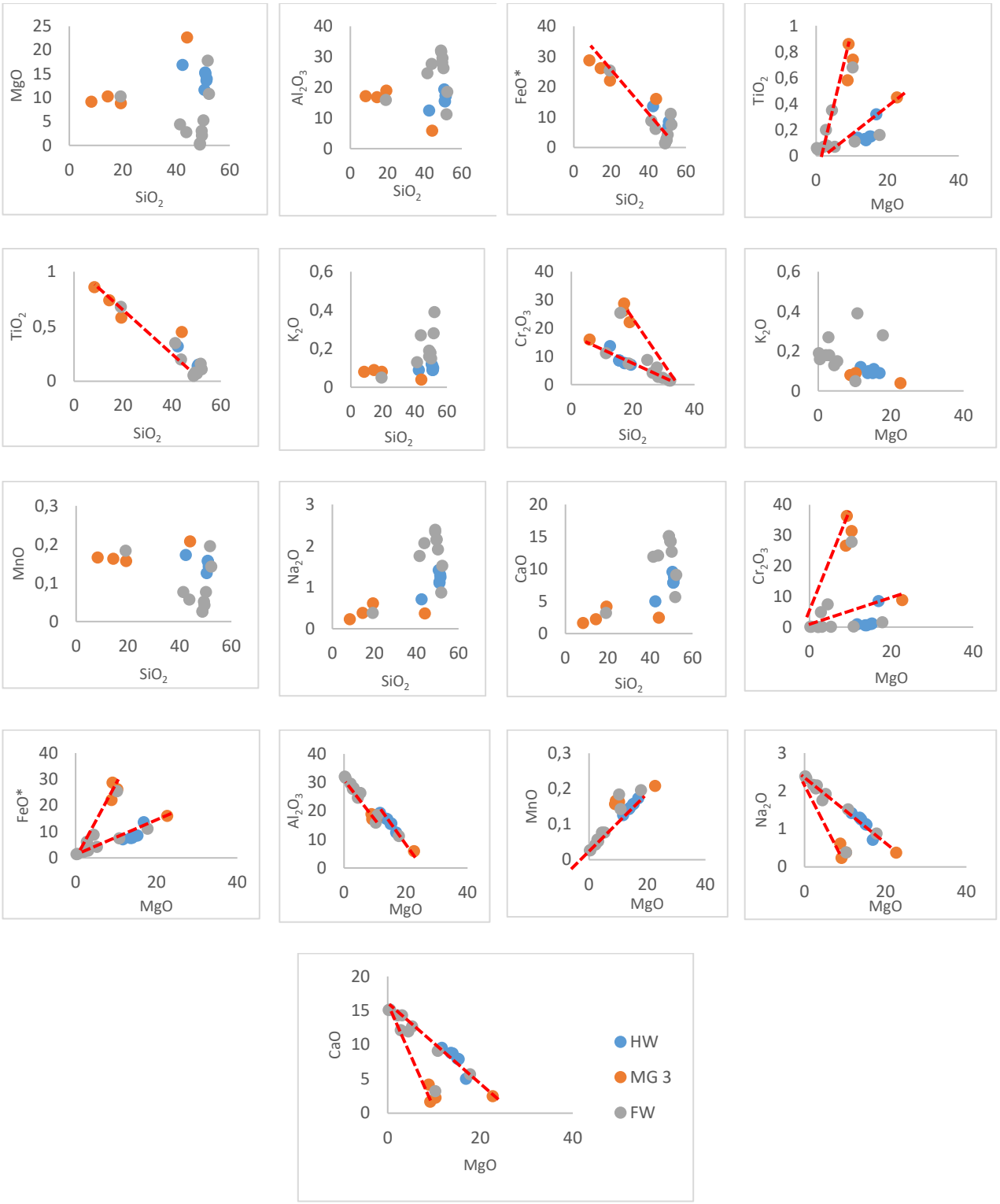

Figure 22. Whole-rock Harker diagrams across the MG 3 rock suite. All data is in wt.% with the exception of FeO. FeO represents total Fe.*

4.4.2 Transition trace elements

Higher Cr concentrations are observed in the chromite layer, with the hangingwall samples having a greater concentration than the footwall in both the MG 3 and 1 suite (Figure 23). There is a subtle increase in Cr concentrations of the footwall as it approaches the chromite; this is seen in both suites. The Ni concentrations for the MG 3 chromite layer show a decrease with depth, and the hangingwall has a higher concentration than the footwall with a peak indicating a chromite stringer. The MG 1 Ni concentrations show a peak at the centre of the chromite. The hangingwall and footwall have a vague decrease in concentrations with depth, with the hangingwall having higher overall Ni concentrations. The Sc concentrations across the MG 3 suite of rocks show peaks at the base and top of the chromite, and the footwall has a general decrease with depth, although samples show alternating increases and decreases in concentrations.

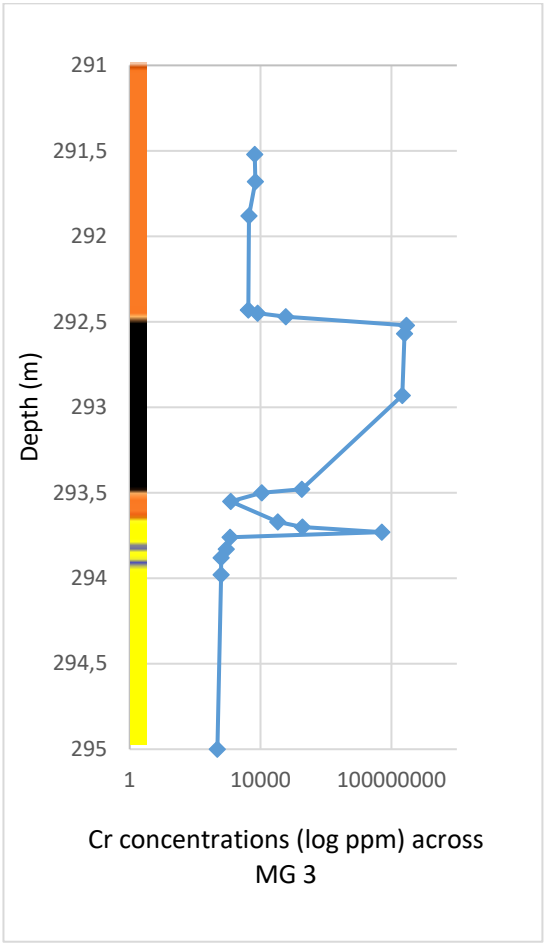

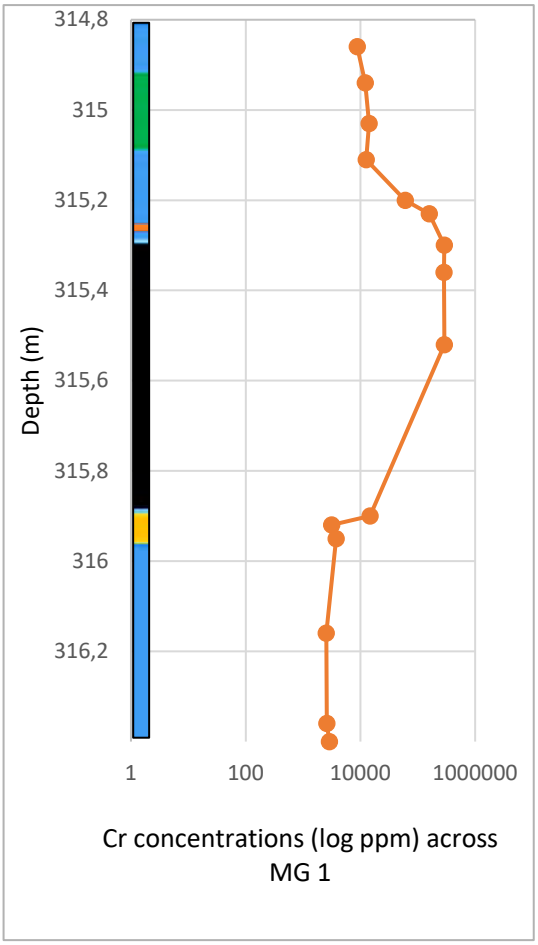

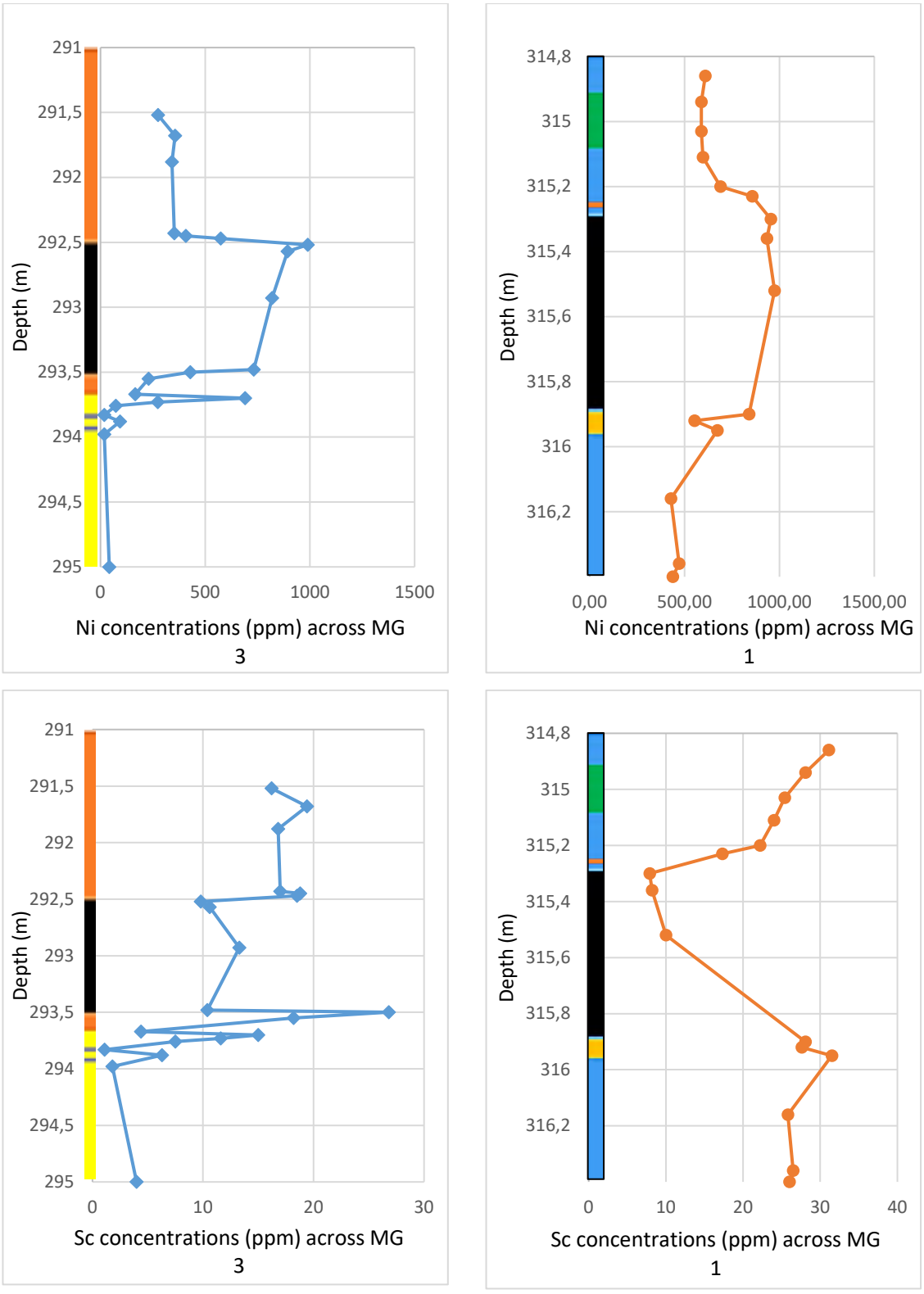

Figure 23. Cr, Ni and Sc whole-rock concentrations across the MG 3 and MG 1 suite of rocks.

The Cu concentrations across the MG 3 chromitite layer show a decrease with depth, and this, unlike the MG 1 chromitite, shows an increase with depth (Figure 24); the total concentration of Cu is more significant in the MG 1 rock suite. The Co concentrations reached the peak

detection limit along the chromites. The MG 3 footwall rocks have lower Co concentrations than the hangingwall rocks whilst the MG 1 hangingwall and footwall have similar Co concentrations. The Ti concentrations across both the MG 3 and MG 1 chromites decrease with depth; the hangingwall of the MG 3 has a higher Ti than the footwall.

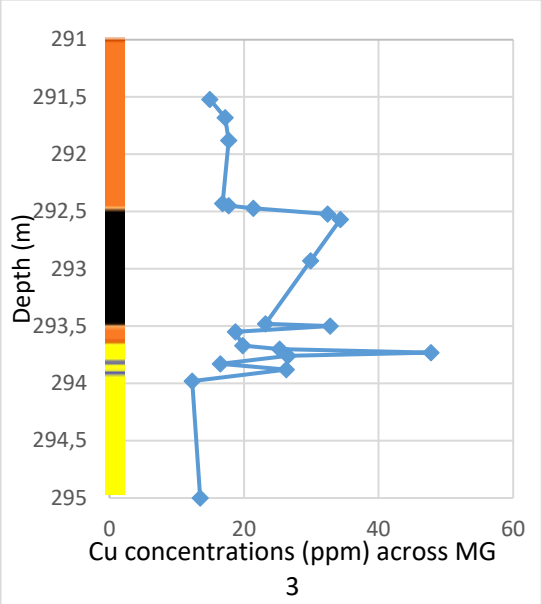

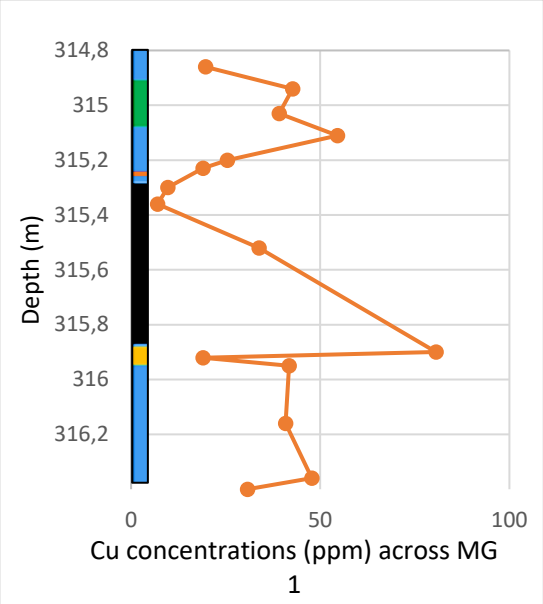

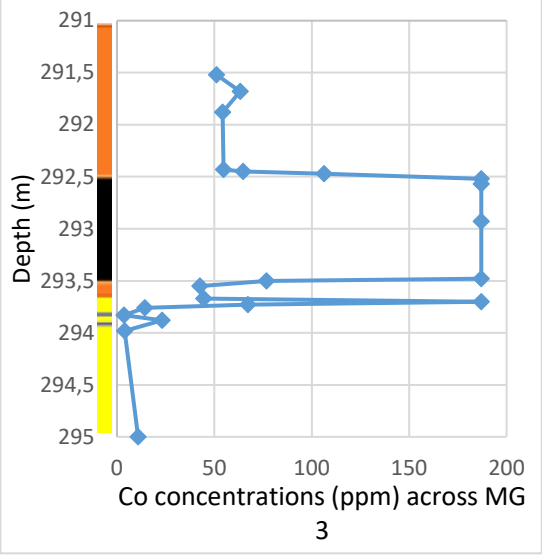

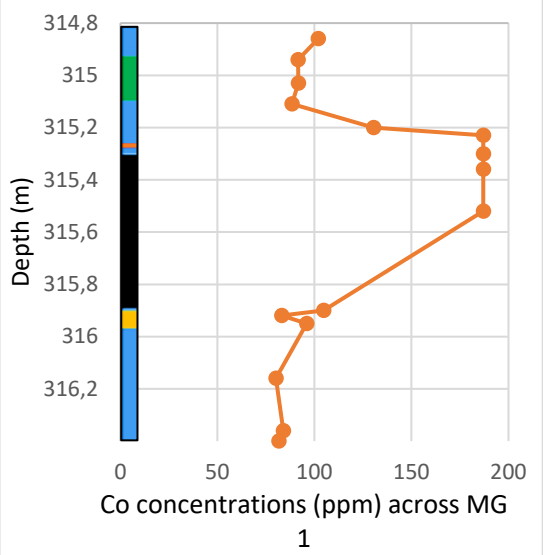

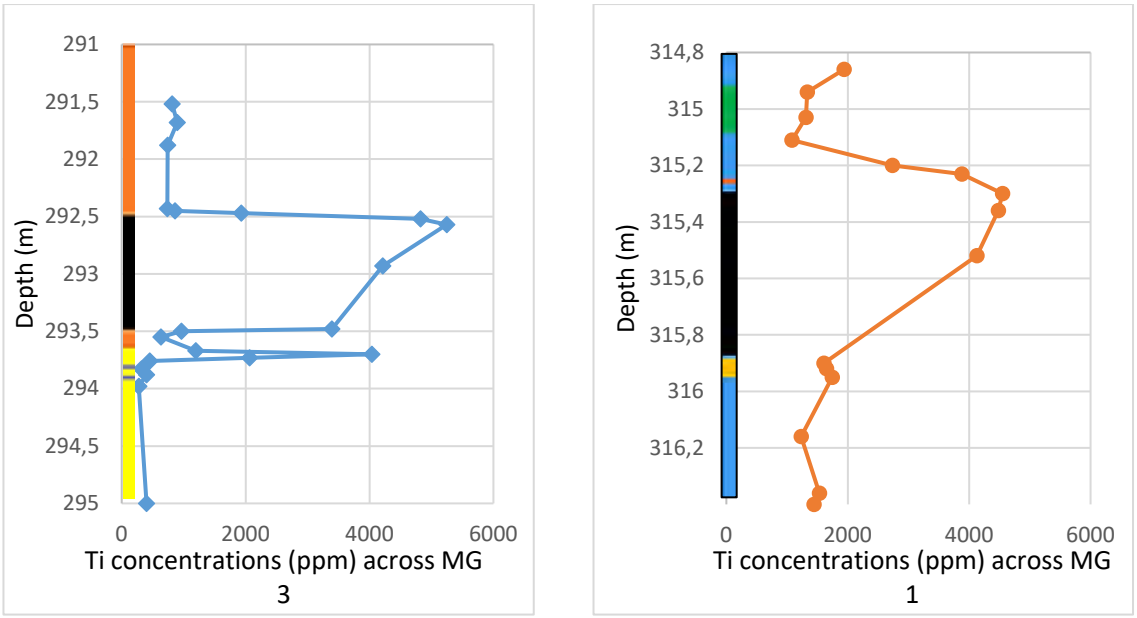

Figure 24. Cu, Co and Ti whole-rock concentrations across the MG 3 and MG 1 suite of rocks.

The MG 3 chromite decreases Zn concentrations with depth, with the footwall having a lower concentration than the hangingwall. The MG 1 chromite layer has constant Zn concentrations throughout, the hangingwall and footwall have similar Zn concentrations. The whole-rock V concentrations were not available for all the samples. The hangingwall samples for MG 1 have comparable V_2O_5 concentrations to the MG 3 chromite from the concentrations obtained. The Ni/Sc ratios plotted for the MG 3 suite of rocks reveal a saw tooth pattern along the footwall as the depth decreases. The ratio along the chromite shows an increase with decreasing depth, which is also observed for the hangingwall rocks (Figure 25). The MG 1 footwall shows a constant Ni/Sc ratio with an increase seen in the chromitite layer than a decrease in the hangingwall rocks.

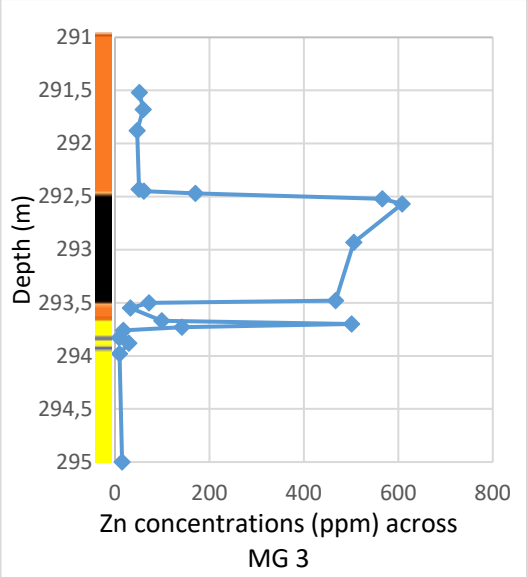
Depth (m)
291
291,5
292
292,5
293
293,5
294
294,5
295
0
200
400
600
800
Zn concentrations (ppm) across MG 3

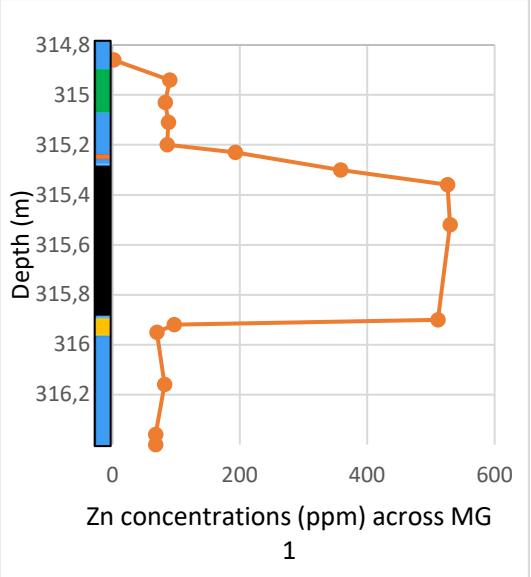
Depth (m)
314,8
315
315,2
315,4
315,6
315,8
316
316,2
0
200
400
600
Zn concentrations (ppm) across MG 1

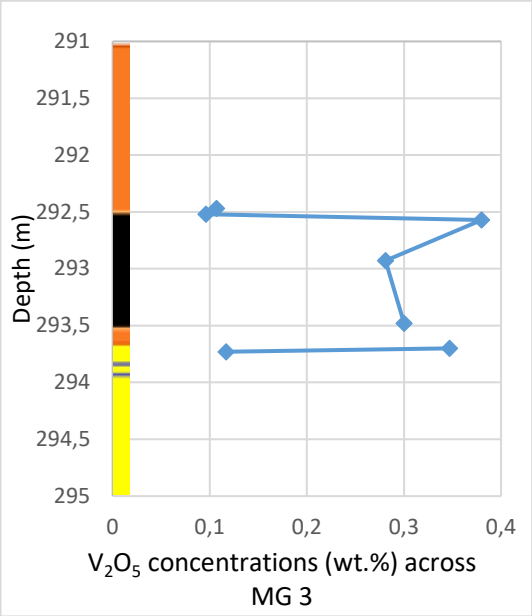
Depth (m)
291
291,5
292
292,5
293
293,5
294
294,5
295
0
0,1
0,2
0,3
0,4
V2O5 concentrations (wt.%) across MG 3

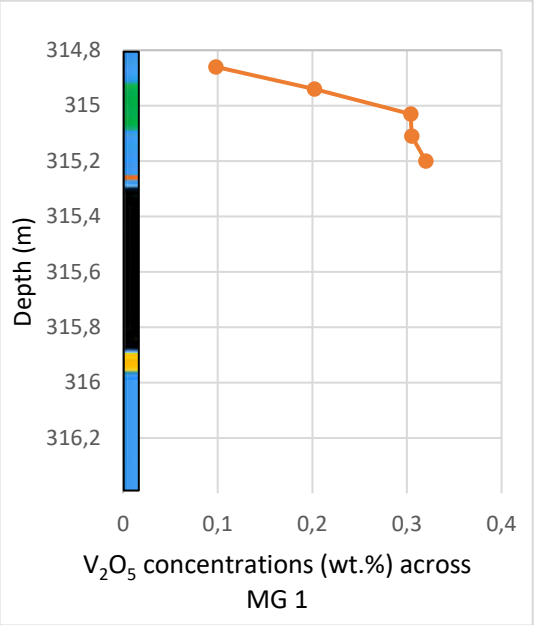
Depth (m)
314,8
315
315,2
315,4
315,6
315,8
316
316,2
0
0,1
0,2
0,3
0,4
V2O5 concentrations (wt.%) across MG 1

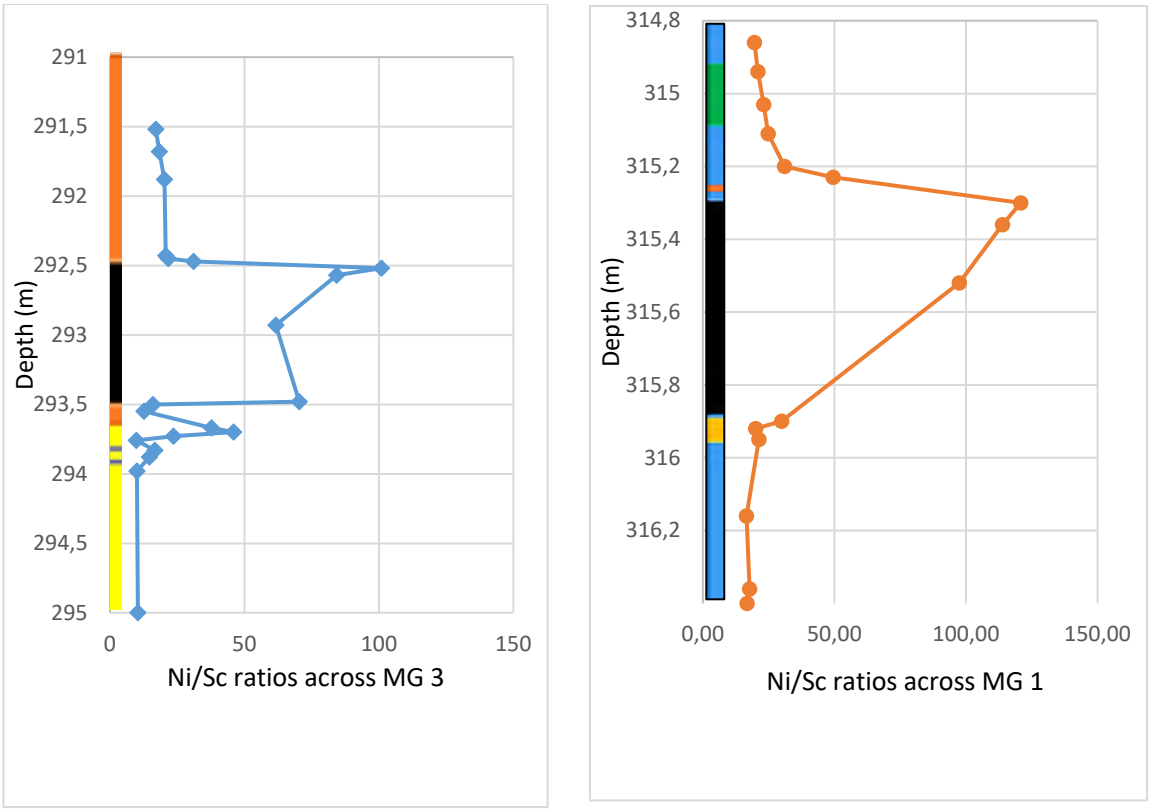

Figure 24. Zn, V_2O_5 (taken to represent V concentrations) and Ni/Sc ratios across the MG 3 and MG 1 suite of rocks.

4.4.3 Lanthanide trace elements

The following section of rare earth elements and incompatible element chondrite normalised plots use the values of (McDonough and Sun, 1995). The REE trends (Figure 26) observed in the MG 3 suite of rocks show enrichment of LREE relative to HREE across the suite of rocks. A flatter trend is observed for the HW and chromitite samples compared to the FW. The samples show a more considerable enrichment than chondrite when looking at the LREE, with strong positive Eu anomaly spikes observed throughout the suite of rocks (HW, chromitite and FW). The FW samples show a much higher Eu anomaly showing a substantial variation in the FW samples in the HREE portion of the plot. The REE trends observed (Figure 23) in the MG 1 suite of rocks are slightly less concentrated than the MG 3 samples in terms of REE compared to chondrite. The FW samples show a positive to a flat Eu anomaly compared to the HW, and chromitite samples show a strong positive Eu anomaly. A flatter curve shows a lesser LREE enrichment than the MG 3 samples; there is a slight variation in the grouping of the MG 3 FW, chromitite and HW samples.

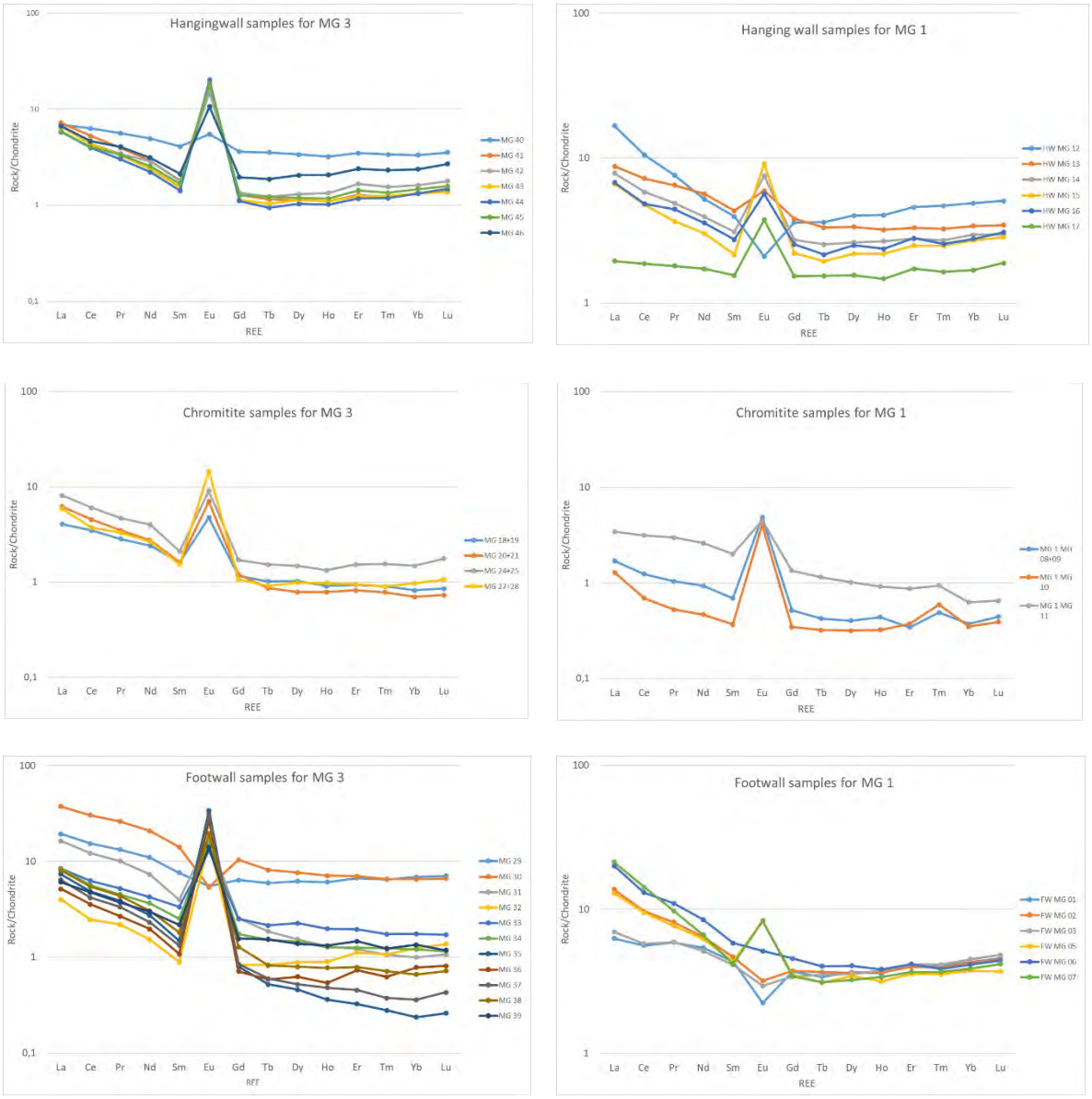

Figure 25. The range of chondrite normalised REE concentrations is normalised for the MG 1 and MG 3 rocks.

The observed trends for incompatible elements/chondrite plots (Figure 27) of the MG 3 rocks show spikes of enrichment for Ba, Sr, and Eu in the FW, chromitite and HW. There are observable depletion troughs for Nb, Sm and to a lesser extent Ti, but these are only seen in some FW samples. The variation between FW samples increases from elements Dy to Yb, but a minor variation is seen in the HW and chromitites. The trends for incompatible elements/chondrite plots (Figure 27) of the MG 1 suite of rocks show spikes of enrichment for Ba in the FW and HW samples and less so for the chromitites. Spikes are also observed in Ti with more apparent trends in the chromitites. There is a depletion of Sr along the FW, with most HW and chromitite samples showing an enrichment trend.

Figure 27. Incompatible element concentrations (chondrite normalised) for the MG 1 and MG 3 rocks.

4.5 Mineral geochemistry

The whole-rock samples provided great insight into the minerals present but to better understand the changes with the depths and rock types, and individual mineral grains were analysed with the results presented below.

4.5.1 Chromites

The observed trends for the chromites of the MG 3 suite (Figure 28) show the TiO_2 that ranges from 0.5-1.7 wt. % with the lowest concentration along the centre of the chromitite layer.

Higher FeO values are observed along the HW and FW of the chromitite suite, with lower values observed along the layer itself. The top portion of the chromitite has the lowest MgO and Al_2O_3, with a steady increase observed from the bottom contact upwards. The Mg# increases from the FW 27 to 45 wt.% in the central portion of the chromitite but then decreases to 18 wt.%. The Cr# mirrors the Mg# with a decrease from ~ 80-68 wt.% as the sampling horizon approaches the central portion of the chromitite from the FW. There is then an increase to ~85 wt.% along the HW chromitites. The Cr_2O_3 values are constant with the concentrations of the samples from ~50-60 wt.%.

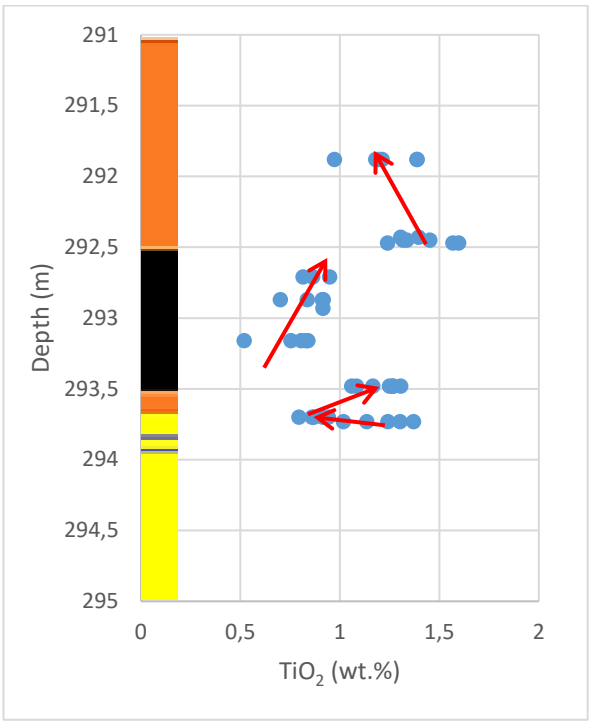

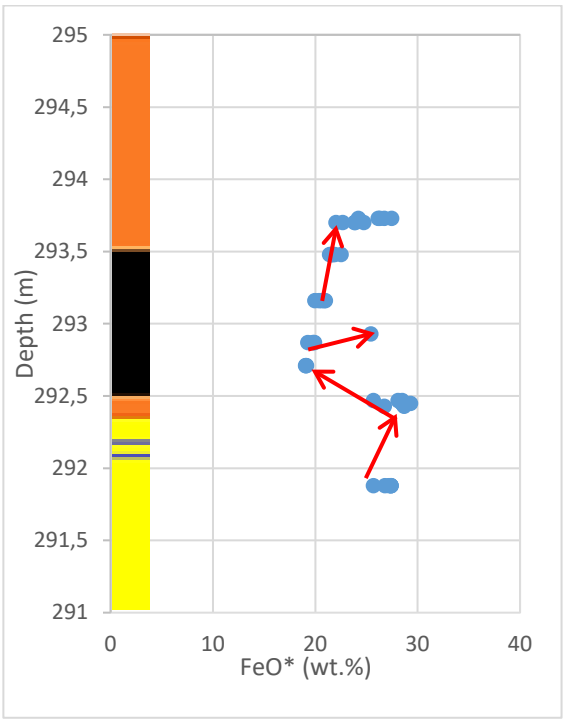

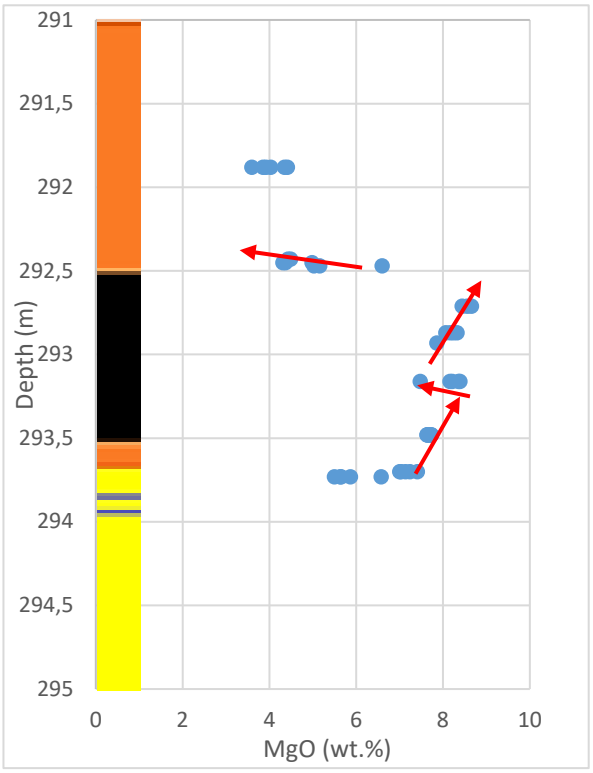
291
291,5
292
292,5
293
293,5
294
294,5
295
Depth (m)
0
2
4
6
8
10
MgO (wt.%)

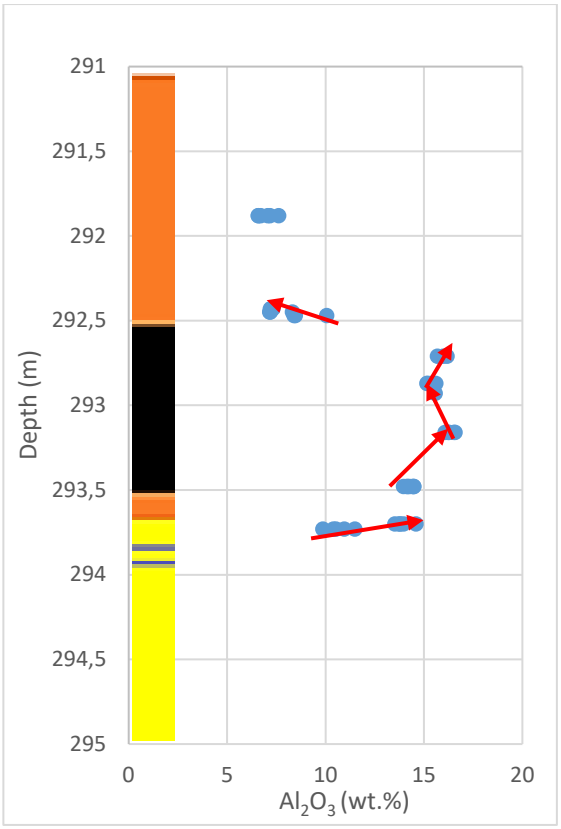
291
291,5
292
292,5
293
293,5
294
294,5
295
Depth (m)
0
5
10
15
20
Al2O3 (wt.%)

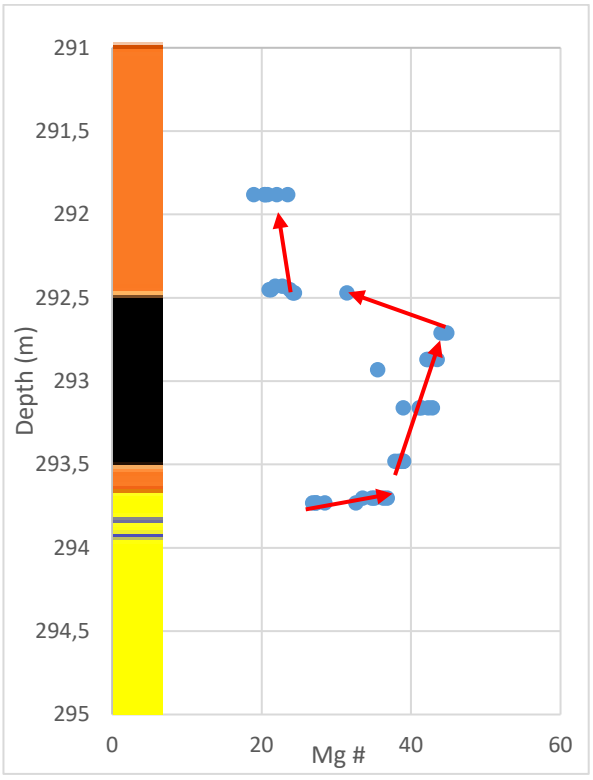
291
291,5
292
292,5
293
293,5
294
294,5
295
Depth (m)
0
20
40
60
Mg #

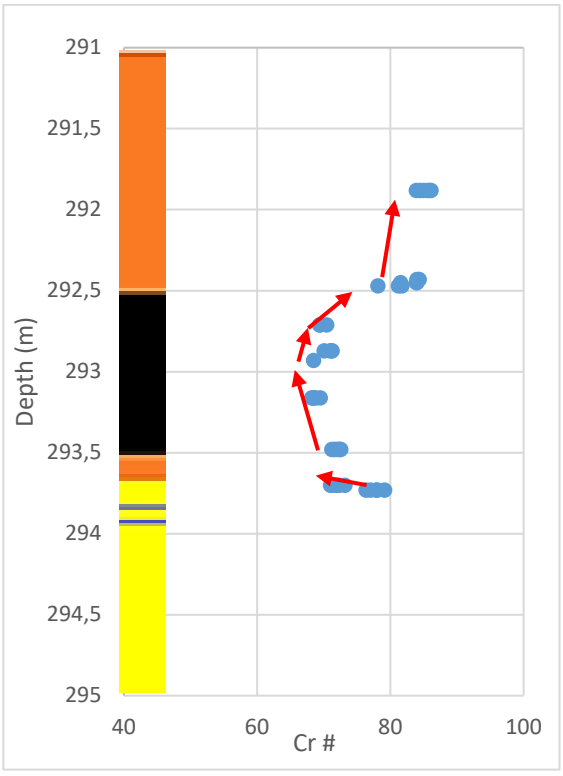
291
291,5
292
292,5
293
293,5
294
294,5
295
Depth (m)
40
60
80
100
Cr #

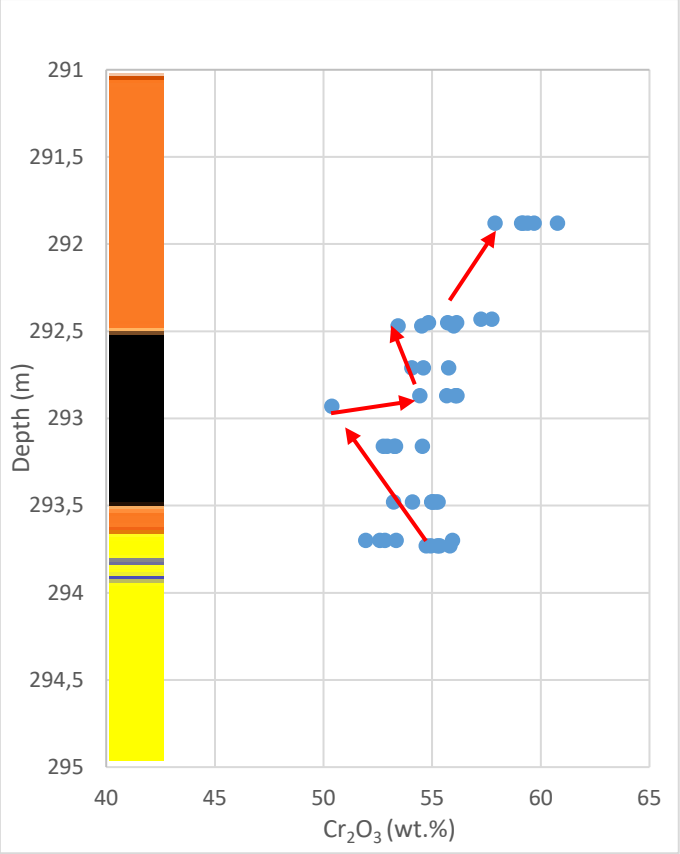

Figure 26. MG 3 chromite mineral chemistry. Red lines indicate potential trends.

The MG 1 chromites (Figure 29) TiO_2 values range from 0.8 – 2.8 wt. %, with no discernible trend, observed through the rock suite. The FeO values range from 17 – 28 wt. %, with the chromitite having the lowest amount and the FW and HW having higher concentrations. The MgO values ranged from 3- 9 wt. %, the FW has the lowest values, with the chromitite having the most significant values; the HW values were more significant than the FW. The Al_2O_3 in the HW has the lowest values at 9 wt. % with the chromitite and HW values ranging from 11 – 16 wt. %. The Mg# and Cr# ranged from 18 – 50 and 68 – 81, respectively.

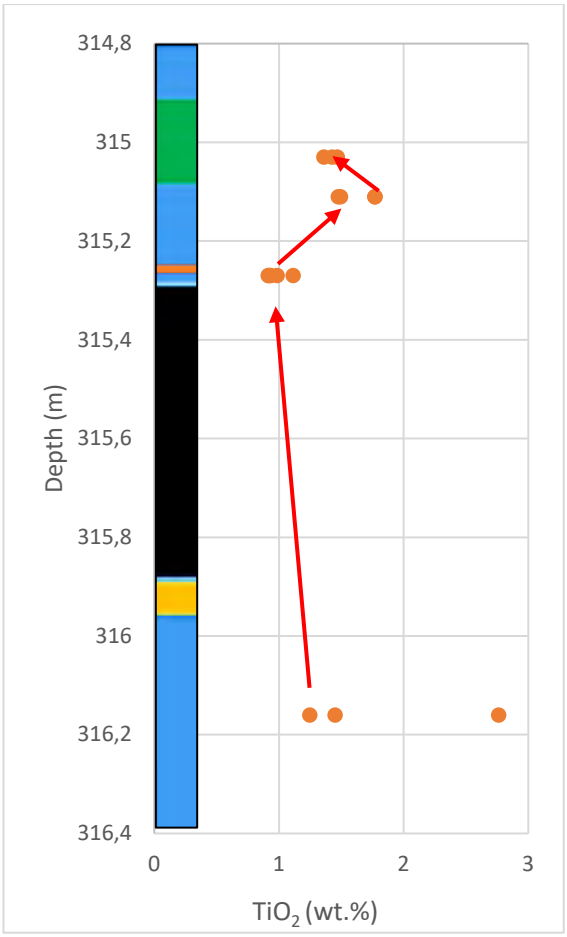
314,8
315
315,2
315,4
315,6
315,8
316
316,2
316,4
Depth (m)
0
1
2
3
TiO2 (wt.%)

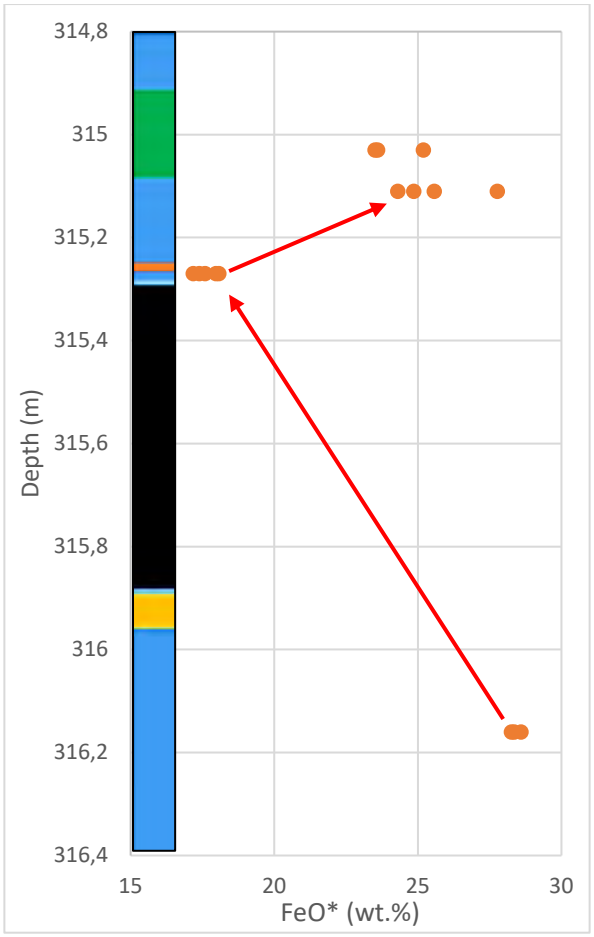
314,8
315
315,2
315,4
315,6
315,8
316
316,2
316,4
Depth (m)
15
20
25
30
FeO* (wt.%)

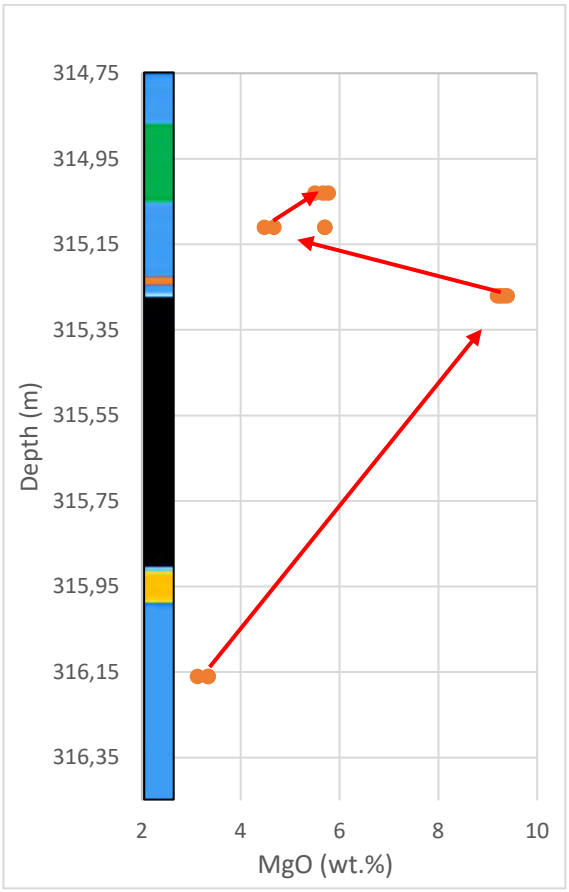
314,75
314,95
315,15
315,35
315,55
315,75
315,95
316,15
316,35
Depth (m)
2
4
6
8
10
MgO (wt.%)

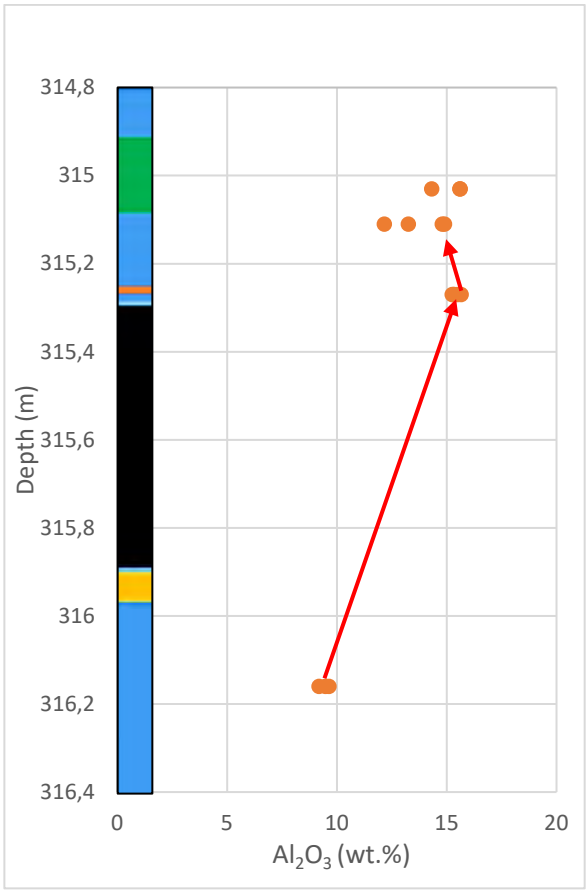
314,8
315
315,2
315,4
315,6
315,8
316
316,2
316,4
Depth (m)
0
5
10
15
20
Al2O3 (wt.%)

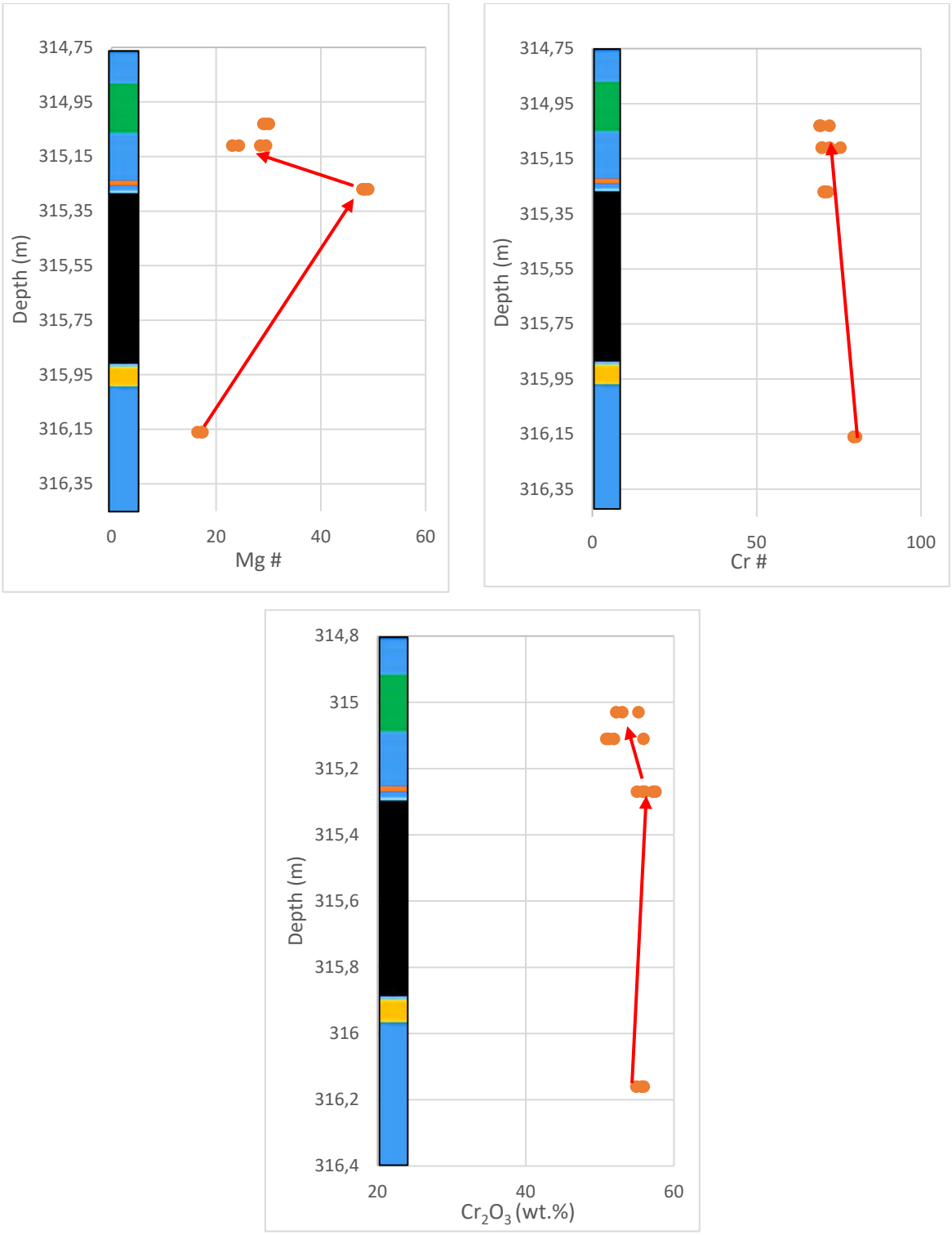

Figure 27. MG 1 chromite mineral chemistry. Red lines show potential trends.

The chromitites' TiO_2 values ranged from 0.5-1.5 wt.% and were too low to infer a trend. The FeO values ranged from 19-30 wt.%, showing a decrease from the FW through to the MG 3 and increases in the HW. The MgO (3.5-10 wt.%) and Al_2O_3 (6-16 wt.%) values show a trend opposite to the FeO, with smaller values observed in the HW rather than in the MG 3 and FW.

The MG# (15-45 wt.%) indicates a slight increase within the chromite itself, decreasing in the FW. The Cr # (70-80 wt.%) and the Cr_2O_3 (50-60 wt.%) values for the chromitites are constant in the MG 3 suite of rocks.

4.5.2 Pyroxenes

The mineral chemistry trends observed for the MG 3 pyroxenes (Figure 30) show that the SiO_2 values of the FW are lower than the concentrations of the HW. The HW shows an initial increase from the contact with the chromitite to a decrease. The Al_2O_3 mimics the pattern of the SiO_2 in the MG 3. The MgO concentrations fall between a narrow range (26-33 wt.%) with the highest values in the HW. The CaO concentrations fell between 0.3-3 wt.%, with two samples in the HW showing a wide distribution. These could potentially be values taken adjacent/to the inclusions associated with the pyroxenes. Higher FeO concentrations are along the FW. The En values range from 70-86 wt.%, with the highest values present in the HW.

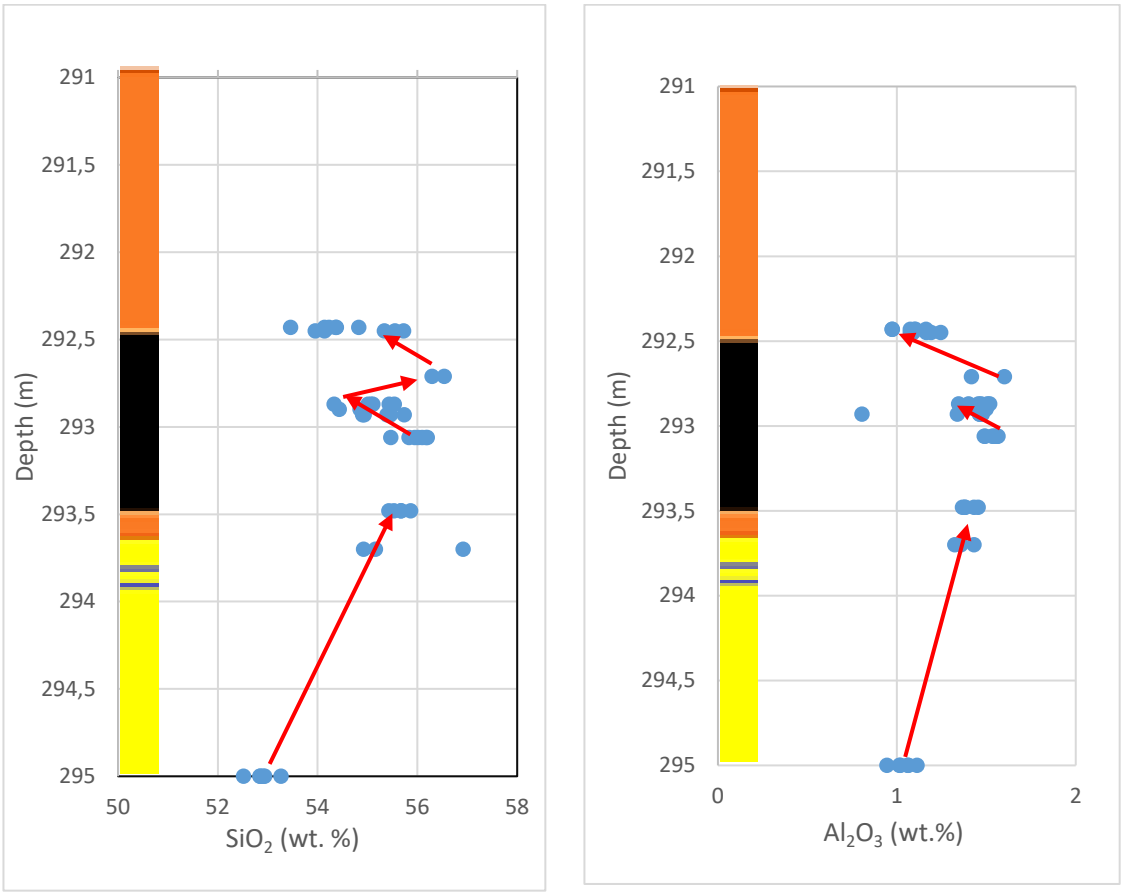

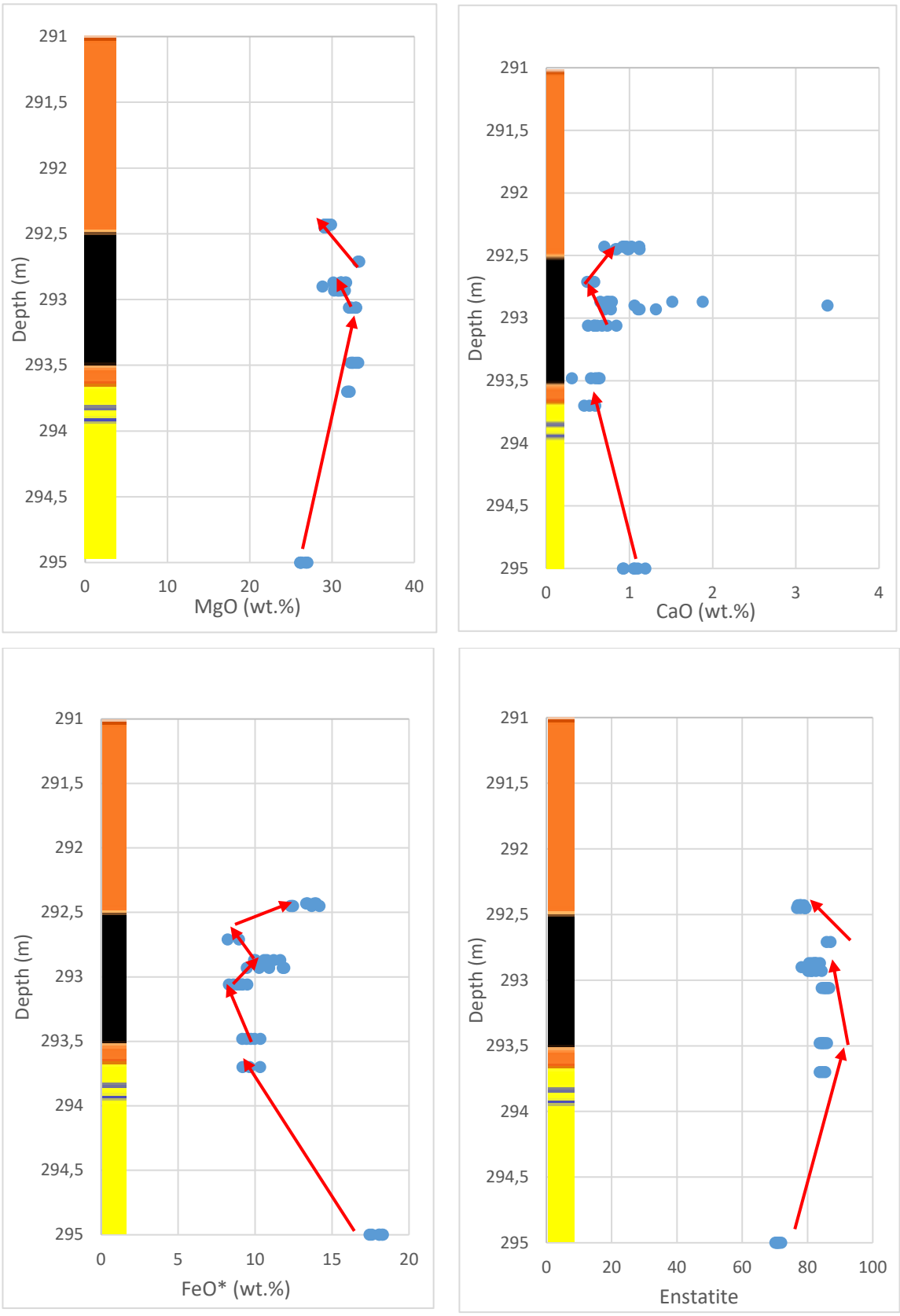

Figure 30. MG 3 Pyroxene chemistry. Red arrows indicate the direction of the trend.

The SiO_2 contents in the HW of the MG 1 suite (Figure 31) are substantially greater than in the FW and increase downwards the closer the samples are to the chromite layer. The Al_2O_3 concentrations are low throughout the samples with no conclusive trends identified, and the CaO concentrations in the MG 1 samples are similarly scattered and represent no sort of trend with depth. The MgO values of the HW show a higher concentration than in the FW. The FeO concentrations of the pyroxenes show a decrease in the HW, with a trend observed with the En content in the HW.

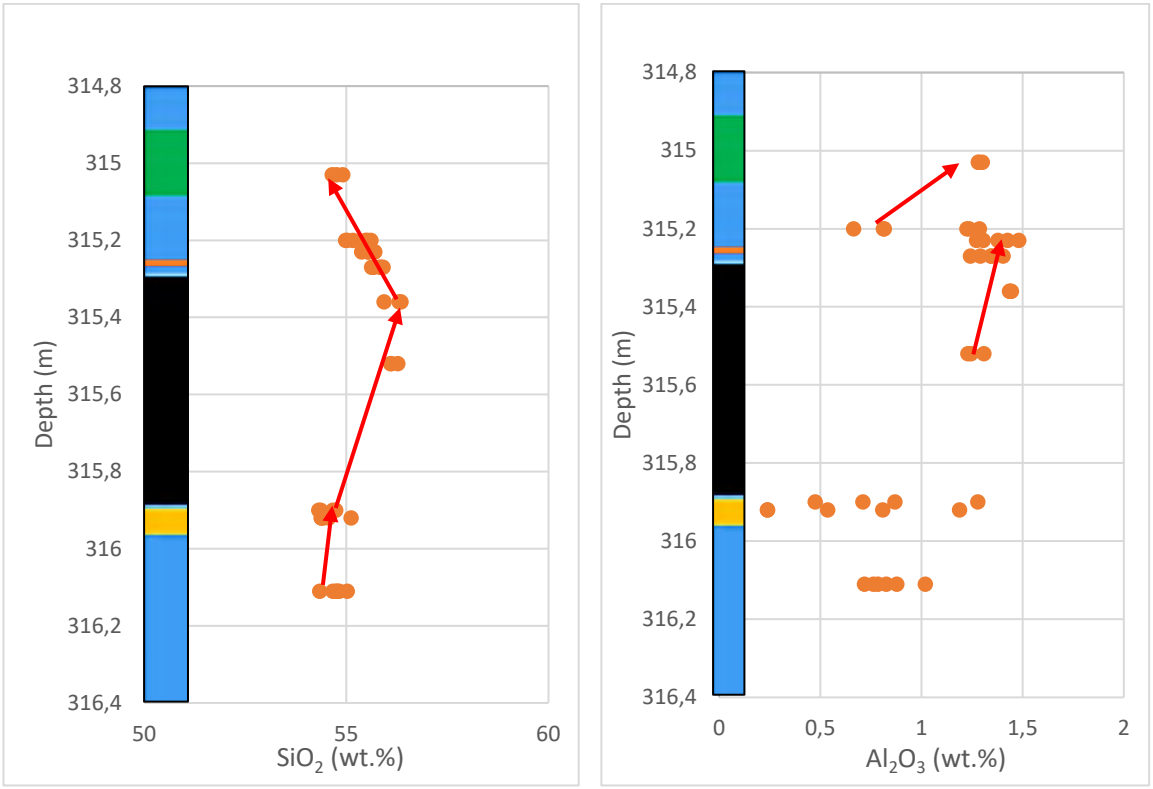

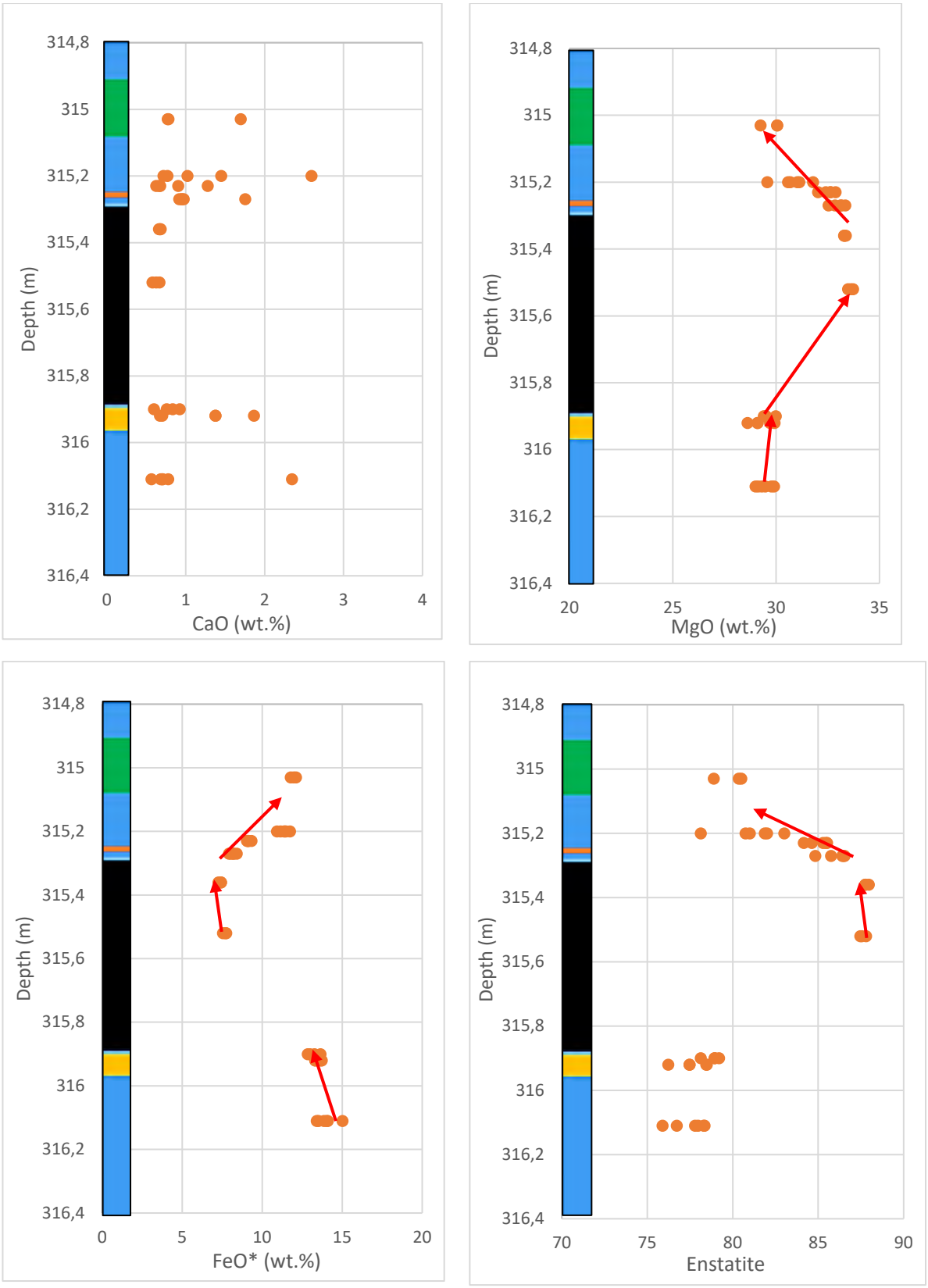

Figure 31. MG 1 pyroxene chemistry with the red arrows indicating the potential trends.

Figures 32 and 33 below show the pyroxene compositions of the MG 1 and MG 3 suite, respectively. Enstatite is the primary pyroxene composition of the MG 1 samples, with the

chromitite samples being more Mg-rich than the HW and FW. The MG 3 suite of rocks shows a more Ca and Fe-rich enstatite.

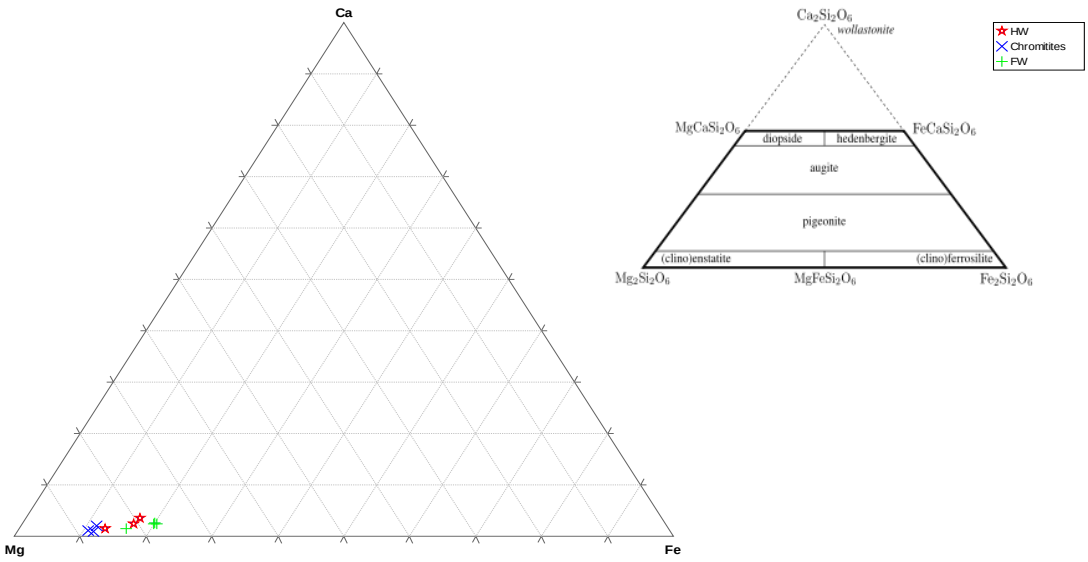

Figure 32. Ternary diagram showing the pyroxene compositions for MG 1 suite of rocks.

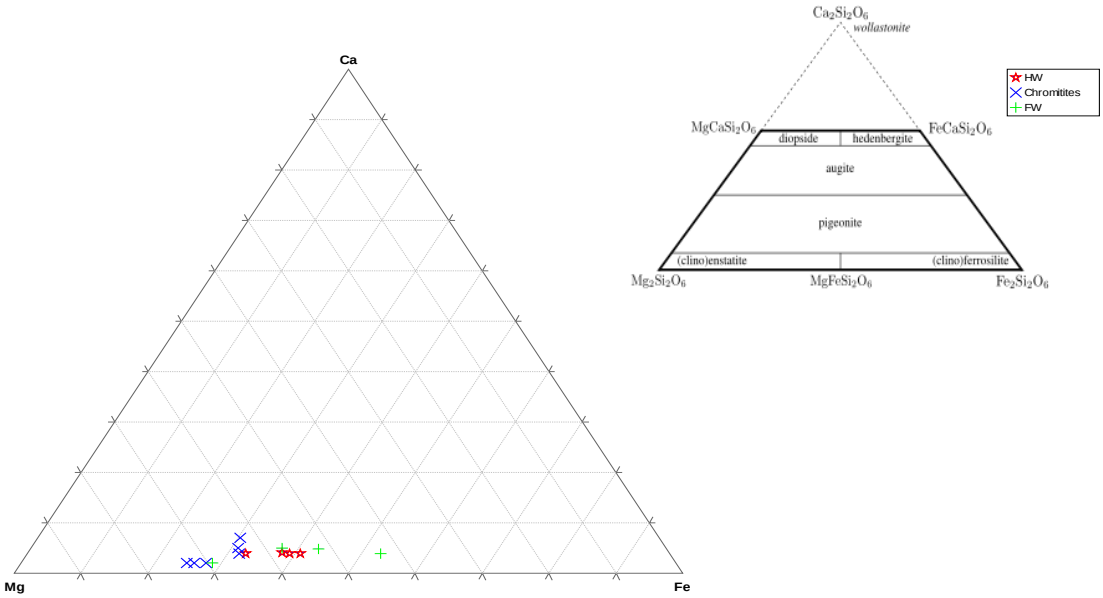

Figure 33. Ternary diagram showing the pyroxene compositions for MG 3 suite of rocks.

4.5.3 Plagioclase

The plagioclase chemistry is constant across the MG 3 suite (Figure 34) relative to the sampling positions from the FW, chromitite and HW, with values for SiO_2 and Al_2O_3 increasing and decreasing in values within the chromite seam. The CaO and Na_2O are relatively constant when comparing the HW, MG 3 and FW. The An # shows a slight decrease in the MG 3 layer.

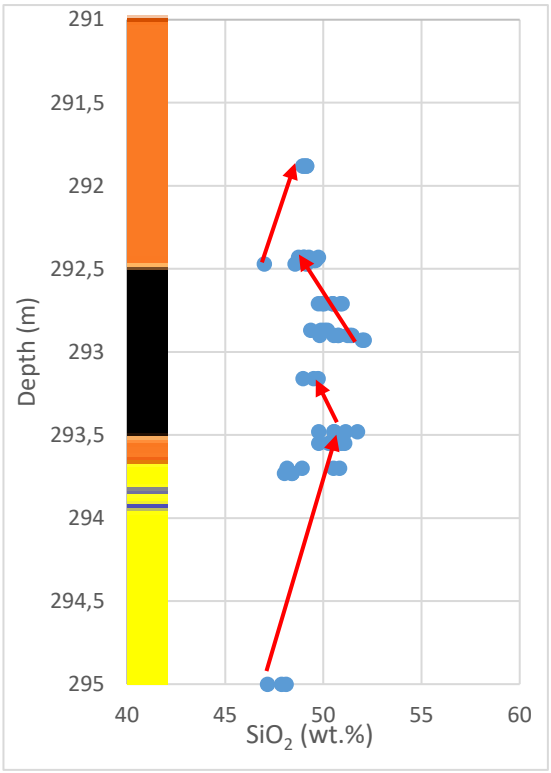

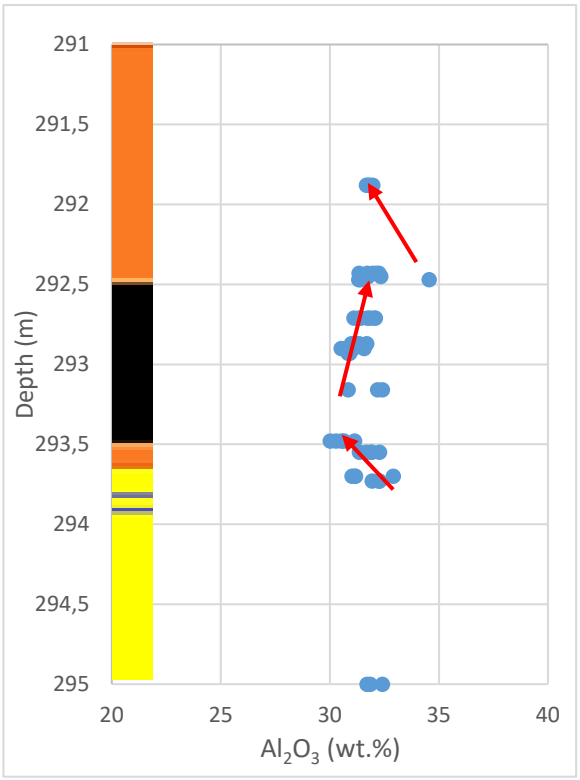

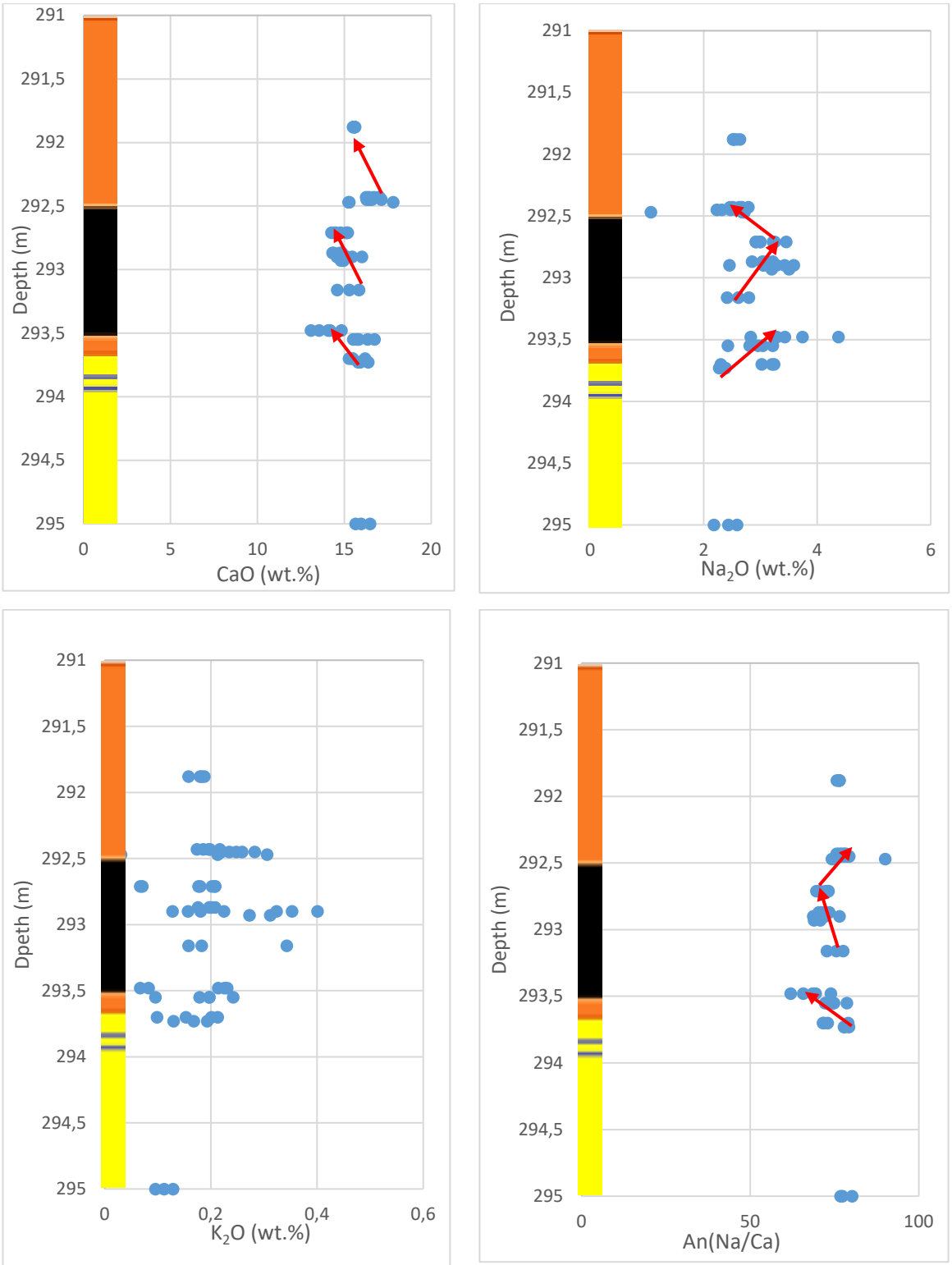

Figure 34. MG 3 Plagioclase chemistry. Red lines indicate a potential trend.

The plagioclase chemistry of the MG 1 suite of rocks is represented in Figure 35, the SiO_2 wt. % ranged from 45 – 54, the values across the FW, chromitite and HW are very similar. The values of Al_2O_3 ranged from 29 – 34 wt. %, slight differences were observed between the FW, chromitite and HW. The CaO values ranged from 12 – 19 wt. %. The Na_2O values ranged from

1 – 4 wt. %. The K_2O amount ranged from values of < 1 wt. % to 0.4 wt. %. The An content ranged from 60 to 90, the An content of the chromitite layer was the highest, with the FW and HW having similar values.

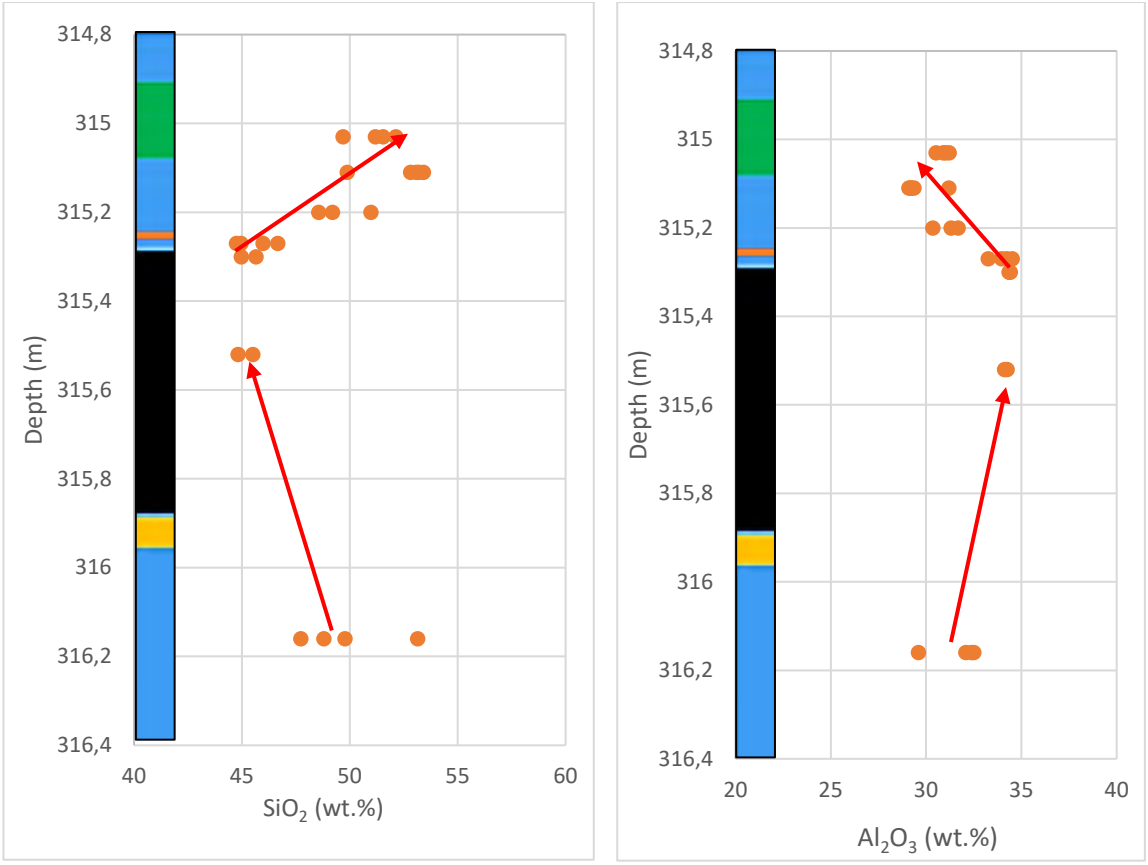

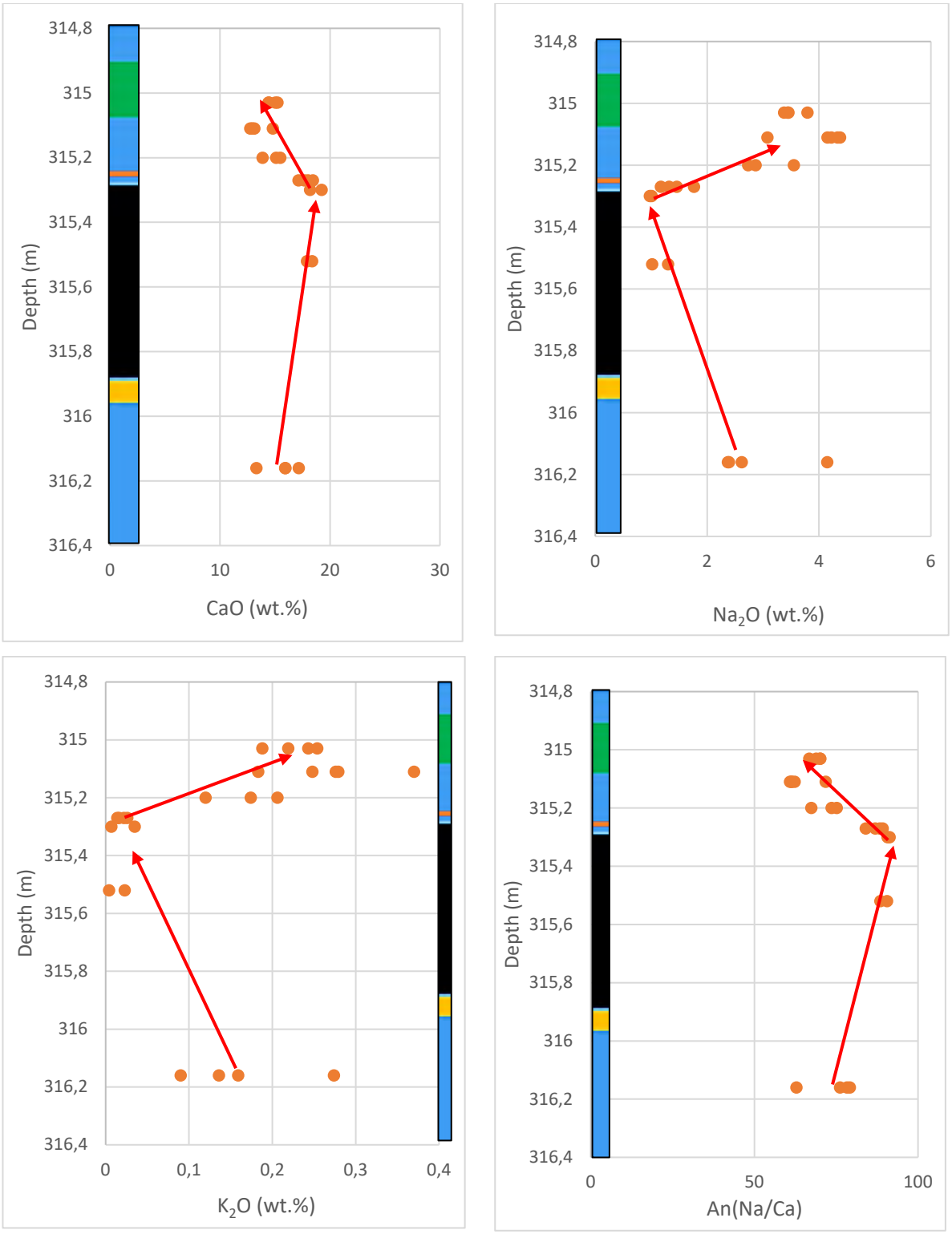

Figure 35. MG 1 Plagioclase chemistry, red lines indicate a potential trend.

The compositions of the plagioclase found in the MG 1 chromitite is more Ca-rich, plotting in the anorthite region of the ternary plot (Figure 36). The HW and FW samples all fall within the anorthite to bytownite region of the plot. The compositions of the plagioclase observed in the MG 3 suite of rocks all fall tightly within the anorthite region of the ternary plot (Figure 37).

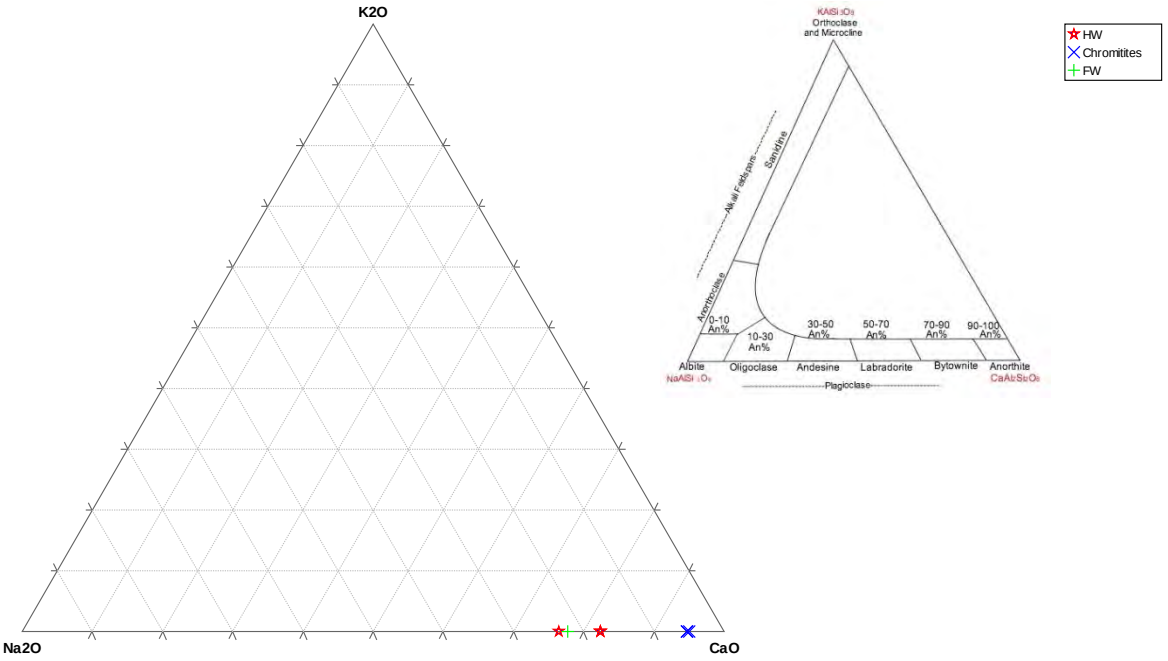

Figure 36. Ternary diagram plotting the compositions of plagioclase across the MG 1 suite.

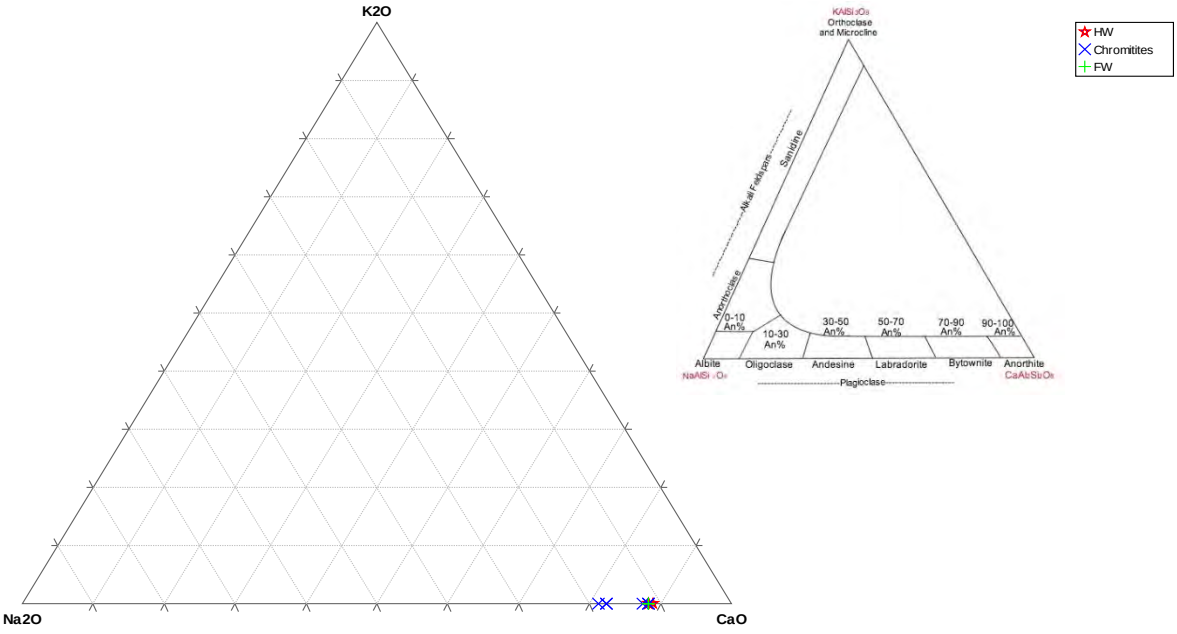

Figure 37. Ternary diagram plotting the compositions of plagioclase across the MG 3 suite.

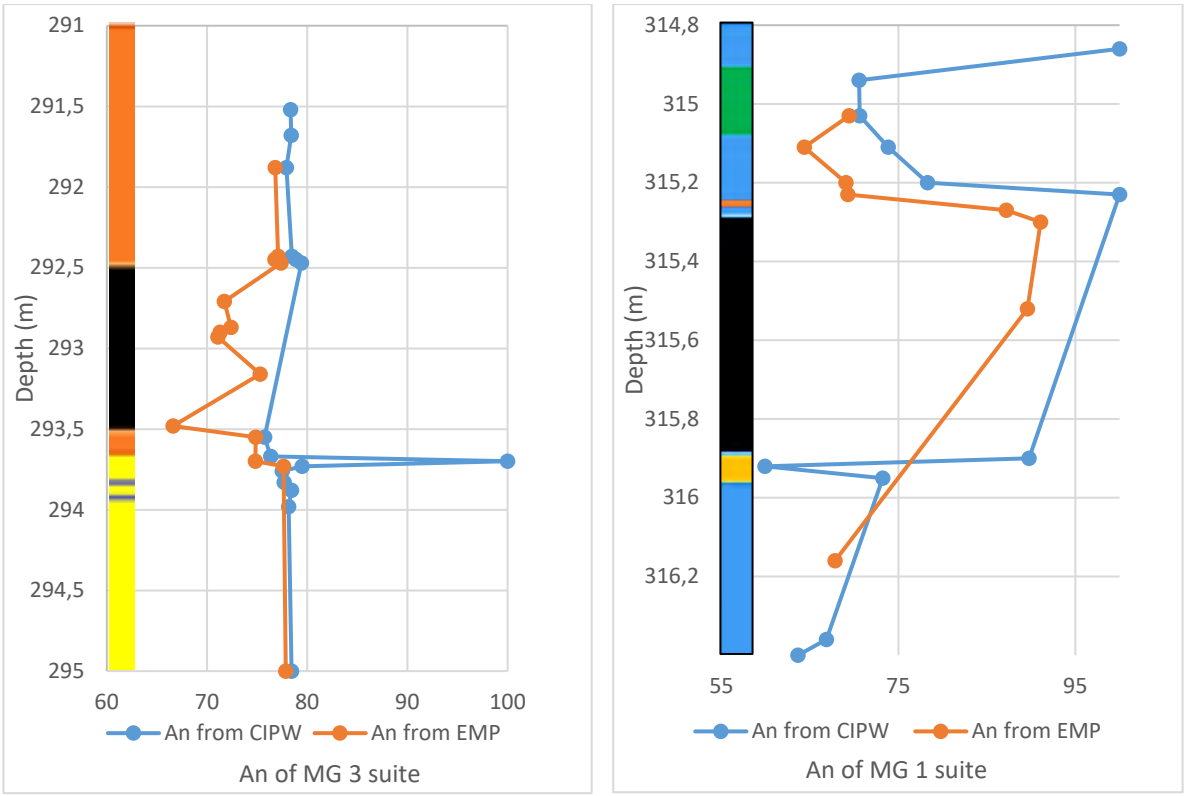

Figure 38. Graphs were comparing the An content of the plagioclase grains and whole-rock CIPW.

The plagioclase trends were tracked, and both modal proportions and WR Al_2O_3 were plotted (Figure 38). Regarding plagioclase/orthopyroxene modal ratios (Figure 39), the MG 3 FW has a higher ratio than the HW. The MG 1 shows higher ratios in the HW than the FW. There is a high Al_2O_3 content in the FW of the MG 3 suite than in the HW, whilst the reverse is valid for the MG 1 suite with a higher Al_2O_3 content in the HW and lower than the FW (Figure 40). The proportion of plagioclase in the various cyclic units of the UCZ is hugely variable, with the lowest proportions of 11 % to 85 %.

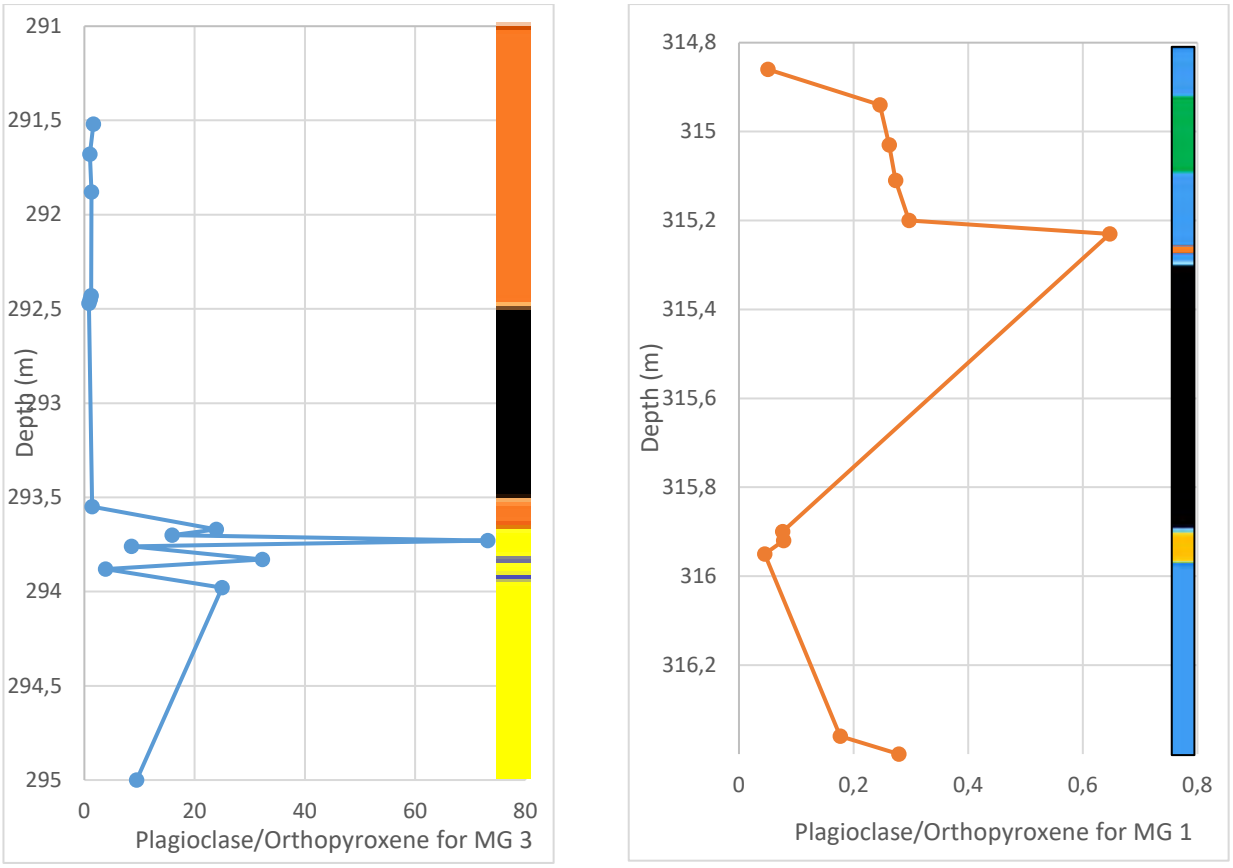

Figure 39. Plagioclase/Orthopyroxene modal ratios were determined from point counting for the MG 3 and MG 1 rock suites.

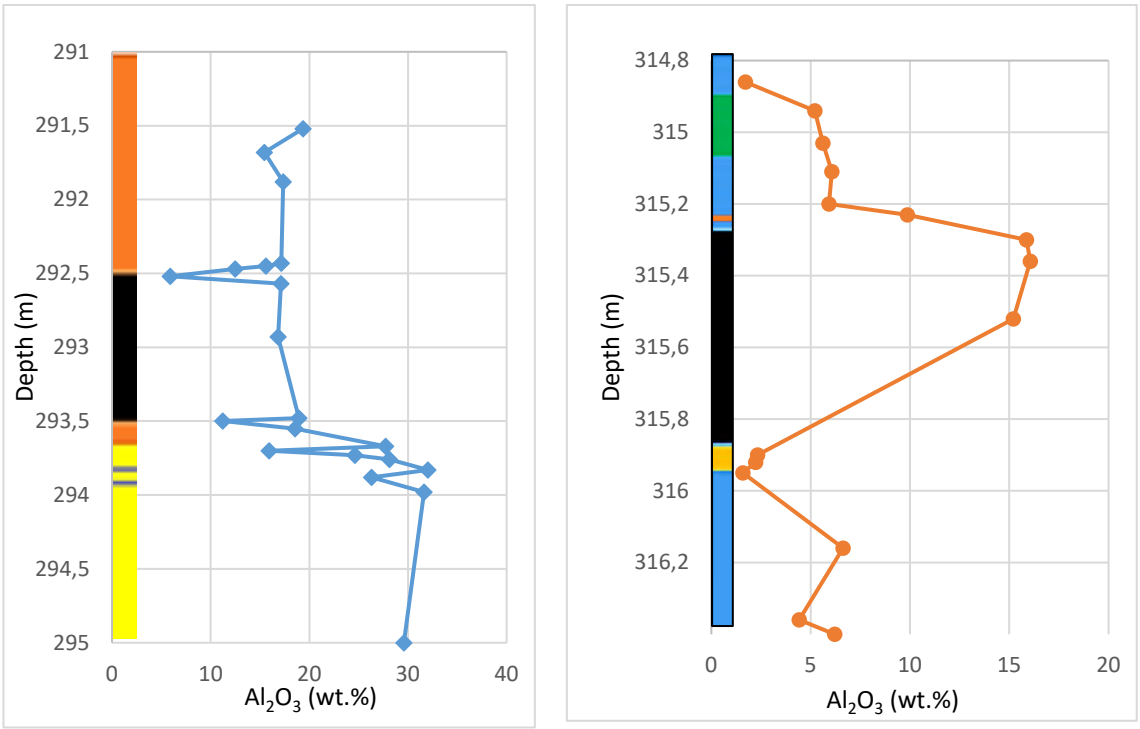

Figure 40. Plot of WR % (Al_2O_3) chemical analysis vs depth. MG 3 and MG 1 chromitite layer.

4.5.4 PGE analysis

The triplots below show the PGE profile types for the MG 3 chromitites (Figure 41) as more Pt and Pd rich than Rh; the FW has the most Pt-rich species, and the most Pd rich one with the HW spread across. The PGE species found in the chromitite plots with the FW samples in the Pt-rich area of the plot.

The MG 1 (Figure 42), in general, is slightly more Rh and Pt rich in species than the samples in the MG 3. The HW rocks show the highest values for Rh and Pt; the species within the chromitites are more Pt rich, with the FW rocks having the lowest values of Rh and the highest values for Pd.

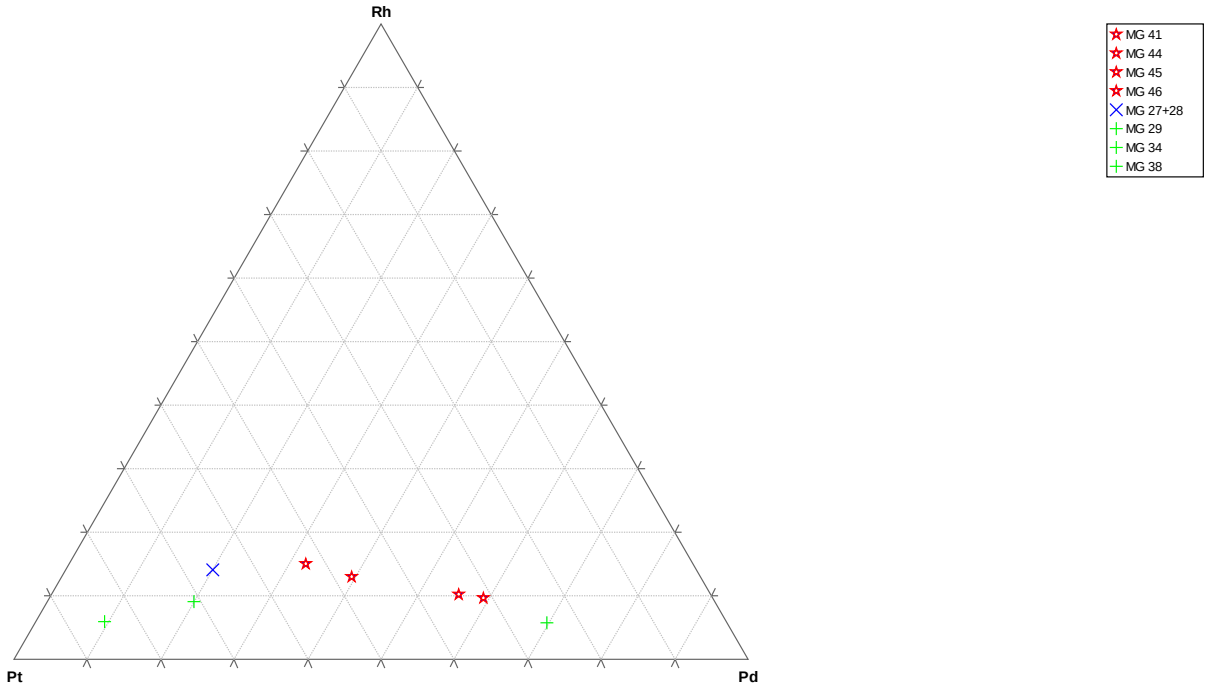

Figure 41. Triplot showing the PGE species in the rocks of the MG 3 suite.

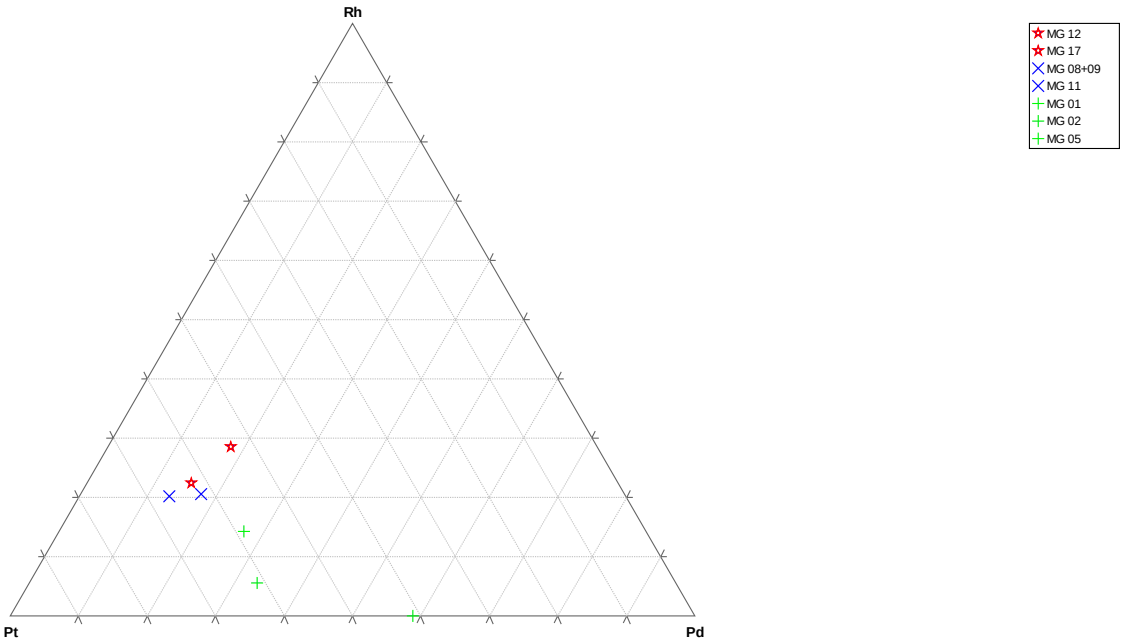

Figure 42. Triplot was showing the PGE species in the MG 1 rock suite.

By using bivariate plots (Figure 43), it was observed that the chromitites are more Ru and Rh rich than the HW (apart from a single analysis) and FW rocks, which tend to cluster in the lower values. There is also higher Pt and Pd in the chromitites with negligible amounts of Au.

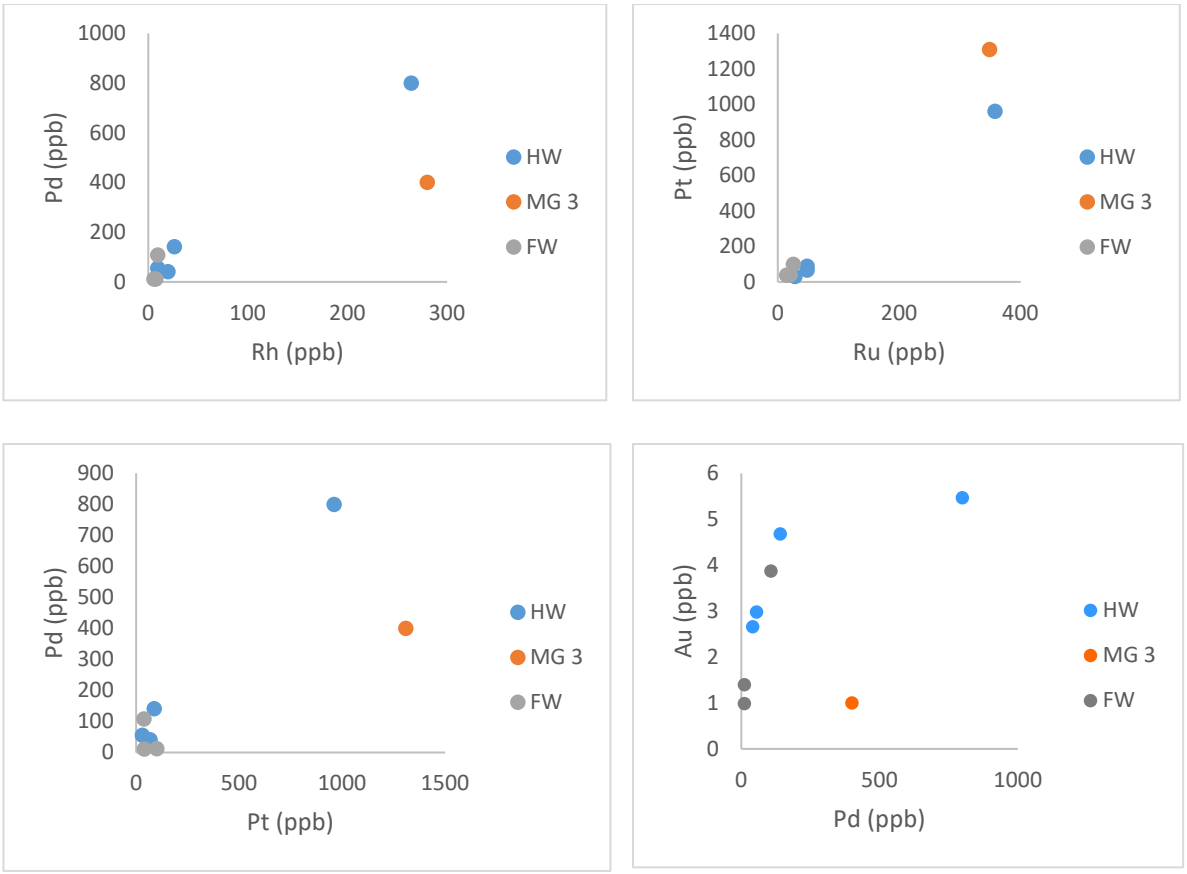

Figure 43. PGE relationships across the MG 3 suite.

A similar pattern is observed along the MG 1 suite of rocks (Figure 44). The chromitites themselves have the highest amounts of Ru and Rh, which corresponds strongly to the higher levels of Pt and Pd. The levels of Au analysed in the rocks are lower than the amounts seen in the MG 3 suite of rocks.

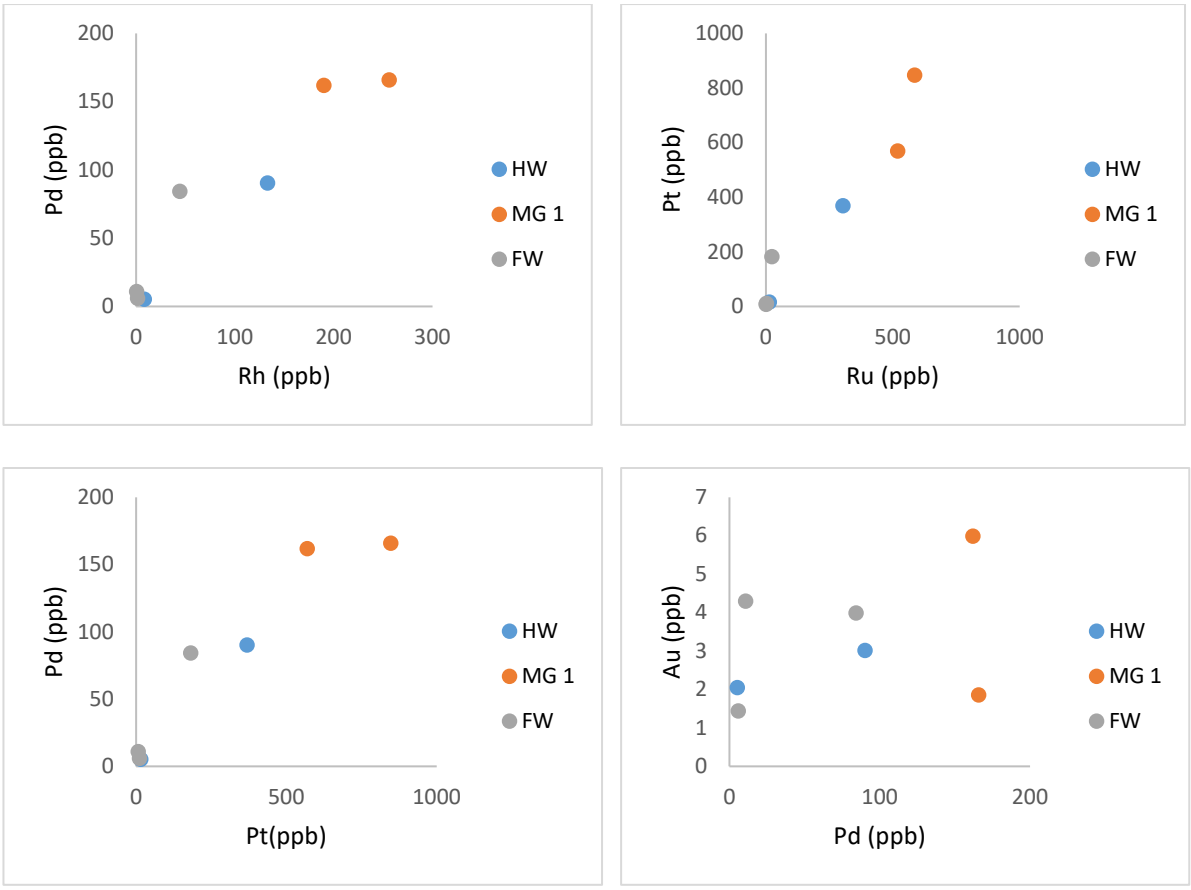

Figure 44. PGE relationships across the MG 1 suite of rocks.

The chromitite showed higher levels of PGE, with the HW showing the second-highest amounts. The FW samples showed the lowest levels bar the Au.

Figure 45 shows the chondrite normalised patterns of the MG 1 and MG 3 chromitite suite of rocks; typical normalised positive patterns are observed from Ir to Ru; this relationship can be observed for the FW, the chromitite and the HW rocks of both the MG 1 and 3 suites. The Rh to Pd portion differs in that the HW and chromitites of the MG 1 are strongly negative whilst the FW is still positive. The HW and chromitite samples for the MG 3 suite show an increase towards Rh then a depletion to Pt, whilst the FW shows a slightly positive pattern to Pt. The normalisation of PGE data to the mantle is thought to be influenced by sulphide segregation which could have been from mantle-derived magmas. Therefore, normalisation from primitive mantle values (Figure 46) is more helpful in determining the derivation of the source and emplacement of the deposit (Barnes and Ripley, 2016).

MG 3 MG 1

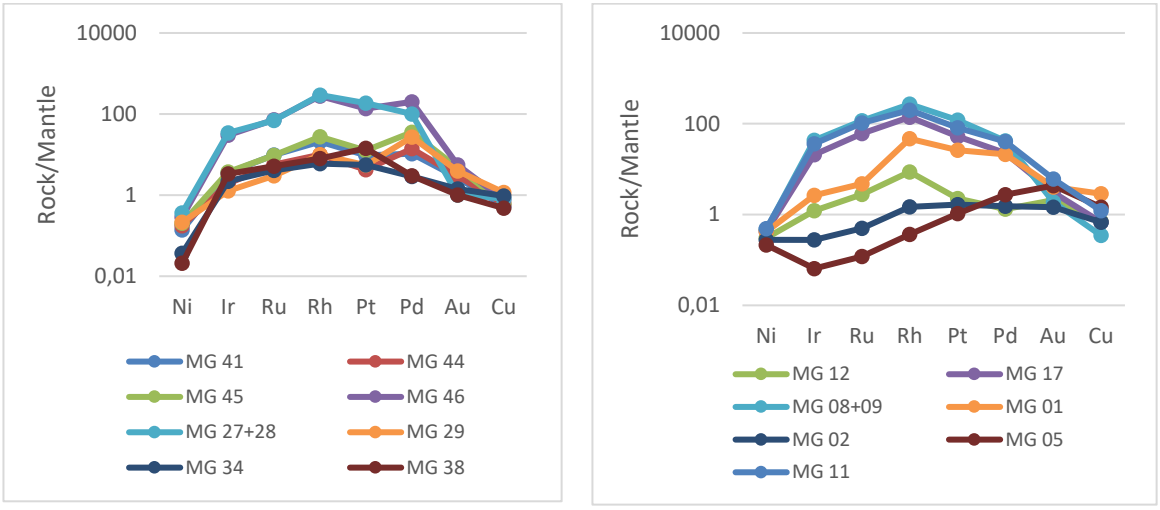

Figure 45. Samples/mantle PGE profiles for the MG 3 and MG 1 layered suites. Samples MG 41-46 represent the HW, MG 27+28 is a chromitite, and MG 29-38 represents the FW. Samples MG 12-17 represent the HW, MG 08+09-11 represents a chromitite, and MG 01-05 represents the FW.

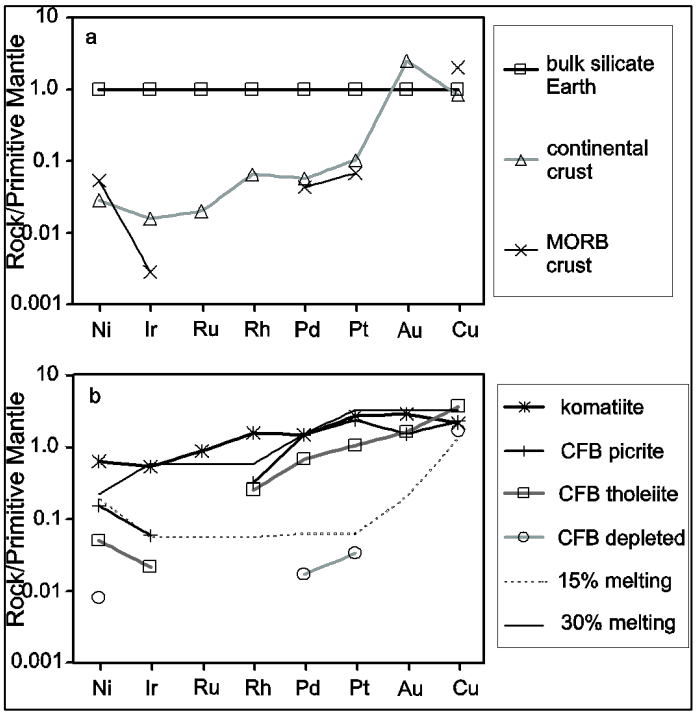

Figure 46. Typical rock/chondrite Ni-Cu values. Adapted from Lodders (2003).

In the MG 1 sequence (Figure 47), the samples adjacent to the chromitite along the FW show decreased Cu, Pd and Au and an increase in Ir, Rh and Ru. Pt and Ni values remained constant as the FW progressed to the chromitite layer. In the chromitite layer, there is an increase in Ir,

Pt, Ru, Pd and Rh with a decrease in the Au and Cu concentrations whilst the Ni remains the same. The immediate HW increases Cu, Au and subtly in Ni, with a decrease observed in the other PGE.

The MG 3 sequence FW increases Au, Pd, Rh, Ni and Cu as the sequence progresses into the chromitite. A reversal trend is observed in the Au and Ru, decreasing while an increase is observed in the remainder of the PGE. A lack of substantial sample material in the chromitite layer itself was why no analysis was present. The immediate HW to the chromitite showed a steady increase in all the PGE. A progressive decrease in Ir, Rh and Ru was observed further into the HW with constant Au, Pd and Ni concentrations.

MG 3 MG 1

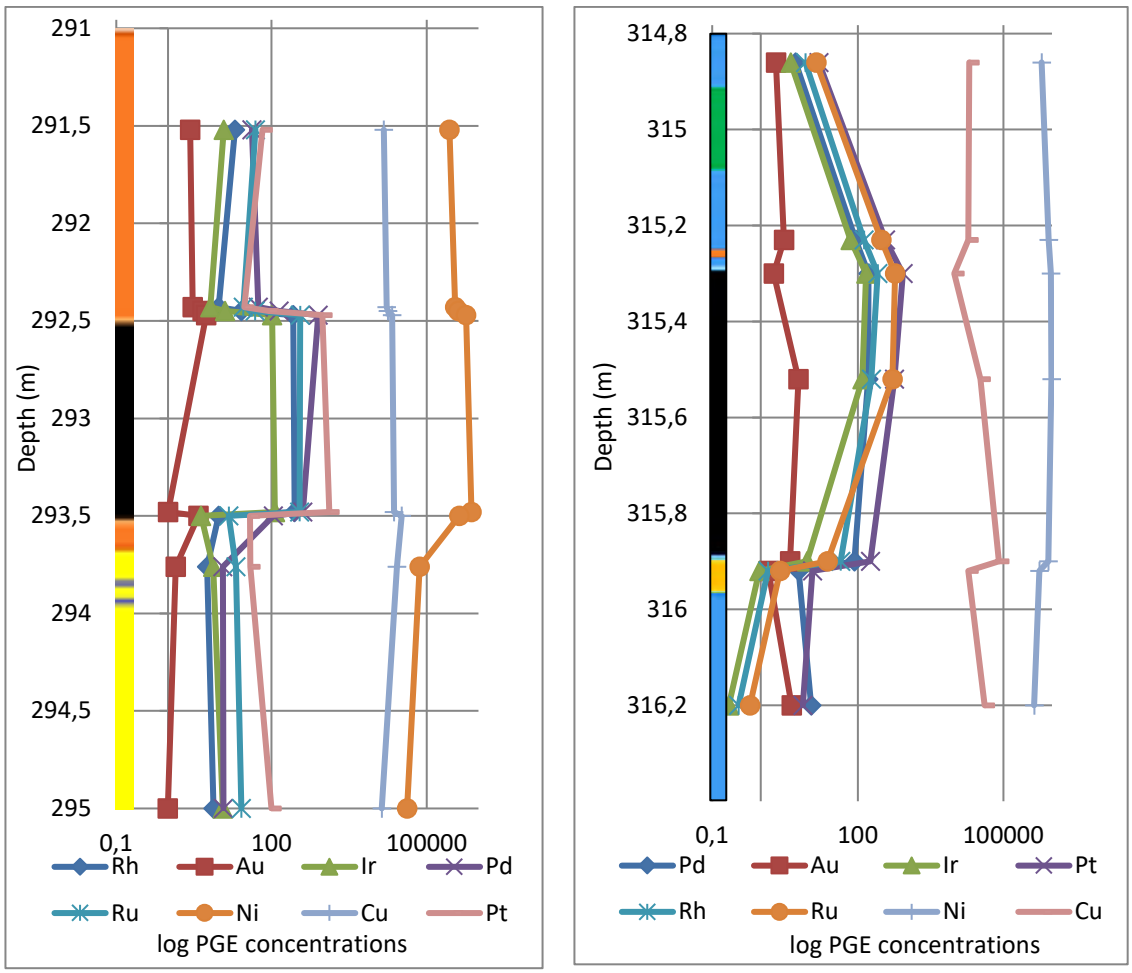

Figure 47. PGE profiles for the MG 3 and MG 1 suite of rocks with the chromitite sequence.

4.6 CIPW Norms

The CIPW norms, as shown in Figures 48 and 49, indicate a higher plagioclase content in both the HW and FW compared to the orthopyroxene of the MG 3 suite. There are increased amounts in the FW with depressed proportions of orthopyroxenes. The HW contrasts the FW with increased orthopyroxene proportions compared to the plagioclase. The CIPW norm index for the MG 1 suite shows orthopyroxene as the most abundant mineral phase in both the HW and FW. The proportions of plagioclase in both the HW and FW remain constant. There are phases of intercumulus olivine in the chromitite suites.

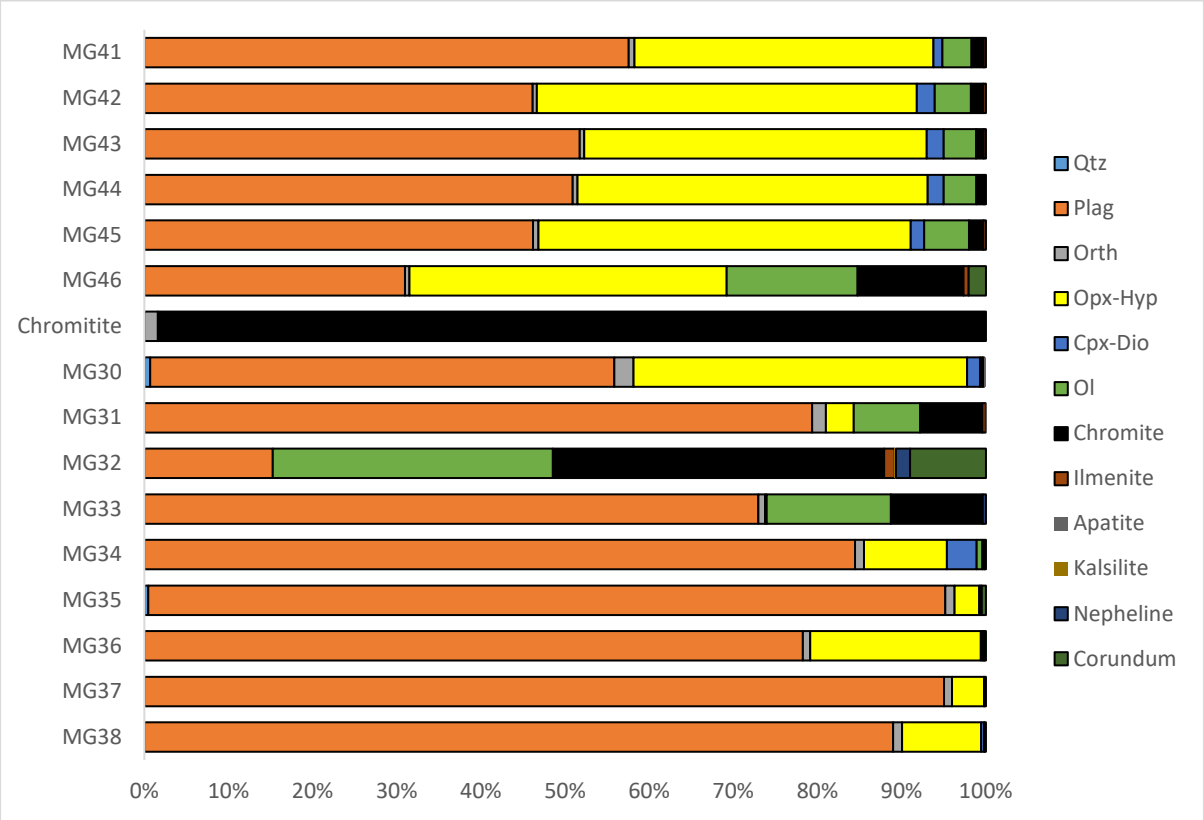

Figure 48. Graph showing the CIPW norms MG 3 chromitite suite.

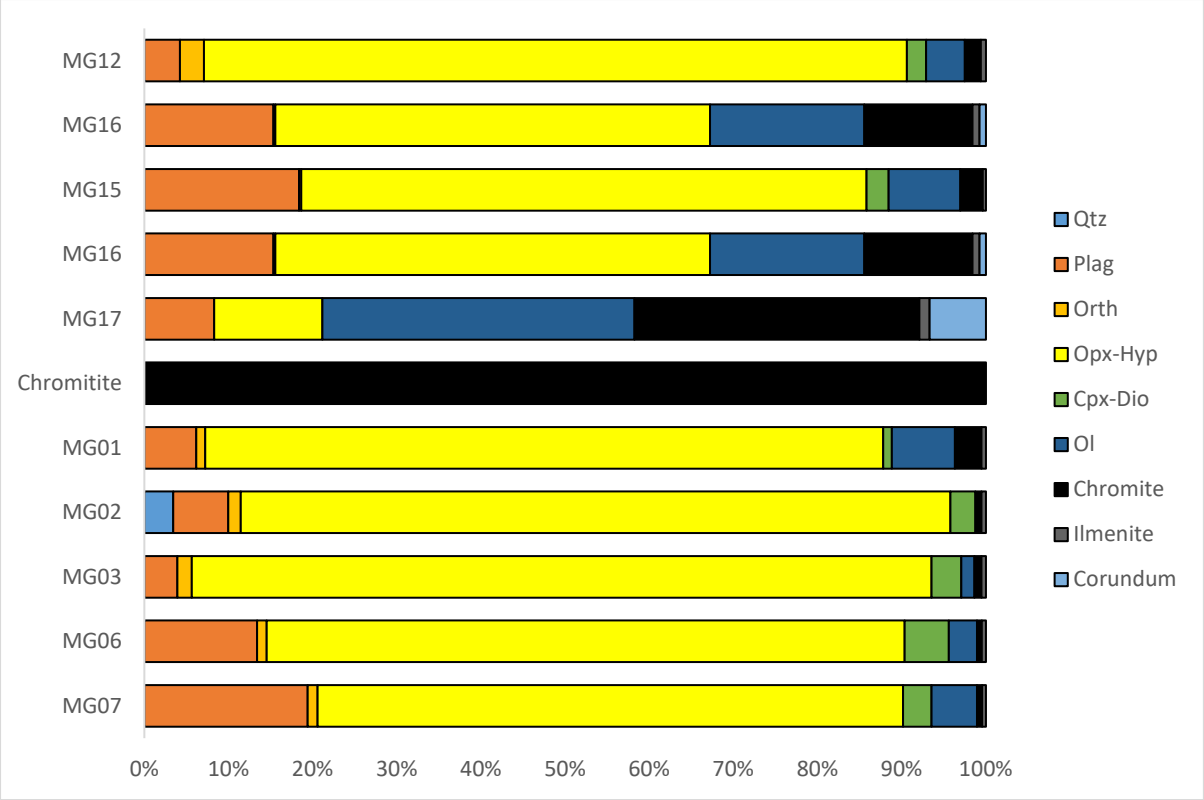

Figure 49. Graph showing the CIPW norm MG 1 chromitite suite.

Chapter 5

Discussion

This chapter will begin with a comparison of the two chromitite layers. The typical models for the formation and emplacement of chromitite layers in layered intrusions were discussed in Chapters 2.1 and 2.3. The characteristics of these models will be evaluated when scrutinising the data attained from the MG 3 and MG 1 sequences. The models used for the association of the PGE with the chromitites seen in Chapter 2.2 will be evaluated to a lesser extent due to the small size of the relevant database acquired.

5.1 Comparing the lithology of the MG 3 and MG 1 chromitites

When comparing the modal abundances of the MG 1 (Figure 19) and MG 3 (Figure 18), chromitites both have pyroxenite-rich hangingwalls (Figure 49), the MG 3 HW has more plagioclase present whilst the MG 1 is more chromite rich along the HW. Both the chromitites have a pyroxenite-rich footwall, although the MG 3 is then underlain by an extensive anorthosite below that. Both have thick chromitites (60-100 cm). This correlates to the whole-rock CIPW norm mineral abundances seen in Figures 48 and 49.

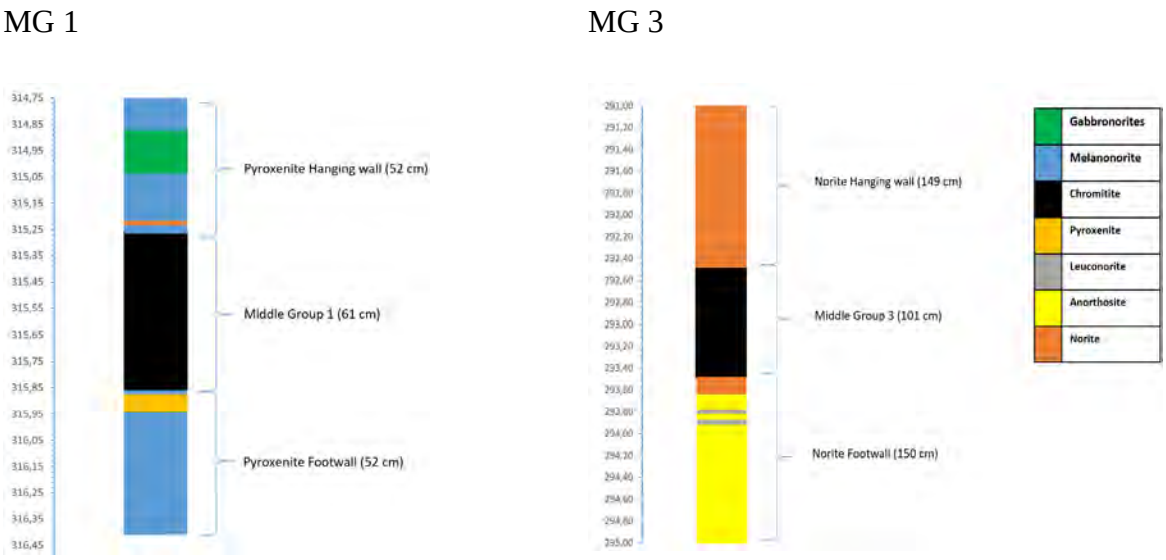

Figure 50: Modal abundance rock classifications of MG 1 and MG 3 rock suites with stratigraphic depth.

5.2 Comparing the primary and secondary rock textures

The plagioclase grains from the MG 1 suite of rocks (Figure 14C) showed deformation twinning. The twinning usually lacks the incredibly straight lamellar of their primarily formed plagioclases and is known to increase the ductile response of rocks (Winter, 2010), and since silicate textures are controlled mainly through compaction and recrystallisation; principal magmatic textures are rarely or no longer preserved (Boorman *et al.*, 2004). This could then indicate secondary mineral grain movement as this is a form of secondary twinning, usually in response to some form of stress.

The formation of oikocrysts depends on the nucleation rate of the different minerals, although the formation can also be explained by replacing olivine primocrysts by the migration of melt through a crystal mush (Kaufmann, 2018). Pyroxene oikocrysts observed in the MG 1 chromitites are seen both in the macroscopic and microscopic textures (Figure 14F). These oikocrysts have been identified in chromite-free zones with aureoles of chromite chadacrysts; this has potentially hindered the annealing process and could be evidence of a late phase formation of chromite rather than early formation (Eales and Costin, 2012).

Samples from both the MG 3 and MG 1 chromitite suite of rocks showed entrained textures and rims (Figure 19); however, they do not follow the characteristics of classical corona textures. Corona textures are closed system reactions that may occur during either retrograde or prograde conditions either by sub-solidus reaction process or prolonged time at elevated temperatures (Claeson, 1998). A potential explanation for these textures would be that during the emplacement of the chromitites, the associated magmatic fluids resulted in the disequilibrium textures observed along with the plagioclase and orthopyroxenes. This type of resorption and embayed mineral grains associated with the growth of ferromagnesian silicates has been explained as a product of a hot slurry emplacement (Eales and Costin 2012) or of hydromagmatic fluid migration (Boudreau, 2008). These textures can be explained by opx - plag = cpx + liquid, followed by the opx being resorbed by a reaction with an evolved liquid (now represented by plag). The new cpx had then nucleated onto the dissolving opx. This sub-solidus migration of exsolved cpx from the opx host, facilitated by prolonged high T cooling (reheating) stage, resulted in the efficient extraction of structurally incompatible cpx to the grain boundaries. The crystallisation of first liquids, then the influx of hot magma and crystals, reheats existing crystals (induces reverse zoning of plagioclase) and the migration of trapped exsolution lamellae in opx (Figure 14). In Figure 17 D, there is further evidence for the

secondary origin of olivine relative to plagioclase, with a partially embayed grain of plagioclase surrounded by olivine.

The textures observed in the MG 1 and MG 3 chromitites show exsolution lamellae within the chromites, but this was not standard (Figure 16A). The chromite grains show triple junctions at 120° and straight grain borders, potentially due to a crystal annealing event via Ostwald ripening (Winter, 2010). However, some pentagonal contact chromites do not follow a natural symmetry (Strickland *et al.*, 2020). Increasing evidence suggests that cumulus texture evolves by crystal ageing and compaction processes. These processes modify the textures observed in the pyroxenes and the plagioclase in the rocks and is a feature for further evidence of recrystallisation.

Cumulates are a series of igneous rocks formed by the accumulation of crystals. Orthocumulate rocks consist of cumulus minerals and the crystallisation of intercumulus liquid, the composition of which would be the new magmas. Adcumulus growth reduces the intercumulus liquid by pushing it out. Adcumulus growth eliminates the intercumulus minerals—an absence of zoning in an adcumulate rock (Wager *et al.*, 1960). The changing proportions of cumulate crystals and evolved interstitial residual liquids can explain geochemical trends or anomalies. The cumulate textures can be separated into (Wager, 1963):

- Adcumulates: no trapped liquids: geochemistry of rock should pretty much look like the main mineral (in this case, basically one mineral),
- Orthocumulates: lots of trapped liquid, crystallising in place and communicating with residual parent liquids above the current level of crystals and
- Heteradcumulates: which is seen as a representation of both textures.

Rocks that are products of in-situ magma crystallization would show no effect of cumulate-trapped liquid ratio variation and therefore would have no cumulates, and cotectic proportions of the major minerals (opx & plag) would be observed. In Figure 51, there is evidence for a) cumulate textures and b) non-cotectic mineral proportions in both the hangingwall and footwall rocks of both chromitite suites. The HW and FW of the MG 1 appear to have more adcumulate texture, whereas the MG 3 appears more heteradcumulate, as seen by the interstitial plagioclase. The more adcumulate nature of the MG 1 suite could potentially be explained by the driving out of interstitial liquids by compression of the late crystallising magma; this would have also led to the plastic deformation observed in its plagioclase as well.

	MG 1	MG 3
FW	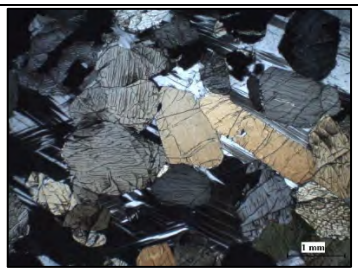 MG07C	 MG 38C
FW	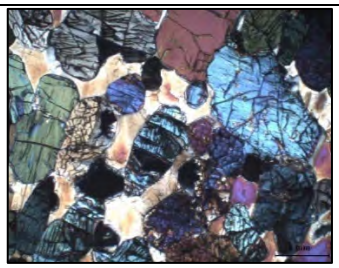 MG05	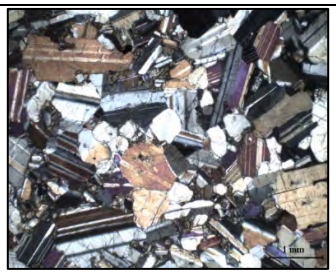 MG34B
HW	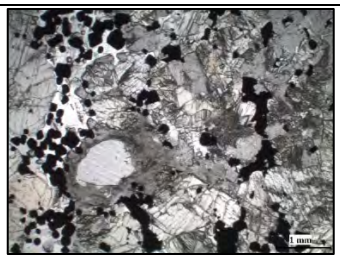 MG 16B	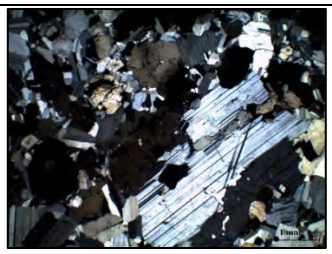 MG 41C
HW	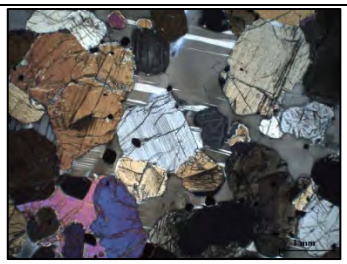 MG 14	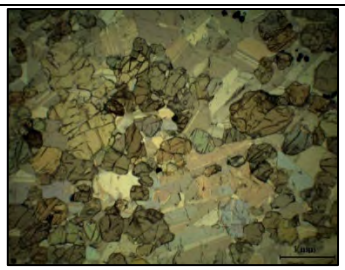 MG 44A

Figure 51: Cumulate textures observed along with the MG suite of rocks in correlation to the position along the hangingwall or footwall of the chromitites. Picture IDs are included to correlate with stratigraphic positions. MG 44A was taken in PPL, whilst the rest of the photomicrographs were taken in XPL.

5.3 Comparing the mineral composition and whole-rock trends

In Figures 30 & 31, both the MG 1 and MG 3 sequences have trends of opx becoming more magnesian up through the footwall, then continuing this trend through the chromitite, but in the upper half to third to the top of the chromitite, it reverts to a more evolved composition, before continuing upwards becoming slightly more primitive again. The feldspars in MG 1 are most primitive (An_{85}) in the upper part of the chromitite, compared to both the HW and FW, which are labradoritic. In MG 3, the plagioclase is consistent, around An_{75}, with possible typical fractionation trends (increasingly sodic with decreasing depth) over the scale of tens of centimetres. The more variation in the A_n composition of the plagioclase, the natural expectation for the formation would be fractional crystallisation. The minor variation observed in the A_n content may imply the emplacement of the plagioclase in the rock. These trends were noted in the Skaergaard intrusion (McBirney, 1989) with the An# of plagioclase and the Mg# of olivine and Ca-rich pyroxene. These variations in the composition suggest crystal growth in-situ with conditions affected by external factors such as rate of nucleation, cooling, and phase relations (McBirney & Noyes, 1979). The Mg # (Figure 52) of the chromites shows the MG 1 FW with the lowest values, with the HW having values ranging from 23-49. This HW samples of the MG 3 range from 18-31, and the FW and chromitite values range from 26-38 and 38-44, respectively.

Cawthorn and Spies (2003) noted in the upper Critical Zone containing the Bastard, and Merensky reef contains an excess of plagioclase relative to orthopyroxene cotectic proportions. Cotectic proportions should contain 60-65 % plagioclase, but 74 % and 84 % are seen in the Merensky and Bastard reef. Figure 36 shows the plagioclase/pyroxene ratio for the MG 1 and MG 3 rocks; the proportions range from 5-80 %. Adding a more magnesian-rich magma to create the cyclic units does not make the amount of plagioclase observed. The low proportions indicate that a new cycle was initiated before the previous one was complete due to either erosion or non-settling. The proportions of plagioclase in the Merensky and Bastard are higher than cotectic proportions. The range is 54-84 %, with only one value decreasing below 54% (Cawthorn and Spies, 2003). There is a suggestion of excess plagioclase in the system.

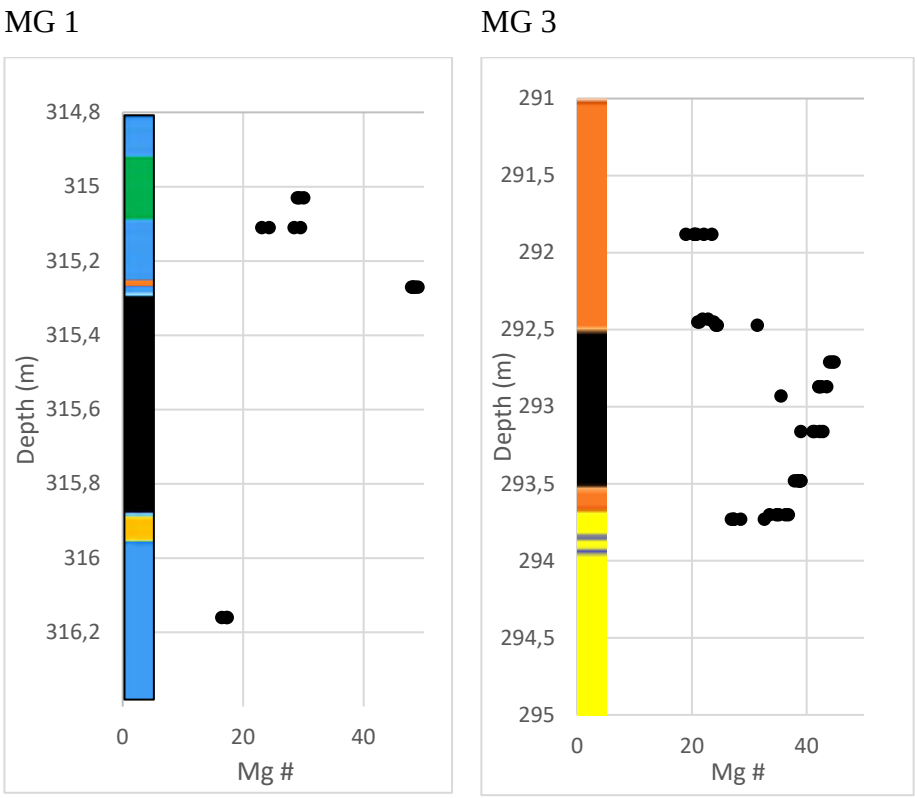

Figure 52: Mg# for the chromites in the MG 1 and MG 3 sequence.

The Cr/Al atomic ratios within the orthopyroxenes of the sequence can serve as an indicator to show restrained variations in rocks that may appear geochemically homogenous (Eales *et al.*, 1986). When looking at Figure 53, an increase in the ratios is observed through the FW of the MG 1 with a sharp decrease at the chromitite base, there is then an increase again through the chromitite with a decrease and then an increase in the HW. The MG 3, on the other hand, shows a decrease in ratios then a minimal increase as the chromitite is approached, there is an overall increase in the ratios through the chromitite with constant HW ratios. The observed reversals in the Cr/Al ratios could potentially indicate either a Cr depleted or enriched (MG 3 FW) pulse or an indicator of ephemeral changes within the chamber or source (Eales and Marsh, 1983).

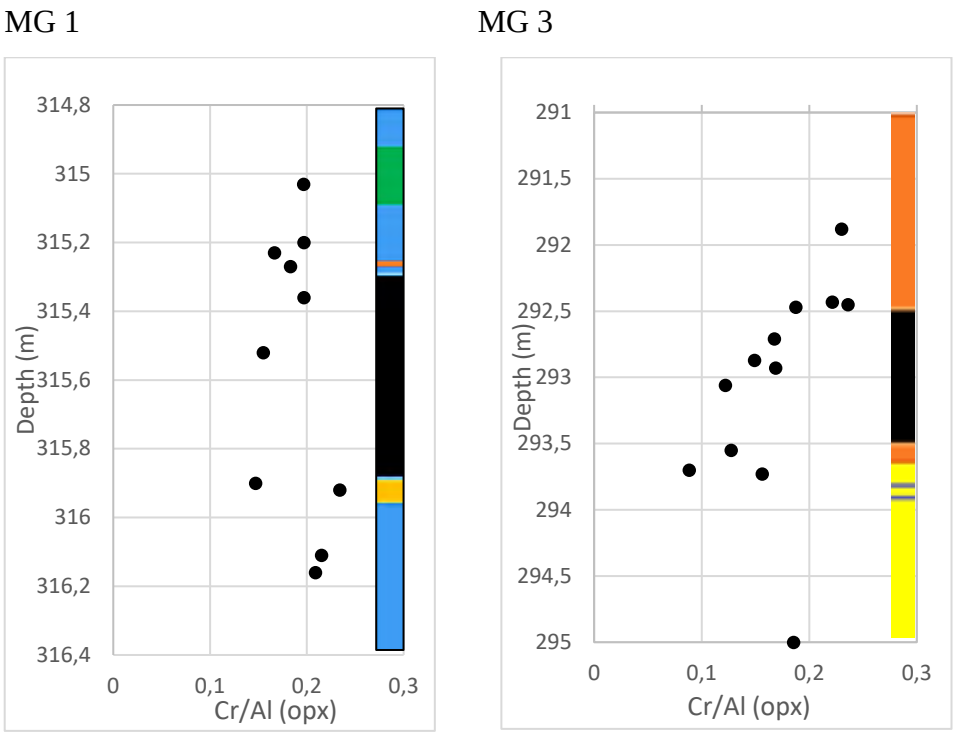

Figure 53. Cr/Al ratios of orthopyroxenes in the MG 1 and MG 3 sequence. Average values from the samples taken.

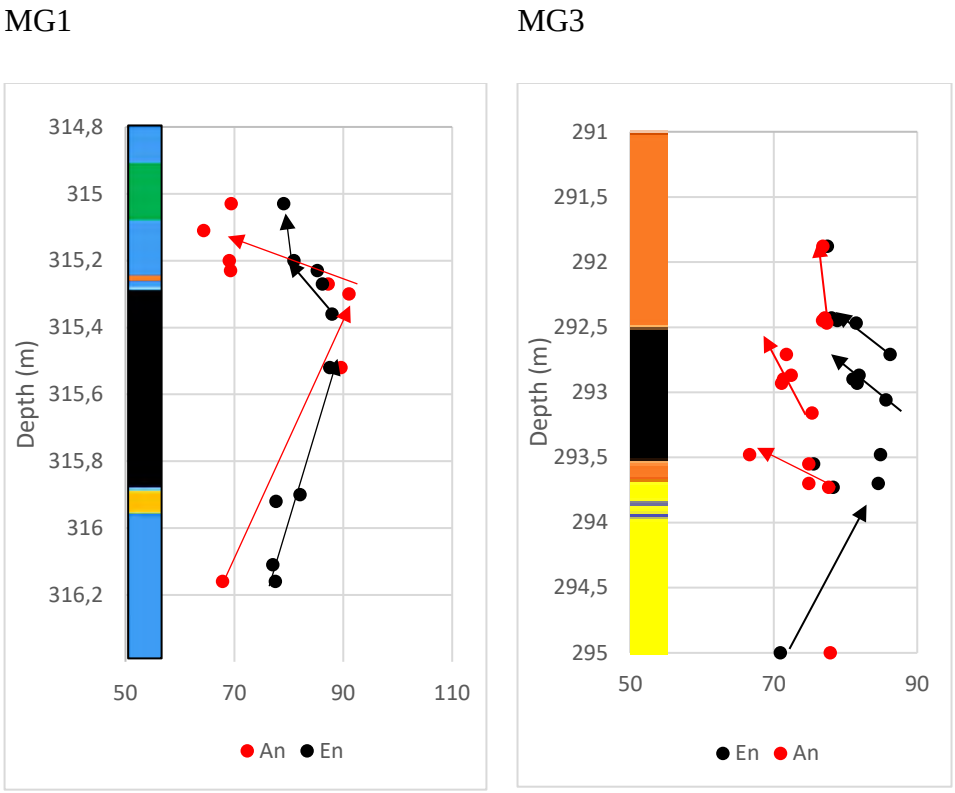

Figure 54: An and En values for the MG 1 and MG 3 rock suites corresponding to stratigraphic depths.

MG 1 MG 3

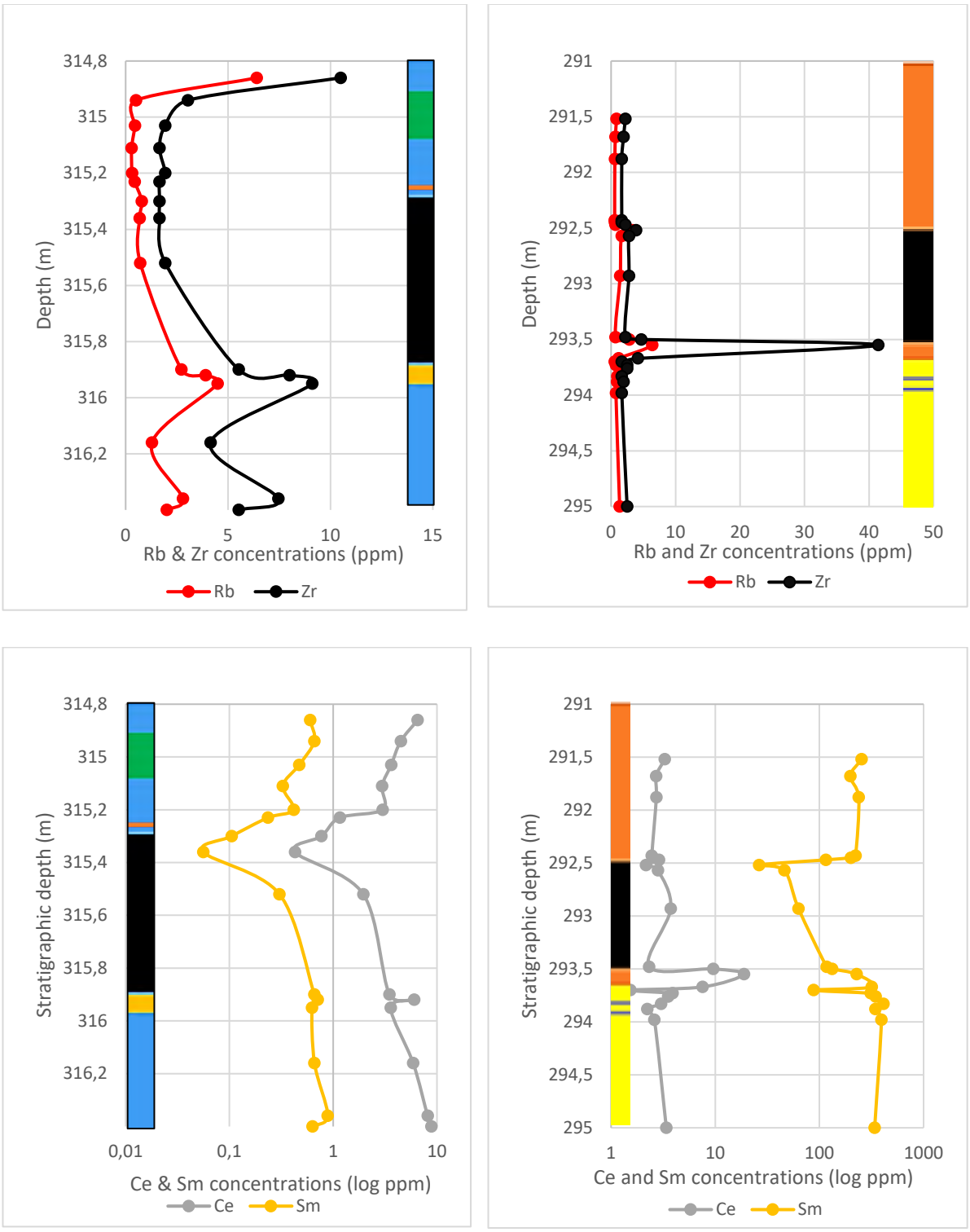

Figure 55: Rb vs Zr and Ce vs Sm concentrations of the MG 1 and MG 3 suites corresponding to stratigraphic depths.

The study of REE patterns within cumulates such as the suite of MG 1 and MG 3 rocks can be complex when it comes to the interpretation of such patterns due to either secondary mineral migration or the number of cumulates that govern the concentration of the REE (Maier and Barnes, 1998). However, it is short-sighted to ignore the trends when comparing the suite of silicates from the same stratigraphic section/core. Figure 26 shows enrichment and depletion trends that correlate with the presence of cumulus amounts of plagioclase in the HW and FW of the MG 3 chromitite; the MG 1 chromitite REE patterns are controlled by the presence of high amounts of opx in the silicates as well as more abundant ilmenite content within the chromitite itself.

A pattern of reverse cryptic variation is observed from the above plots (Figures 54 & 55). The trends for Rb (LILE) and Zr (HFSE) show that the highest abundances of these elements are in the FW, the lowest in the HW, and varying trends in the chromitite. This is, therefore, inconsistent with a standard, vertically fractionating sequence of parent rocks, in which the incompatible elements should become progressively enriched. There are no obvious contrasts between mineral compositions in HW and FW, suggesting that the parent magmas from which they crystallised were similar. The silicates found in the chromitite layer are, if anything, more primitive than those in HW and FW. The incompatible element abundances in the chromitite are also, if anything, lower than their HW and FW and certainly not higher. A crustal contamination model produces the exact opposite effect.

The trends and observations from both the MG 1 and MG 3 chromitites above can give an indication of the origin of the chromitite layers and their relationship with the PGE. The next subsection will strive to connect the above observations to the prevailing models.

5.4 Origin of chromitite layers

5.4.1 Crustal contamination

Irvine had proposed this in 1975. The crustal contamination of an orthopyroxenite would create chromite oversaturation based on Irvine's model. It works for rocks crystallising olivine because the cotectic between olivine and chromite is believed to be a curve (Figure 56). The enstatite-chromite cotectic is a straight line, effectively parallel to the crustal contamination trend line, so it is not easy to pull an orthopyroxenite into the chromite field by adding a silicate. Contamination drags the magma composition off the olivine-chromite cotectic line into the chromite-only (yellow) field. If the magma is already up at point F or higher, contamination with SiO_2 (top apex of triangle) + minor MgO (which is represented in the Fo corner at lower

left; a granite or sediment, for example) will not pull you to the right much, if at all. Alkali elements (enriched in crustal rocks compared to mantle-derived rocks) are lower in the MG1 chromitite than in its HW and FW. Therefore, contamination would not explain its formation.

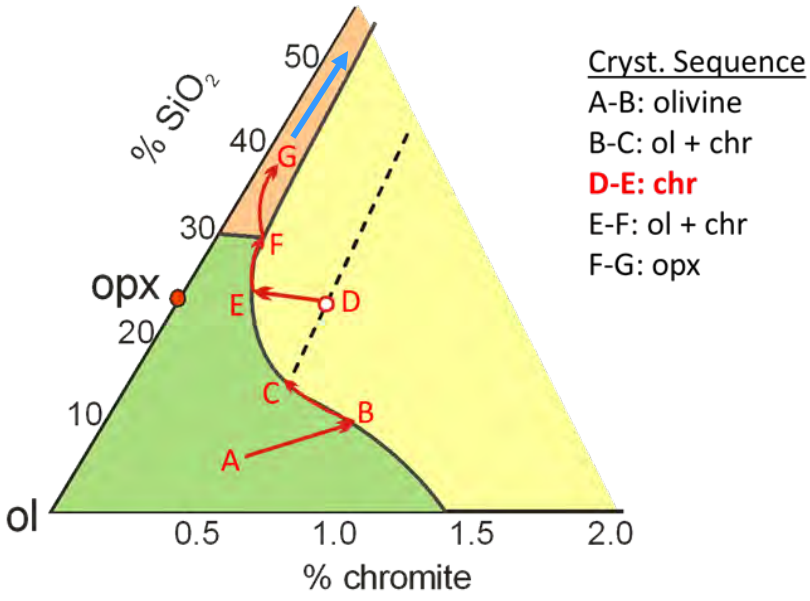

Figure 56. Phase diagram illustrating contamination of olivine-rich magma (at C), and for comparison, of orthopyroxenite, from G (after Prevec, 2021).

5.4.2 Magma mixing

Irvine proposed the magma mixing model in 1977. This mechanism requires a curved cotectic path between the compositions of the mixing magmas in Fo-chromite-SiO_2 space, which does not readily apply to pyroxenites, where contamination would not easily draw the magma composition into the chromite stability field (Figure 56). There is no evidence for sharply contrasting magma compositions in the HW and FW of the MG 1 and MG 3 sequences that would support the formation of chromite in-situ at the mixing interface. Figure 57 shows Cr concentrations across the chromitites; the HW shows higher concentrations than the FW, consistent with magma mixing origin with differential Cr contents.

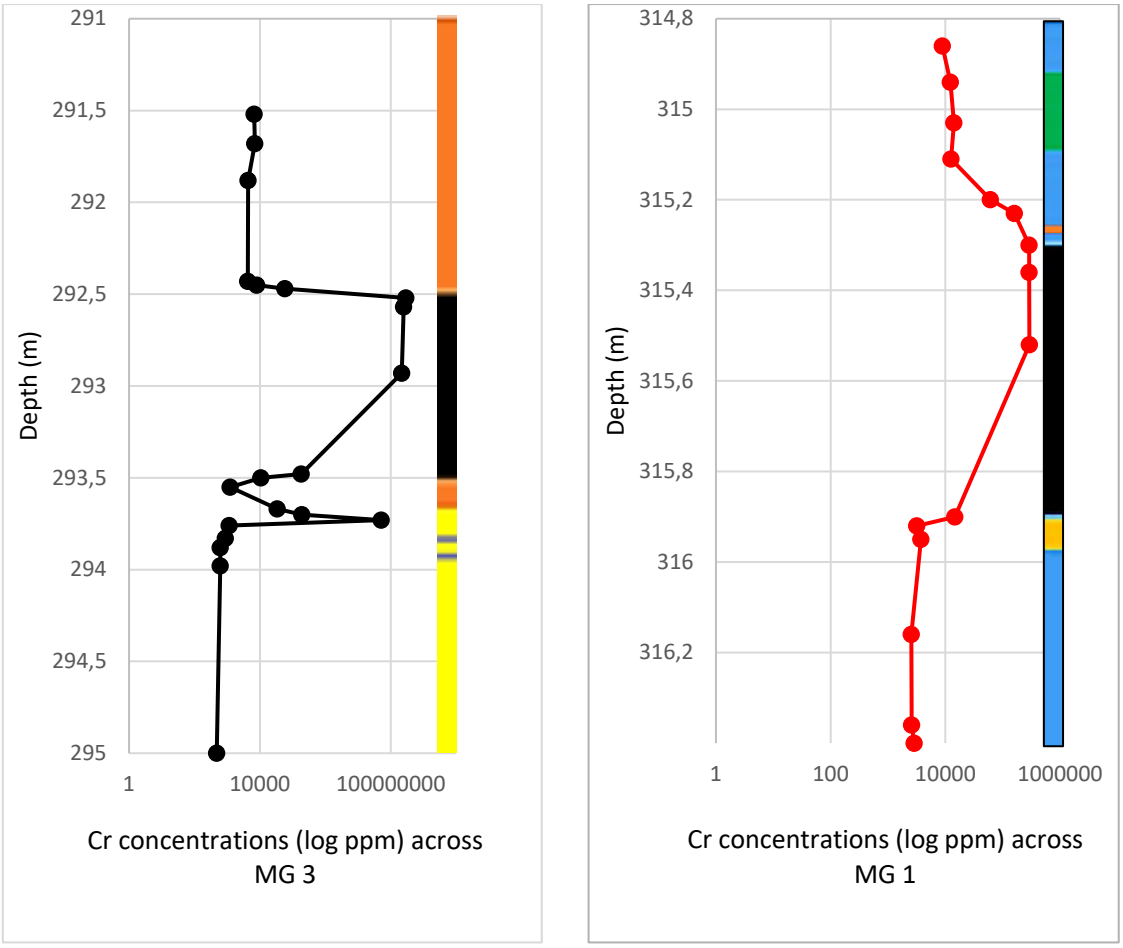

Figure 57. Cr concentrations across the MG suite of rocks with stratigraphic depth.

However, it is also consistent with the pattern of increasingly primitive rock compositions upwards, as also seen in terms of Ni content (Figure 45), which should be unaffected by chromite directly, and is controlled by opx ($D_{Ni}^{opx} > 1 >> D_{Ni}^{plag}$) and sulphides, which are believed to be effectively restricted to the chromitite layers in this part of the stratigraphy (Kottke-Levin, 2011). Whether this represents an upwards trend of increasing Ni content or a Ni-rich primitive HW overlying a Ni-poorer FW cannot easily be determined, as the higher Ni contents may also correspond to higher px contents in the HW (Figure 58) in MG 3; however, in MG 1 the HW is not more pyroxenitic than the FW, so this cannot explain the Ni-rich HW. This suggests some sort of reverse differentiation, where a more evolved magma is being overlain by more primitive magma. The increase in the Ni trend was observed in Figure 59, whereby the sample was taken from the silicate rock in the MG 1 FW.

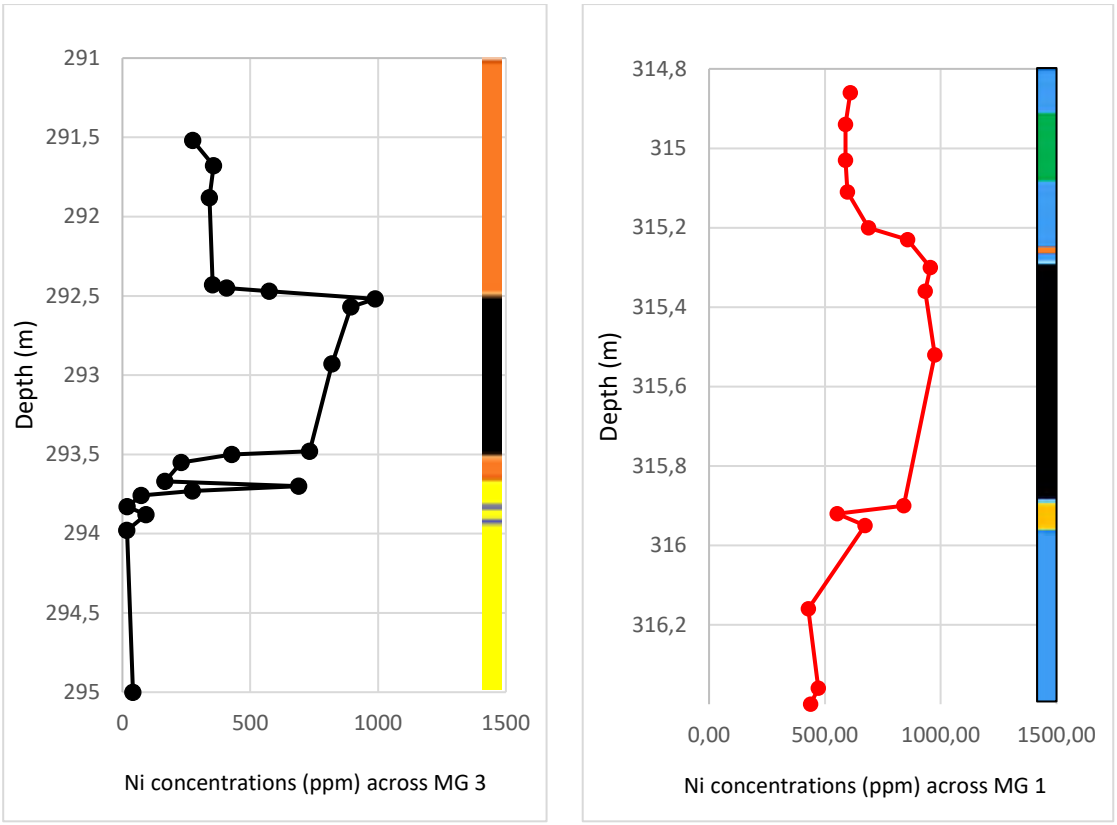

Figure 58. Ni concentrations across the MG suite of rocks related to stratigraphic depth.

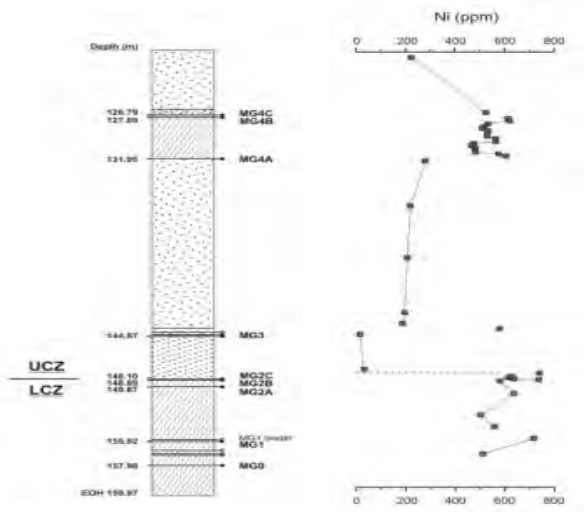

Figure 59. Whole-rock Ni concentrations of the silicates across the MG sequence. (Kottke-Levin, 2011)

5.4.3 Sudden temporary changes in magma conditions.

Authors such as Murck & Campbell (1986) and Lipin (1993) had proposed temporarily changing the conditions of the magma. This model would involve a normally differentiating, fractionally crystallising magma, during which sudden changes in the crystallization conditions temporarily stabilise spinel (chromite) until either the chromite is exhausted or until the conditions revert to those in which chromite stability is no longer facilitated. The appearance of plagioclase cumulates during this sequence would therefore be purely a coincidence petrologically. Arguably the presence of a lithologically distinct layer (anorthosite) could provide a horizon of rheological contrast and different solidification rates compared to the pyroxenitic rocks, which might have facilitated the emplacement of a new magma pulse as its immediate footwall. It has been established that we do not have a typical differentiation sequence across these layers in this section. Multiple pulses of magma would seem to be required to explain the reverse differentiation profiles reflected by the mineral chemistry and trace element trends. This does not mean that those magmas could not have been intruded, regardless of their sequence or source, under conditions in which chromite stability was enhanced.

5.4.4 Changing the oxidation state of igneous melts by contamination.

Many authors, such as Mungall *et al.* (2016), Maier *et al.* (2012) and Scoon & Teigler (1994), to name a few, have suggested the formation of the chromitites by contamination. This contamination could have occurred via the carbonates that are available in the footwall (Pretoria Group of Transvaal Supergroup). There is no evidence of its involvement in this study, but it doesn't rule it out; carbonates do not carry a vast budget of Sr or Nd to affect radiogenic isotopes necessarily, so effects might not be noticeable. This has been proposed to cause spinel stabilization elsewhere for magnetite (Ganino *et al*., 2008) and chromite (Dyan, 2021), although it was based on a reasonably clear and direct link in those cases. There is no evidence for higher Ca in the chromitites (Figures 21 & 22) nor higher concentrations of water-soluble alkali metals, so while these possibilities cannot be excluded, there is not much evidence to support them. The other way to change the oxidation state of the magma would be to increase the water concentration. There was minor biotite (Figures 18 & 19) identified in the upper levels of both chromitites along with altered plagioclase and opx (Figure 15). The higher water content will also preferentially stabilise olivine and clinopyroxene, and spinel over orthopyroxene and plagioclase (Boudreau, 2008). Olivine was observed in both the HW and FW sequences of both chromitites (Figures 48 & 49), with the significant grains being

serpentinised. This evidence could support higher water contents. Wallmach *et al.* (1995) have shown that in the critical zone, preserved periclase in xenoliths supports an absence of H_2O-rich fluids. Evidence from the REE trends in this suite suggests that although hydrothermal brines can extract REE from the melts with higher efficacy, LREE tends to be extracted more efficiently (Manning and Aranovich, 2014); the REE distributions, however, seem to be mineralogically controlled in both the MG 1 and MG 3.

5.4.5 Emplacement of a Cr-enriched sill into an existing pyroxenitic to a noritic sequence.

The chromitites could represent the basal layers of intrusive sills emplaced into a pre-existing sequence of pyroxenitic to noritic rocks (Scoon & Teigler, 1994; Mungall *et al*., 2016), within which the chromite has accumulated by efficient density settling. Maier *et al*. (2012) suggested a hydrodynamic process to facilitate this process. Latypov *et al.* (2018) proposed that chromite precipitated during decompression of the host magma en-route from depth (specifically the mantle in this model) and then settled out after emplacement as an explanation for pyroxenite-hosted massive chromitites (with associated PGE sulphides) lower in the stratigraphy (LG 6). Based on the existing evidence, this emplacement mechanism is the least objectionable of the options presented here due to the lack of cryptic variation observed in the Cr# and Mg# of chromite apart from the MG 1 chromitite HW and FW reverse cryptic signature, which is potentially indicative of possible emplacement rather than in-situ fractional crystallisation.

5.5 Potential PGE control and distribution within the MG 3 and MG 1 chromitites

In Figure 45, the contrasting PGE chondrite concentrations can serve as a petrogenetic tracer, showing a flat primitive pattern or a positive fractionated plot (von Gruenewaldt and Merkle, 1995). The same authors have suggested that the PGM within the chromitites formed from its parental magma. The relatively positive patterns of the FW in both the MG 1 and 3 could potentially shine a light on a similarly evolved rock as with the HW and chromitites of both sequences showing a relatively flat and more primitive pattern. The rock type evolution would then support an emplacement of deeper primitive chromitites, which would cut through the fractionated rock, creating a FW. Then, settling allowed for a more primitive chromitite and HW. Robust control by magmatic sulphides should give a Merensky & UG2-like PGE profile, enriched in PPGE and depleted in IPGE (Junge *et al.*, 2016). The MG chromitites in this study match those from literature (Scoon & Teigler, 1994 and Junge *et al.*, 2016), as seen in Figure 60, with relatively flat normalized profiles enriched in Ru and Rh relative to Ir and Pt and Pd. This is thought to reflect PGE scavenging in a low-sulphide liquid environment, where the spinels become the primary scavenger, with some associated sulphides. The number of visible

base metals in both layers is uncommon. Sulphides in the MG 1 and 3 chromitite sequence were mainly observed as inclusions and interstitial phases at the boundary of grains; this observation correlates to those of Lee & Fesq (1986) in the MG chromitites from the western Bushveld.

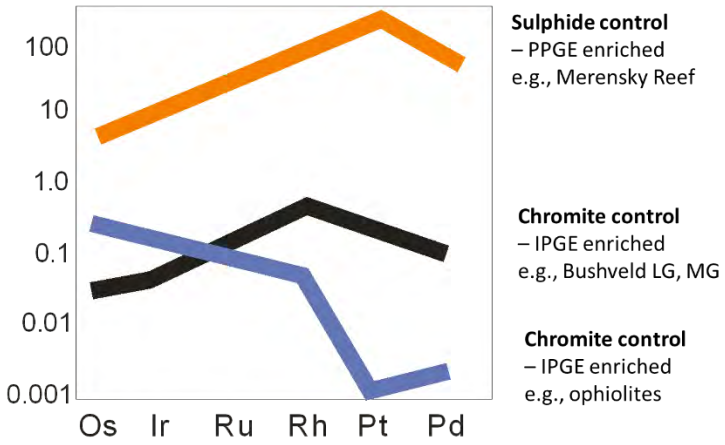

Figure 60. Representative plot showing the distribution of PGE and the control mechanism. Data derived from Tredoux et al. (1995) & Junge et al. (2016) in Prevec (2021).

The Cu/Pd ratios serve as an indicator of sulphide saturation history and are used as a possible indicator for mineralisation (Maier *et al.*, 1996). The Cu/Pd ratios for the MG 1 varies with a decrease in the ratios with decreasing height as it approaches contact with the chromitite. There is then an increase with stratigraphy in the HW of MG 1, matching the values in the FW. The Cu/Pd ratios of the MG 3 rock suite are typically lower than the MG 1 suite of rocks. The HW ratios of the MG 3 are lower than the FW; there is a decrease in ratios as the HW approaches the chromitite with an increase. The typical Cu/Pd MORB values are plotted to serve as a baseline for indicating the point of sulphide saturation. Neither the MG 1 nor MG 3 (Figure 61) profile shows evidence for scavenging PGE by sulphides from above (settling) or below (hydromagmatic liquid or silicate magma upwelling by compaction). The scavenged zones are expected to show high & erratic Cu/Pd ratios, which are entirely missing here. It is, therefore, safe to assume that the concept of the PGE being introduced with the chromite is feasible.

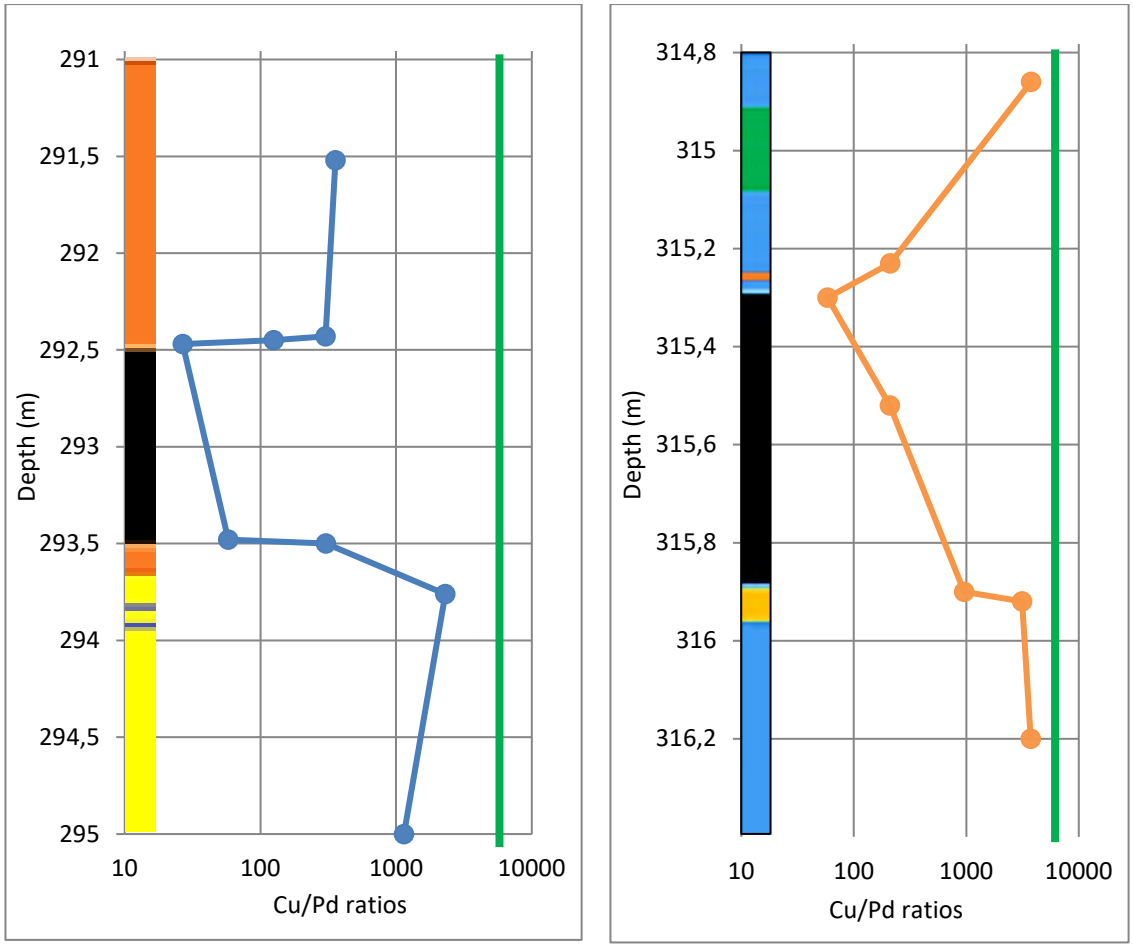

Figure 61. Cu/Pd ratios vs stratigraphic depths for the MG 3 and MG 1 rock suite. A typical MORB value is plotted as a green line.

Figure 47 shows the PGE-Au concentration profiles along the stratigraphy of both the chromitites; there was no obvious FW PGE-depletion trend observed that would aid in the development of a fluid mobilised PGE-reconcentration model as suggested by Prevec *et al.* (2021) for the Merensky Reef.

5.6 Potential formation of the MG 3 & MG 1 chromitites.

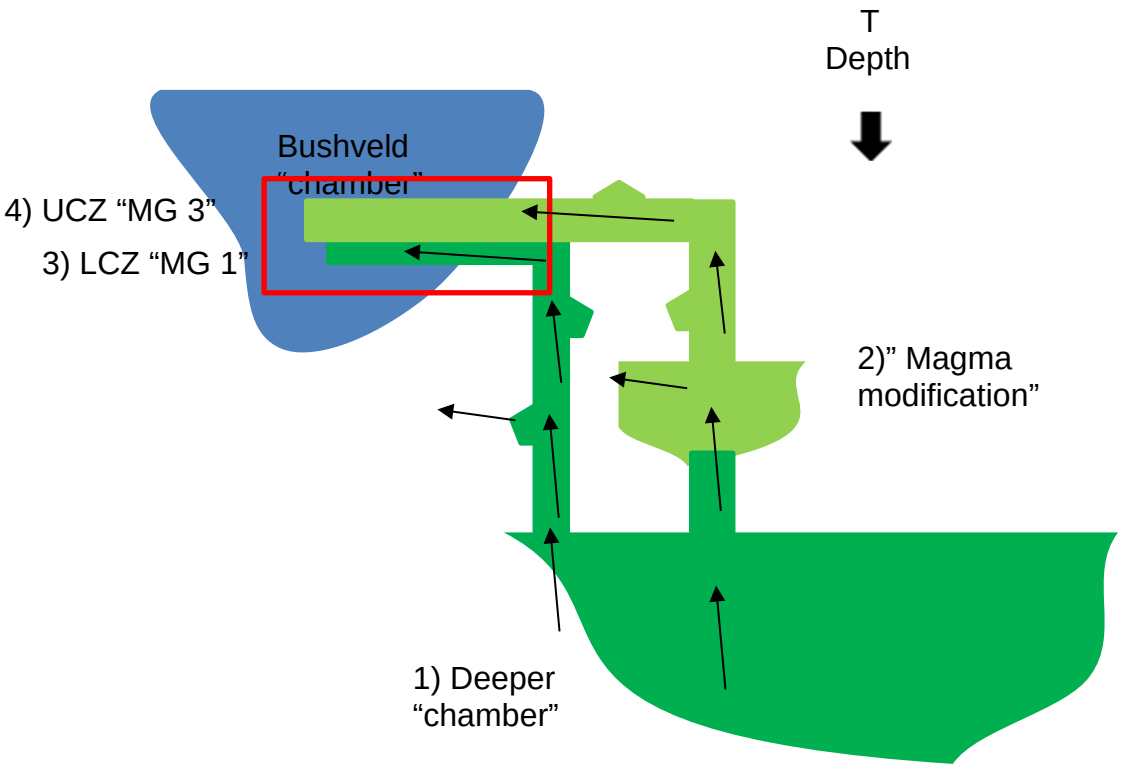

Figure 62. Proposed schematic cross-section for the origin and emplacement of the MG 1 and MG 3 chromitites.

Figure 62 depicts the following stages: stage 1 Magma staging chamber at depth; the origin of the magmas that comprise the MG 1 and 3 chromitites was not the focus of this study. stage 2: shows the transportation of the magma and how it digresses through different pathways from the main magma chamber; along the pathways, there are various degrees of changes to the chromitite layers and silicates; stage 3 is the emplacement of the MG 1 chromitite suite and Stage 4 is the emplacement of the MG 3 chromitite suite. Figures 63-65 will focus on the magma dynamics in stages 3 & 4 of the process.

5.7 Potential emplacement model of the MG 3 & MG 1 chromitite layers

Latypov *et al.* (2018) have provided evidence through phase equilibria and modelling that account for chromitite-only saturation along the ascension path to the Bushveld final chamber, as theorised in Figure 62. The cooling of the magma, along with the decrease in pressure and changes to the oxidation state of the environment, allowed the chromitite slurry to form. The characteristics of the magma would be comparative to that of slag or molten metal in the

smelting process. The effect of suspended crystals in a melt increases its apparent viscosity; slag must possess a low enough viscosity to allow easy separation from the metal phase and increase mass transfer rates across phase interfaces. The physical properties of the magma would have allowed it to assimilate the surrounding conduits and provide a transport mechanism for the already formed crystals like molten slag. By looking at the pyroxenes' Mg/Fe ratio and Al/Cr, a decrease in temperature and oxygen fugacity is thought to account for such ratios. The Al/Cr ratio in spinels decreased with increasing silica activity in melts; melts higher in SiO_2 would precipitate spinels richer in Cr. From the results obtained in the study, one of the following factors applied to increase the solubility of chromium oxide in slags is an increase in operating temperature, a decrease in the feeder material's chromium oxide content, a decrease in slag basicity and a decrease in oxygen partial pressure (Bartie, 2004). The subsequent influx of the slurry travelled along the partially congealed interface of the pre-existing more primitive and the newer evolved slurry. The process would have occurred with multiple “sill-like” pulses with varying mineral chemistry and static components. Caricchi *et al.* (2007) have noted that with an increase in temperature, there is a decrease in the viscosity, and an increase in the crystal fractionation of the melt would increase the viscosity. The deformation and preferred orientation in some plagioclase grains indicate a potential non-Newtonian melt movement characteristic, thus entrenching a crystal-laden melt emplacement (Figure 63).

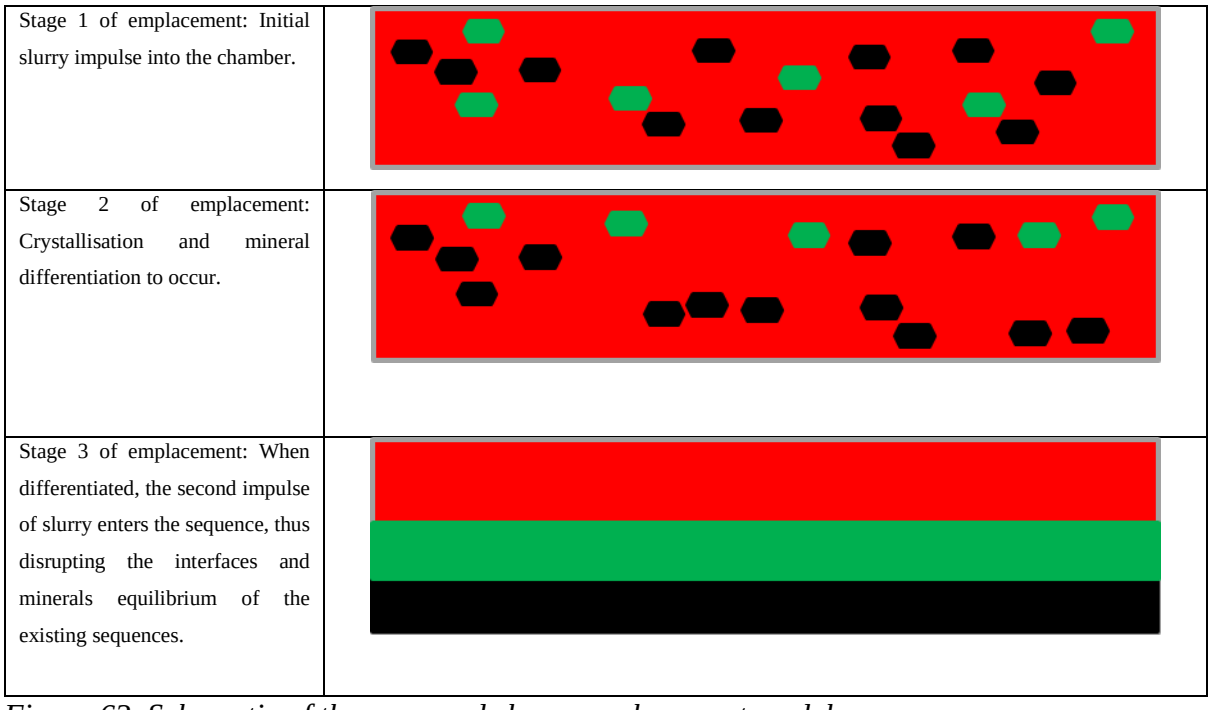

Figure 63. Schematic of the proposed slurry emplacement model.

The slurry emplacement model seen in Figures 63 fails to explain the reverse cryptic variations observed. So, the below models (lower chamber, or sub-chamber, could be at the crust-mantle boundary), as seen in Figure 64, can potentially explain the more primitive HW rocks. The model illustrated here is based on the concepts derived from arc-related ignimbrite deposits (Hildreth, 1981).

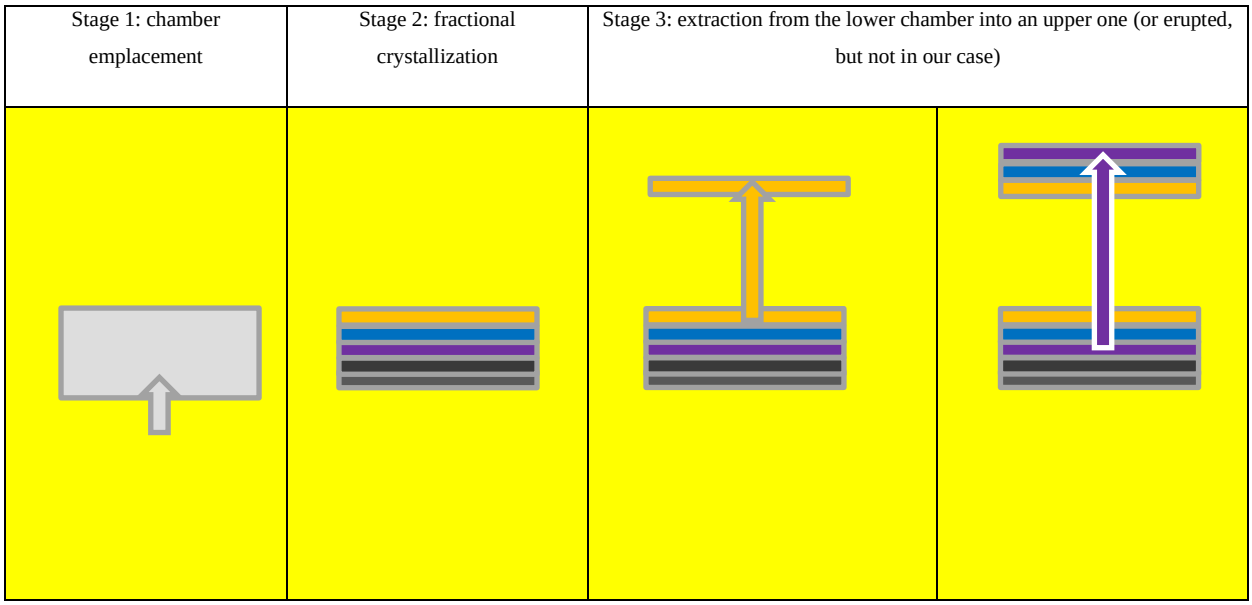

Figure 64. Emplacement of a more primitive magma to create the HW of MG 1.

Alternatively, Mungall *et al.* (2016) proposed that, as a response to localized stress field modification resulting from a sill emplacement, subsequent sills are emplaced within a specific time (beyond which the stress field re-equilibrates) would be preferentially emplaced below their predecessor (Figure 65). This mechanism would explain this specific relationship and would be consistent with a rapidly emplaced, lithologically-similar suite of rocks.

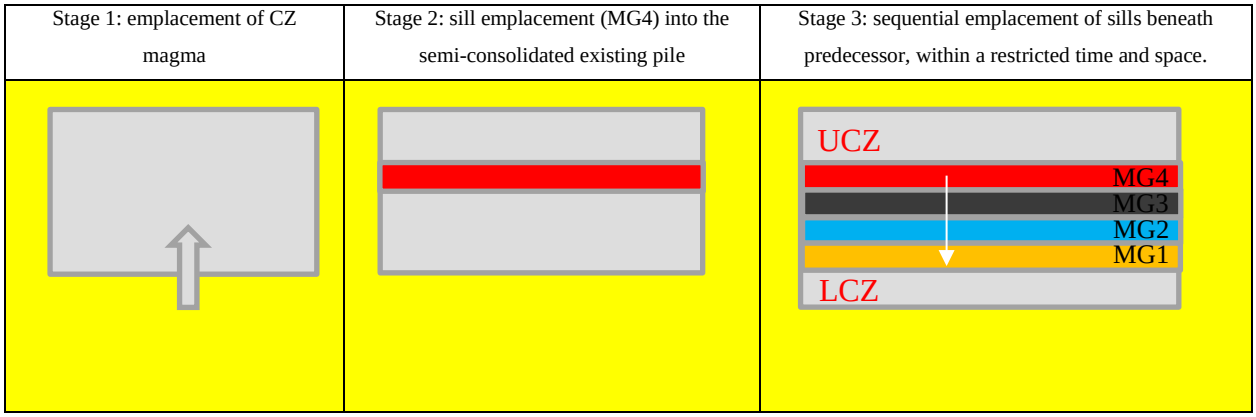

Figure 65. Schematic illustrating the sill emplacements to form the MG chromitites.

This is not to say that this is being proposed as the emplacement model for the entire Bushveld, nor even for the Critical Zone, but that more primitive magma was emplaced above more evolved magma as a possibility locally, specifically for these two units (also consistent with Mungall *et al.*, 2016).

The occurrence of cumulus plagioclase in the upper sills and in the overlying non-chromititic pyroxenites is problematic in different ways for both models. For the inverse emplacement level model, it is not clear how plagioclase could join pyroxene on the liquidus for earlier magma pulses (MG 4 & 3) but then revert to occurring as a later phase in the subsequent pulses (MG 2 & 1). It could be argued that the original differentiating magma pulse had achieved plagioclase-liquidus independently of these MG sills, but then it would seem to require that the cumulus plagioclase in subsequent sills was a coincidence, wherein the HW of the MG 3 contained cumulus plagioclase but not the entire FW of the suite. Similarly, though, the extraction of sequentially emplaced sills from a deepening source would require that the deeper, more chemically primitive source magma is nonetheless evolving towards plagioclase stability.

Chapter 6

Conclusion

This thesis represents a high-partial resolution study (5 cm sections) of the MG 1 and 3 chromitite suite (HW, chromitites and FW); this contrasts with existing published studies that have larger sample spacings, albeit over larger sections. The trends, anomalies and interpretations have taken the scaling effects into account.

The evidence presented allows for the discounting of some chromitite formation models:

a) The typical emplacement and fractional crystallisations remain unlikely due to the reverse cryptic variation observed in the chromitites suggested by the An and En content of minerals increasing upwards with HFSE (Zr) & LILE (Rb) decreasing upwards.
b) The magma mixing and crustal contamination models are discounted due to the lack of phase relationships as well as the lack of mineralogical variability between the HW and FW of the MG 1 and MG 3 chromitites.

There are noticeable differences in the HW and FW between the two chromitite seams. The chromitite acted as a PGE cluster scavenger as it settled within the magma. Or crystallisation of separate PGE minerals along with the chromite. There are sharp contacts along the reefs' FW and HW, with the only wavy pattern observed in a sole stringer MG 1 HW & FW. Samples with disequilibrium rims along some contact grains can indicate mineral grains that were not suited to the environment surrounding them. Moving onto the trends and observations made that doesn’t allow for the excluding of chromitite formations and emplacement:

a) Crystal accumulation had occurred due to, the non-cotectic mineral proportions, the presence of cumulate textures in both chromitites and the deformation of interstitial plagioclase in MG 1. The texture of the plagioclase was formed by high strain rates and low temperatures.
b) Prolonged heating trends such as the recrystallised chromites and cpx exsolution lamellae.
c) The changes in ephemeral properties such as pressure, temperature and oxidation state cannot be discounted in this study.

Therefore, it is suggested that a slurry sill model seems the most likely with likely micro-scale remobilisation of elements to create the observed reversals in the HW and FW rocks of the MG 3 and MG 1.

Chapter 7

References

- Ashwal, L.D. (2010). The Temporality of Anorthosites. The Canadian Mineralogist. **48**. 711-728.
- Barnes S.J, Naldrett, A.J and Gorton, M.P. (1985). The origin of the fractionation of platinum-group elements in terrestrial magmas. Chemical Geology. **53**. 303-323.
- Barnes S-J. and Ripley, E.M. (2016). Highly siderophile and strongly chalcophile elements in magmatic ore deposits. In: highly siderophile and strongly chalcophile elements in high temperature geochemistry and cosmochemistry. Editors J. Havey and J.M. Day Reviews in Mineralogy and Geochemistry. **81**: 725-774**.**
- Barnes, S-J., and Maier, W.D. (2002). Platinum-group element distributions in the Rustenberg Layered Suite of the Bushveld Complex, South Africa. In the Geology, Geochemistry, Mineralogy and Mineral Beneficiation of Platinum-Group Elements. Edited by L.J. Cabri, Canadian Institute of Mining, Metallurgy and Petroleum, Special Volume **54**, p.431-458.
- Bartie N.J. (2004). The effects of temperature, slag chemistry and oxygen partial pressure on the behaviour of chromium oxide in melter slags. MSc Thesis. Dept. of Process Engineering at the University of Stellenbosch.
- Boorman, S., Boudreau, A., and Kruger F.J. (2004). The Lower Zone-Critical Zone Transition of the Bushveld Complex: a Quantitative Textural Study. Journal of Petrology. **45**. 1209-1235.
- Boudreau, A.E. (2008). Modeling the Merensky Reef, Bushveld Complex, Republic of South Africa. Contributions to Mineral and Petrology. **156**. 431-437.
- Burnham O.M, Hechler J.H, Semenyna L and Schweyer J. (2002). Mineralogical Controls on the Determination of Trace Elements Following Mixed Acid Dissolution. Ontario Geological Survey. 6100. 36-1 to 36-12.
- Burnham O.M. (2008). Trace Element Analysis of Geological Samples by Inductively Coupled Plasma Mass Spectrometry (ICP-MS) at the Geoscience Laboratories: Revised Capabilities Due to Method Improvements. Ontario Geological Survey. 6226. 38-1 to 38-10.
- Campbell, I.H. (1978). Some problems with the cumulus theory. Lithos. **11**. 311-323.

- Caricchi, L., Burlini, L., Ulmer, P., Gerya, T., Vassali, M. & Papale, P. (2007). Non-Newtonian rheology of crystal-bearing magmas and implications for magma ascent dynamics. Earth and Planetary Science Letters. **264**. 402-419.
- Cawthorn R.G and Spies L. (2003). Plagioclase content of cyclic units in the Bushveld Complex, South Africa. Contribution Mineral Petrology. **145**. 47-60.
- Cawthorn, R.G. (1999). The platinum and palladium resources of the Bushveld Complex. South African Journal of Science. **95**. 481-489.
- Cawthorn, R.G. (2006). Cr and Sr: Keys to parental magmas and the processes in the Bushveld Complex, South Africa. Lithos. **95**. 381-398.
- Chromium mine production worldwide 2020 | Statista accessed on 2021/03/03.
- Ciborowski, T.J.R., Kerr, A.C., Ernst, R.E., McDonald, I., Minifie, M.J., Harlan, S.S., and Millar, I.L. (2015). The early Proterozoic Matachewan Large Igneous Province: Geochemistry, Petrogenesis, and Implications for Earth Evolution. Journal of Petrology. **56**. 1459-1494.
- Claeson D.T. (1998). Corona, reaction rims, symplectites and emplacement depth of the Rymmen gabbro, Transscandinavian Igneous Belt, southern Sweden. Mineralogical Magazine. **62**. 743-757.
- Dyan, S. (2021) Constraining the role of carbonate assimilation on spinel stability in oxide ores of the Flatreef, Bushveld Complex, South Africa. Unpublished M.Sc. thesis, Rhodes University, Makhanda, RSA. 137 pp. + appendices.
- Eales H. V. (2000). Implications of the chromium budget of the Western Limb of the Bushveld Complex. South African Journal Geology. **103**. 141.
- Eales H.V and Costin G. (2012). Crustally Contaminated Komatiite: Primary Source of the Chromitites and Marginal, Lower and Critical Zone Magmas in the Staging Chambers Beneath the Bushveld Complex. Economic Geology. **107**. 645-665.
- Eales H.V, Field M, de Klerk W.J and Scoon R.N. (1988). Regional trends of chemical variation and thermal erosion in the Upper Critical Zone, Western Bushveld Complex. Mineralogical Magazine. **52**. 63-79.
- Eales, H.V. and Cawthorn, R.G. (1996). The Bushveld Complex. In: Cawthorn, R.G. (ed.): Layered intrusions. Elsevier Science B.V., 181-229.
- Eales, H.V., Botha, W.J., Hattingh, P.J, de Klerk, W.J, Maier, W.D and Odgers, A.T.R. (1993). The mafic rocks of the Bushveld Complex: a review of emplacement and

crystallisation history, and mineralisation, in the light of recent data. Journal of African Earth Sciences. **16**. 121-142

- Eales, H.V. and Marsh, J.S. (1983). Al/Cr ratios of coexisting pyroxenes and spinellids in some ultramafic rocks. Chemical Geology. **38**. 57-74.
- Eales, H.V., Marsh, J.S., Mitchell, A.A., de Klerk, W.J., Kruger, F.J, and Field, M. (1986). Some geochemical constraints upon models for the crystallisation of the upper critical zone-main zone interval, north-western Bushveld complex. Mineralogical Magazine. **50**. 567-582.
- Finnigan, C.S., Brenan, J.M., Mungall, J.E., and McDonough, W.F. (2008). Experiments and Models Bearing on the Role of Chromite as a Collector of Platinum Group Minerals by Local Reduction. Journal of Petrology. **49**. 1647–1665.
- Fleet M.E and Pan Y. (1994). Fractional crystallisation of anhydrous sulphide liquid in the system Fe-Ni-Cu-S with application to magmatic sulphide deposits. Geochimica et Cosmochimica Acta. **58**. 3369-3377.
- Ganino, C., Arndt, N.T., Zhou, M.-F., Gaillard, F. and Chauvel, C. (2008a). Interaction of magma with sedimentary wall rock and magnetite ore genesis in the Panzhihua mafic intrusion, SW China. Mineralium Deposita. **43**. 677–694.
- Godel B, Barnes S.J and Maier W.D. (2007). Platinum-Group Elements in Sulphide Minerals, Platinum-Group Minerals, and Whole-Rocks of the Merensky Reef (Bushveld Complex, South Africa): Implications for the Formation of the reef. Journal of Petrology. **48**. 1569-1604
- Gräbe, P.J. 2014. Merafe Resources. Mineral Resources and Mineral Reserve Report.
- Graham, S.D., Holwell, D.A., McDonald, I., Jenkin, G.R.T., Hill, N.J., Boyce, A.J., Smith, J. and Sangster, C. (2017). Magmatic Cu-Ni-PGE-Au sulphide mineralisation in alkaline igneous systems: An example from the Sron Garbh intrusion, Tyndrum, Scotland. Ore Geology Reviews. **80**. 961-984.
- Haldar, S.K. (2018). Chapter 2 - Economic Mineral Deposits and Host Rocks, Editor(s): Swapan Kumar Haldar, Mineral Exploration (Second Edition), Elsevier. 25-45.
- Hatton C. J. & von Gruenewaldt G. (1989). The geological setting and petrogenesis of the Bushveld chromitite layers. In Stowe C. W. ed. Chromite deposits through time. International Geological Congress, Washington. **11**. 109-142.
- Hildreth, W. (1981). Gradients in silicic magma chambers: Implications for lithospheric magmatism. Journal of Geophysical Research. **86**. 10153-10192.

- Hollocher, K. (2005). cipwnormexcel. Geology Department. Union College. New York.
- Howarth, G.H. and Prevec, S.A. (2013). Hydration vs oxidation: Modelling implications for Fe–Ti oxide crystallisation in mafic intrusions, with specific reference to the Panzhihua intrusion, SW China. Geoscience Frontiers. **4**. 555-569.
- Irvine T, N. (1975). Crystallisation sequences in the Muskox intrusion and other layered intrusions-II. Origin of chromitite layers and similar deposits of other magmatic ores. Geochimica Cosmochimica Acta, **39**. 991–1020
- Irvine T, N., Keith D, W. and Todd S, G. (1983). The J-M platinum palladium reef of the Stillwater Complex, Montana: II Origin by double diffusive convective magma mixing and implications for the Bushveld Complex. Economic Geology. **78**.1287–334
- Irvine T. N. (1977). Origin of chromitite layers in the Muskox intrusion and other stratiform intrusions: a new interpretation. Geology. **5**. 273–277.
- Jackson S.E, Fryer B.J, Gosse W, Healey D.C, Longerich H.P and Strong D.F. (1990). Determination of the precious metals in geological materials by inductively coupled plasma-mass spectrometry (ICP-MS) with nickel sulphide fire-assay collection and tellurium coprecipitation. Chemical Geology. **83**. 119-132.
- Johnson, M.R, Anhaeusser, C.R and Thomas, R.J. (2006). The Geology of South Africa. The Geological Society of South Africa. South Africa.
- Junge, M., Obethür, T, and Melcher, F. (2014). Cryptic variation of chromite chemistry, platinum group element and platinum group mineral distribution in the UG-2 chromitite: An example from the karee mine, western Bushveld complex, South Africa. Economic Geology. **109**. 795-810.
- Kaufmann, F.E.D, Vukmanovic, Z, Holness, M.B and Hecht, L. (2018). Orthopyroxene oikocrysts in the MG1 chromitite layer of the Bushveld Complex: implications for cumulate formation and recrystallisation. Contributions to Mineralogy and Petrology. **173**.
- Keating G.L and Burnham O.M. (2013). Revision of the Calibration for Trace Element Analysis of Geological Samples by Wavelength Dispersive X-Ray Fluorescence at the Geoscience Laboratories. Ontario Geological Survey. Open File Report. 6290. 46-1 to 46-6.
- Kinnaird, J.A., Kruger, F.J., Nex, P.A.M. and Cawthorn, R.G. (2002): Chromitite formation – a key to understanding processes of platinum enrichment. Transactions of

the Institution of Mining and Metallurgy (Section B: Applied Earth Sciences.) **111**, B23-B35.

- Kottke-Levin, J. (2011). A geochemical study of the Middle Group chromitites, Helena mine, Bushveld complex, South Africa. PhD Thesis. University of Free State.
- Kruger J. (2005). Filling the bushveld complex magma chamber: lateral expansion, roof and floor interaction, magmatic unconformities, and the formation of giant chromitite, PGE and T-Magnetite deposits. Mineralium Deposita .**40**. 451-472.
- Latypov, R., Chistyakova, S., Costin, G., Namur, O., Barnes, S. and Kruger, W. (2020). Monomineralic anorthosites in layered intrusions are indicators of the magma chamber replenishment by plagioclase-only-saturated melts. Scientific reports: nature research. **10:3839**. https://doi.org/10.1038/s41598-020-60778-w
- Latypov, R., Costin, G., Chistyakova, S., Hunt, E.J., Mukherjee, R. and Naldrett, A.J. (2018b). Platinum-bearing chromite layers are caused by pressure reduction during magma ascent. Nature Communications. **9**. 462.
- Le Maitre, R.W. (2002). Igneous rocks a Classification and Glossary of Terms Recommendations of the International Union of Geological Sciences, Sub-Commission on the Systematics of Igneous Rocks, Cambridge University Press, 236 p. http://dx.doi.org/10.1017/CBO9780511535581
- Lee C.A and Fesq H.W. (1986). Au, Ir, Ni and Co in some chromitites of the eastern Bushveld Complex South Africa. Chemical Geology. **62**. 227-237.
- Lehohla, P.J. (2015). Report No. 20-01-02 (2015). Mining industry 2015. Statistics South Africa. 1-38.
- Li C, Barnes S.J, Makovicky E, Rose-Hansen J and Makovicky M. (1995). Partitioning of nickel, copper, iridium, rhenium, platinum, and palladium between Monosulphide solid solution and sulphide liquid: Effects of composition and temperature. Geochimica et Cosmochimica Acta. **60**.1231-1238.
- Lipin, B.R. 1992. Pressure Increases, the Formation of Chromitite Seams, and the Development of the Ultramafic Series in the Stillwater Complex, Montana. U.S Geological Survey. Journal of Petrology, **34**. 955-976.
- Liu Y and Brenan J. (2015). Partitioning of platinum-group elements (PGE) and chalcogens (Se, Te, As, Sb, Bi) between monosulphide-solid solution (MSS), intermediate solid solution (ISS) and sulphide liquid at controlled fO_2-fS_2 conditions. PhD Thesis. https://hdl.handle.net/1807/79746.

- Liu Y and Brenan J. (2015). Partitioning of platinum-group elements (PGE) and chalcogens (Se, Te, As, Sb, Bi) between monosulphide-solid solution (MSS), intermediate solid solution (ISS) and sulphide liquid at controlled fO_2-fS_2 conditions.
- Lodders, K. (2003). Solar system abundances and condensation temperatures of the elements. The Astrophysical Journal. **591**. 1220-1247.
- Lowenstern, J.B. (2001). Carbon dioxide in magmas and implications for hydrothermal systems. Mineralium Deposita. **36**. 490-502.
- Maier W.D and Barnes S.J. (1998). Concentration of rare earth elements in silicate rocks of the Lower, Critical and Main Zones of the Bushveld Complex. Chemical Geology. **150**. 85-103.
- Maier W.D, Barnes S.J., de Klerk W.J., Teigler B & Mitchell A.A. (1996). Cu/Pd and Cu/Pt of silicate rocks in the Bushveld Complex: Implications for platinum-group element exploration. Economic Geology. **91**. 1151-1158.
- Maier, W.D and Barnes S.J. (1998). Concentrations of rare earth elements in silicate rocks of the Lower, Critical and Main zones of the Bushveld Complex. Chemical Geology.**150**. 85-103.
- Maier, W.D., Barnes, S.J and Groves, D.I. (2013). The Bushveld Complex, South Africa: formation of platinum–palladium, chrome- and vanadium-rich layers via hydrodynamic sorting of a mobilized cumulate slurry in a large, relatively slowly cooling, subsiding magma chamber. Mineralium Deposita. **48**. 1-56.
- Manning, C.E., and Aranovich, L.Y. (2014). Brines at high pressure and temperature: Thermodynamic, petrologic, and geochemical effects. Precambrian Research. **235**. 6-16.
- McBirney, A.R. (1989). The Skaergaard Layered Series: I. Structure and average compositions. Journal of Petrology. **30**. 363-397.
- McBirney, A.R & Noyes, R.M. (1979). Crystallisation and Layering of the Skaergaard Intrusion. Journal of Petrology. **20**. 487-554
- McDonough W.F and Sun S. (1994). The composition of the Earth. Chemical Geology. **120**. 223-253.
- McDonough, W.F. and Sun, S.S. (1995). The Composition of the Earth; Chemical Geology. **120**. 223-253.

- Mondal, S.K. (2011). Platinum group element (PGE) geochemistry to understand the chemical evolution of the Earth's mantle. Journal of the Geological Society of India.**77**. 295.
- Mungall, J.E and Brenan, J.M. (2014). Partitioning of platinum-group elements and Au between sulphide liquid and basalt and the origins of mantle-crust fractionation of the chalcophile elements. Geochimica et Cosmochimica Acta. **125**. 265-289.
- Mungall, J.E., Kamo, S., & McQuade, S. (2016). U–Pb geochronology documents out-of-sequence emplacement of ultramafic layers in the Bushveld Igneous Complex of South Africa. Nature Communications. **7**. 13385.
- Murck, B.W & Campbell, I.H. (1986). The effects of temperature, oxygen fugacity and melt composition on the behaviour of chromium in basic and ultrabasic melts. Geochimica et Cosmochimica Acta. **50**. 1871-1887.
- Naldrett, A.J. and von Gruenewaldt. (1989). Association of Platinum-Group Elements with Chromitite in Layered Intrusions and Ophiolite Complexes. Economic Geology. **84**. 180-187.
- Osbahr I, Oberthur T., and Klemd R. (2015). PGE distribution in base-metal sulphides from the Merensky Reef of the Bushveld Complex, South Africa. Goldschmidt Conference Abstracts. 1575**.**
- Papp J.F. (2017). Chromium: U.S Geological Survey, Mineral Commodity Summaries. 703. 648
- Papp, J.F and Lipin, B.R. (2011). Chromium. Handbook of Chemical Economics, Inorganic. Handbook of Chemical Industry Economics, Inorganic. 1-102.
- Perugini, D., Busà, T., Poli, S and Nazzareni, S. (2003). The role of chaotic dynamics and flow fields in the development of disequilibrium textures in volcanic rocks. Journal of Petrology. **44**. 733-756.
- Prevec, S.A., Largatzis, S.A., Brownscombe, W, and Salge, T. (2021). PGE distribution in the Merensky wide-reef facies of the Bushveld Complex, South Africa: Evidence for localized hydromagmatic control. The Canadian Mineralogist. **59**. 1305-1338.
- Prevec, S.A. (2018). Igneous Rock Associations 23. The Bushveld Complex, South Africa: New Insights and Paradigms. Geoscience Canada. **45**. 117-135.
- Prevec, S.A. (2021). Honours class presentation notes. Rhodes University. RSA.

- Prevec, S.A. Largatzis, S.A., and Raines, M.E. (2016). Constraints on the origins of PGE-mineralized chromitite reefs from PGE distributions and isotopic compositions of the Merensky Reef, Bushveld Complex, South Africa. Penrose Conference.
- Scoon, R.N and Teigler, B. (1994). Platinum-group element mineralization in the critical zone of the western bushveld complex: I. Sulphide poor-chromitites below the UG-2. Economic Geology. **89**. 1094-1121.
- Sharpe, M.R. and Irvine, T.N. (1983). Melting relations of two Bushveld chilled margin rocks and implications for the origin of chromitite. Carnegie Institute Washington, Yearb. **82**. 295-300.
- South African Committee for Stratigraphy. (1980). Stratigraphy of South Africa. Part 1, Lithostratigraphy of the Republic of South Africa, Southwest Africa/Namibia, and the Republics of Bophutswana, Transkei and Venda. Handbook Geological Survey South Africa. **8**. 690.
- Strickland, J, Nenchev, B, Perry, S, Tassenberg, K, Gill, S, Panwisawas, C, Dong, H, D'Souza, N and Irwin, S. (2020). On the nature of hexagonality within the solidification structure of single crystal alloys: Mechanisms and applications, Acta Materialia. **200**. 417-431,
- Teigler B. and Eales H. V. (1993). Correlation between chromite composition and PGE mineralisation in the Critical Zone of the western Bushveld Complex. Mineral. Deposita. **28**. 291–302
- Teigler, B., Eales, H.V. and Scoon, R.N. (1992). The cumulate succession in the Critical Zone of the Rustenberg Layered Suite at Brits, western Bushveld Complex. Mineralium Deposita.
- Tredoux M, Lindsay N.M, Davies G, McDonald I. (1995). Fractionation of platinum-group elements in magmatic systems with the suggestion of a novel causal mechanism. South African Journal of Geology. **98**. 157-167.
- Tredoux, M., Lindsay, N.M., Davies, G., and McDonald, I. (1995). The fractionation of platinum-group elements in magmatic systems, with the suggestion of a novel causal mechanism. South African Journal of Geology. **98**. 157-167.
- Ulmer, G.C. (1969). Experimental investigation of chromite spinels. Economic Geology Monograph. **4**. 114-131.

- Von Gruenewaldt G and Merkle R.K.W. (1995). Platinum-group element proportions in chromitites of the Bushveld complex: implications for fractionation and magma mixing models. Journal of African Earth Sciences. **21**. 615-632.
- Wager L.R, Brown G.M and Wadsworth W.J. (1960). Types of igneous cumulates. Journal of Petrology.**1**.73-85.
- Wager, L.R. (1963). The mechanism of Adcumulus growth in the layered series of the Skaergaard intrusion. Mineral Society American Special Papers. **1**. 1-9.
- Wager, L.R., Brown, G.M., & Wadsworth, W.J. (1960). Types of igneous cumulates. Journal of Petrology. **1**. 23-48.
- Wallmach. T, Hatton. C.J, De Waal. S.A and Gibson R.S. (1995). Retrogressive hydration of calc-silicate xenoliths in the eastern Bushveld complex: evidence for late magmatic fluid movement. Journal of African Earth Sciences. **21**. 633-646.
- Winter, J.D. (2010). Principles of Igneous and Metamorphic Petrology. 2nd Edition. Pearson publishers. USA. 222-242.
- Zaccarini F, Pushkarev V.E, Fershtater B.G, Cabella R and Garuti G. (2002). Platinum Group Element Mineralogy and Geochemistry in chromitites of the Nurali Mafic-Ultramafic Complex (Southern Urals, Russia). Unpublished work.
- Zientek M.L. (2012). Magmatic Ore Deposits in Layered Intrusions—Descriptive Model for Reef-Type PGE and Contact-Type Cu-Ni-PGE Deposits. USGS

Chapter 8

Appendix

8.1 Whole rock analyses

Table 4: Whole rock analysis of the MG 3 chromitites (Part 1).

Depths	Al2O3	BaO	CaO	Cr2O3	Fe2O3	K2O	LOI	MgO	MnO	Na2O	P2O5	SiO2	TiO2	V2O5	Majors Sum		Co	Cu	Ni	Zn	Cr ppm	Ti
291,52	19.35	0.01	9.563	0.98	7.08	0.12	-0.12	11.67	0.126	1.42	0.004	50.5	0.14		100.83	MG 41					6705.16	0.083931
291.68	15.44	<0.004	7.954	1.02	8.55	0.09	-0.23	15.06	0.156	1.13	0.004	50.93	0.15		100.26	MG 42					6978.84	0.089927
291.88	17.35	0.01	8.828	0.64	7.62	0.09	-0.18	13.62	0.143	1.3	0.002	51.23	0.13		100.78	MG 43					4378.88	0.077936
292.43	17.15	0.01	8.729	0.62	7.65	0.1	-0.11	13.99	0.146	1.25	0.002	51.37	0.12		101.01	MG 44					4242.04	0.071941
292.45	15.59	0.01	7.901	1.18	8.57	0.11	-0.13	15.31	0.158	1.11	<0.002	50.84	0.15		100.79	MG 45					8073.56	0.089927
292.47	12.49	<0.008	5.029	8.545	13.62	0.09	<0.05	16.88	0.173	0.715	<0.004	42.37	0.32	0.107	100.112	MG 46	119	50	598	181	58464.89	0.191843
292.52	5.9	<0.008	2.458	8.841	16.02	0.04	<0.05	22.67	0.208	0.375	0.017	44	0.45	0.096	100.585	MG 18+19	135	50	718	207		0.26978
292.57	17.14	<0.008	1.667	36.412	28.72	0.08	<0.05	9.15	0.166	0.234	<0.004	8.28	0.86	0.38	101.901	20+21	275	90	999	642	249130.9	0.515579
292.93	16.83	0.012	2.248	31.447	26.18	0.09	<0.05	10.3	0.163	0.384	<0.004	14.34	0.74	0.281	101.784	24+25	268	142	925	581	215160.4	0.443637
293.48	18.94	0.018	4.183	26.695	22.12	0.08	<0.05	8.86	0.157	0.615	<0.004	19.3	0.58	0.3	100.808	27+28	218	81	779	519	182647.2	0.347716
293.5	11.23	0.02	5.682	1.58	11.12	0.28	0.07	17.78	0.196	0.88	0.043	51.72	0.16		100.77	MG 29					10810.36	0.095922
293.55	18.54	0.01	9.099	0.18	7.51	0.39	0.22	10.8	0.143	1.52	0.089	52.19	0.11		100.80	MG 30					1231.56	0.065946
293.67	27.74	0.01	12.109	4.92	6.11	0.27	-0.11	2.8	0.057	2.07	0.01	43.74	0.2		99.92	MG 31					33662.64	0.119902

Depths	Al2O3	BaO	CaO	Cr2O3	Fe2O3	K2O	LOI	MgO	MnO	Na2O	P2O5	SiO2	TiO2	V2O5	Majors Sum		Co	Cu	Ni	Zn	Cr ppm	Ti
293.7	15.92	0.011	3.214	27.885	25.46	0.05	<0.05	10.27	0.184	0.382	<0.004	19.13	0.68	0.347	101.557	MG 32	220	50	746	565	190789.2	0.407667
293.73	24.63	<0.008	11.927	7.442	8.78	0.13	<0.05	4.43	0.077	1.757	0.006	41.38	0.35	0.117	100.802	MG 33	65	78	278	154	50918.16	0.209829
293.76	28.12	<0.004	14.292	0.17	2.8	0.18	0.23	3.06	0.052	2.15	0.004	49.44	0.08		100.58	MG 34					1163.14	0.047961
293.83	32.03	0.01	15.072	0.13	1.4	0.19	0.27	0.21	0.026	2.39	0.004	48.81	0.06		100.60	MG 35					889.46	0.035971
293.88	26.31	0.01	12.694	0.09	4.22	0.15	0.14	5.24	0.077	1.92	0.003	50.15	0.07		101.07	MG 36					615.78	0.041966
293.98	31.64	0.01	15.137	0.09	1.5	0.16	0.24	0.46	0.027	2.34	0.002	48.85	0.05		100.51	MG 37					615.78	0.029976
295	29.58	0.01	14.287	0.07	2.38	0.18	0.24	2.11	0.043	2.16	0.007	49.58	0.07		100.72	MG 38					478.94	0.041966

Table 5. Whole rock analysis of the MG 3 chromitites (Part 2).

Client ID	Unit	Detect Limit	MG 41	MG 42	MG 43	MG 44	MG 45	MG 46	MG 18+19	MG 20+21	MG 24+25	MG 27+28	MG 29	MG 30	MG 31	MG 32	MG 33	MG 34	MG 35	MG 36	MG 37	MG 38
Ba	ppm	0.8	49.1	41.6	43.2	43.9	46.6	40.6	24.6	26.5	34.5	34.5	152.7	132.8	96.1	24.9	60.9	53.8	71.6	42.9	59.8	49.4
Be	ppm	0.04	0.23	0.26	0.19	0.22	0.23	0.26	0.14	0.18	0.2	0.19	0.34	0.48	0.37	0.14	0.29	0.39	0.34	0.19	0.27	0.29
Bi	ppm	0.47	<0.47	<0.47	<0.47	<0.47	<0.47	<0.47	<0.47	<0.47	<0.47	<0.47	<0.47	<0.47	<0.47	<0.47	<0.47	<0.47	<0.47	<0.47	<0.47	<0.47
Cd	ppm	0.013	0.018	0.013	0.027	0.043	0.03	0.032	0.023	<0.013	0.029	0.037	0.061	0.054	0.035	0.033	0.028	0.043	0.015	0.017	0.025	0.03
Ce	ppm	0.12	3.27	2.71	2.72	2.46	2.52	2.88	2.16	2.82	3.74	2.32	9.55	18.86	7.56	1.53	3.9	3.52	3.02	2.22	2.6	3.39
Co	ppm	0.13	51.1	63.31	54.23	54.78	64.73	106.35	187.00	187.00	187.00	187.00	76.71	42.49	44.46	187	67.18	14.37	3.65	23.17	4.01	10.79
Cr	ppm	3	6705.16	6978.84	4378.88	4242.04	8073.56	58464.89	287931886.00	249130904.00	215160374.00	18264 7.19	10810.36	1231.56	33662.64	190789.2	50 918 164	1163.14	889.46	615.78	615.78	478.94
Cs	ppm	0.013	0.064	0.037	0.04	0.036	0.042	0.099	0.242	0.153	0.088	0.073	0.227	0.585	0.107	0.028	0.054	0.059	0.043	0.038	0.036	0.07
Cu	ppm	1.4	14.9	17.2	17.7	16.8	17.7	21.4	32.4	34.3	29.9	23.2	32.8	18.7	19.8	25.3	47.8	26.5	16.5	26.3	12.3	13.5
Dy	ppm	0.009	0.288	0.33	0.29	0.263	0.304	0.525	0.26	0.2	0.376	0.251	1 580	1 943	0.393	0.226	0.577	0.371	0.117	0.16	0.133	0.203
Er	ppm	0.007	0.209	0.27	0.203	0.191	0.232	0.39	0.152	0.133	0.248	0.154	1 087	1 143	0.199	0.183	0.318	0.204	0.053	0.12	0.074	0.128
Eu	ppm	0.0031	0.2833	0.2383	0.2545	0.2565	0.2725	0.2212					0.3893	0.6626	0.5639	0.1386	0.3857	0.3473	0.378	0.2412	0.3321	0.3032

Client ID	Unit	Detect Limit	MG 41	MG 42	MG 43	MG 44	MG 45	MG 46	MG 18+19	MG 20+21	MG 24+25	MG 27+28	MG 29	MG 30	MG 31	MG 32	MG 33	MG 34	MG 35	MG 36	MG 37	MG 38
Ga	ppm	0.04	13.83	11.81	12.08	12.08	11.96	18.19	0.0661	0.1	0.1743	0.1908	10.01	12.73	24.53	45.51	25.18	18.52	20.56	16.47	19.78	18.75
Gd	ppm	0.009	0.261	0.276	0.234	0.227	0.259	0.401					1 309	2 120	0.522	0.17	0.515	0.358	0.164	0.146	0.174	0.263
Hf	ppm	0.14	0.21	0.22	0.15	0.15	<0.14	0.23	53.54	52	51.15	46.27	0.46	3.44	0.38	0.2	0.27	0.26	0.14	0.19	0.14	0.24
Ho	ppm	0.0025	0.0629	0.07 64	0.0631	0.058	0.0671	0.1183					0.3476	0.4049	0.0738	0.0515	0.1132	0.0729	0.0207	0.0309	0.0276	0.0443
In	ppm	0.0018	0.0125	0.0151	0.0122	0.013	0.0155	0.0224	0.246	0.238	0.348	0.218	0.023	0.0157	0.0076	0.0319	0.016	0.009	0.0031	0.0086	0.0038	0.0054
La	ppm	0.1	1.74	1.6	1.59	1.4	1.42	1.62					4.68	9.06	3.96	0.97	2.04	2.03	1.78	1.25	1.55	1.95
Li	ppm	0.4	2.8	2.6	2.9	3.2	3	3.3	0.3	0.42	0.32	0.24	3.4	2.6	2.2	0.9	2.6	3	3.6	2.4	3.2	2.9
Lu	ppm	0.002	0.0358	0.045	0.0348	0.0375	0.0399	0.0681					0.1783	0.1673	0.0271	0.0346	0.0435	0.0293	0.0066	0.0205	0.0109	0.0182
Mo	ppm	0.08	1.06	1.02	1.07	0.99	1.08	1.26	0.0447	0.0518	0.0759	0.0557	1.41	2.84	1.17	1.1	1.03	0.83	0.99	0.9	0.98	0.84
Nb	ppm	0.028	0.366	0.307	0.296	0.308	0.261	0.452					0.749	2 916	0.733	0.365	0.279	0.271	0.347	0.254	0.222	0.401
Nd	ppm	0.06	1.36	1.35	1.13	1.04	1.2	1.47	0.0264	0.0266	0.0278	0.0253	5.16	9.82	3.45	0.72	2	1.72	1.29	0.93	1.09	1.43
Ni	ppm	0.7	275.2	356.5	340.9	352.8	407.7	574.7					428.7	230	166.2	690.1	273.7	73.5	18.4	92.7	18	41.7
Pb	ppm	0.18	0.8	0.7	0.7	0.8	0.7	0.7	1.5	0.98	1.96	1.42	1.5	2.3	2.2	0.7	1.4	1.2	1	0.9	1	1
Pr	ppm	0.014	0.374	0.324	0.313	0.286	0.317	0.385					1 254	2 471	0.956	0.207	0.494	0.428	0.368	0.253	0.317	0.412
Rb	ppm	0.11	1.94	1.55	1.34	1.28	1.36	1.53	2.4	1.3	1.2	2.7	6.49	14.73	2.69	1.32	1.72	2.93	2.23	2.09	1.73	3.07
Sb	ppm	0.04	0.14	0.12	0.12	0.13	0.13	0.17					0.22	0.3	0.15	0.14	0.13	0.1	0.12	0.11	0.12	0.1
Sc	ppm	1.1	16.2	19.4	16.8	17	18.8	18.5	0.0184	0.0215	0.0445	0.0267	26.8	18.2	4.4	15	11.6	7.5	<1.1	6.3	1.8	4
Sm	ppm	0.026	0.276	0.273	0.236	0.216	0.254	0.322					1 151	2 142	0.606	0.136	0.51	0.385	0.227	0.164	0.202	0.276
Sn	ppm	0.16	0.68	0.68	0.62	0.6	0.65	0.57	0.48	0.96	0.63	0.53	0.82	1.6	0.51	0.34	0.6	0.56	0.72	0.58	0.59	0.54
Sr	ppm	0.6	253.7	198	238.6	222.1	200.3	115		26.30			132	227.9	317.8	87.7	310.7	346.4	412.4	344.9	393	339.2
Ta	ppm	0.007	0.016	0.014	0.009	0.012	0.008	0.024	0.566	0.908	0.598	0.351	0.053	0.181	0.041	0.016	0.012	0.012	0.015	0.009	0.009	0.024
Tb	ppm	0.0023	0.044	0.04 69	0.0396	0.036	0.0472	0.0717					0.2285	0.3128	0.0714	0.0321	0.0824	0.0585	0.02	0.0226	0.023	0.0316
Th	ppm	0.018	0.205	0.183	0.109	0.112	0.119	0.223	1.29	1.13	1.88	1.25	0.647	2 550	0.46	0.081	0.148	0.142	0.152	0.105	0.126	0.215

Client ID	Unit	Detect Limit	MG 41	MG 42	MG 43	MG 44	MG 45	MG 46	MG 18+19	MG 20+21	MG 24+25	MG 27+28	MG 29	MG 30	MG 31	MG 32	MG 33	MG 34	MG 35	MG 36	MG 37	MG 38
Ti	ppm	7	813	895	741	734	861	1932	4825.00	5245.00	4214.00	3391.00	963	632	1194	4039	2067	452	318	402	275	402
Tl	ppm	0.002	0.012	0.01	0.011	0.012	0.009	0.012	893.7	989.5	819.9	732.4	0.045	0.077	0.034	0.004	0.015	0.031	0.021	0.034	0.008	0.014
Tm	ppm	0.0019	0.0313	0.0406	0.0327	0.0309	0.0351	0.0605					0.1693	0.1711	0.0276	0.0281	0.0453	0.0326	0.0073	0.0163	0.0098	0.0187
U	ppm	0.011	0.055	0.044	0.028	0.03	0.024	0.056	0.7	0.5	0.9	0.8	0.164	0.63	0.149	0.02	0.037	0.052	0.049	0.04	0.036	0.071
V	ppm	0.8																51	29.5	45.6	27.5	35.5
W	ppm	0.05	0.6	0.59	0.55	0.56	0.57	0.72	0.329	0.268	0.441	0.312	0.86	1.58	0.66	0.63	0.56	0.5	0.59	0.5	0.62	0.46
Y	ppm	0.05	1.76	2.13	1.78	1.63	1.91	3.1					9.6	10.81	2.04	1.37	2.97	1.97	0.56	0.97	0.73	1.22
Yb	ppm	0.009	0.226	0.272	0.223	0.224	0.249	0.4	3.81	7.63	3.26	1.61	1 163	1 099	0.169	0.209	0.296	0.204	0.04	0.132	0.061	0.112
Zn	ppm	1.8	52	60	47	51	61	170	566	608	506	467	72	33	99	501	142	18	9	29	10	15
Zr	ppm	6	8	7	<6	<6	<6	8	0.06	0.12	0.08	0.06	17	150	15	6	9	9	6	7	<6	9

Table 6. PGE concentrations of the MG 3 chromitites.

Depth	Client ID	Au	Ir	Pd	Pt	Rh	Ru
	Units	ppb	ppb	ppb	ppb	ppb	ppb
	Detect Limit	0.4	0.01	0.12	0.17	0.04	0.08
291.52	MG 41	2.66	12	41.6	67.3	19.8	48.7
292.43	MG 44	2.98	6.54	55.5	29.8	9.47	28.5
292.45	MG 45	4.68	12.7	141	87.7	26.1	48.2
292.47	MG 46	5.47	103	800	961	264	358
293.48	MG 27+28	1	116	400	1309	280	349
293.5	MG 29	3.87	4.36	108	38.4	9.46	14.9
293.76	MG 34	1.4	7.42	11.5	39	5.69	20.5
295	MG 38	0.99	11.4	11.8	99.8	7.6	26

Table 7: Whole rock analysis of the MG 1 chromitites (Part 1).

Depth	Al2O3	BaO	CaO	Cr2O3	Fe2O3	K2O	LOI	MgO	MnO	Na2O	P2O5	SiO2	TiO2	V2O5	Majors Sum	Co	Cu	Ni	Zn		Ti
314.86	1.71	0.01	1.312	1.29	14.38	0.38	-0.47	27.51	0.25	0.09	<0.002	54.21	0.32		100.99					MG 12	0.191843
314.94	5.21	<0.004	4.163	1.78	12.02	0.06	-0.29	24.14	0.211	0.54	0.01	52.5	0.22		100.56					MG 13	0.131892
315.03	5.62	0.01	3.564	2.06	12.47	0.07	-0.41	24.18	0.215	0.58	0.007	52.24	0.22		100.83					MG 14	0.131892
315.11	6.07	0.01	3.476	1.84	12.09	0.05	-0.33	24.33	0.21	0.55	<0.002	52.45	0.19		100.93					MG 15	0.113907
315.2	5.92	<0.008	2.475	8.851	16.05	0.04	<0.05	22.75	0.203	0.383	0.017	44.14	0.45	0.098	100.88	136	50	715	206	MG 16	0.26978
315.23	9.87	0.008	1.701	23.294	22.27	<0.02	<0.05	18.12	0.212	0.04	<0.004	25.31	0.66	0.202	101.012	216	54	930	403	MG 17	0.395677
315.3	15.86	0.009	0.448	42.083	27.9	<0.02	<0.05	11.07	0.152	0.04	<0.004	3.92	0.78	0.304	101.612	286	50	1056	594	08+09	0.467618
315.36	16.06	0.012	0.141	41.877	28.17	<0.02	<0.05	11.53	0.159	0.04	<0.004	4.11	0.75	0.305	101.671	263	50	1023	740	10	0.449633
315.52	15.2	<0.008	0.964	42.519	28.06	<0.02	<0.05	11.32	0.164	0.04	<0.004	5.14	0.71	0.32	102.064	265	116	1057	572	11	0.425652
315.9	2.33	0.01	1.364	2.14	13.67	0.18	0.61	27.12	0.204	0.07	0.004	51.82	0.27		99.80					MG 01	0.161868
315.92	2.24	0.01	1.564	0.48	12.45	0.25	0.62	25.53	0.209	0.3	<0.002	56.92	0.28		100.84					MG 02	0.167863
315.95	1.59	0.01	1.479	0.57	13.37	0.29	0.38	27.35	0.223	0.12	<0.002	55.12	0.28		100.78					MG 03	0.167863
316.16	6.63	0.01	4.029	0.39	11.78	0.13	-0.33	23.14	0.21	0.68	0.005	53.93	0.2		100.79					MG 05	0.119902
316.36	4.43	0.01	3.189	0.4	12.43	0.19	-0.36	24.64	0.218	0.51	0.003	54.76	0.26		100.66					MG 06	0.155873
316.4	6.21	0.02	3.417	0.42	11.99	0.2	-0.5	23.16	0.213	0.81	0.003	54.16	0.24		100.33					MG 07	0.143882

Table 8. Whole rock analysis of the MG 1 chromitites (Part 2).

Client ID	Units	Detect Limit	MG 12	MG 13	MG 14	MG 15	MG 16	MG 17	MG 08+09	MG 10	MG 11	MG 01	MG 02	MG 03	MG 05	MG 06	MG 07	McDonough and Sun
Ba	ppm	0.8	62	33	35	29.5	24.3	9.1	11.6	1	3.5	46.1	89.5	82.6	60.2	56.7	137.8	2410
Be	ppm	0.04	0.33	0.3	0.26	0.23	0.25	0.13	0.11	0.12	0.18	0.28	0.36	0.26	0.32	0.34	0.39	0.025
Bi	ppm	0.47	<0.47	<0.47	<0.47	<0.47	<0.47	<0.47	<0.47	<0.47	<0.47	<0.47	<0.47	<0.47	<0.47	<0.47	<0.47	110.00
Cd	ppm	0.013	0.054	0.06	0.051	0.044	0.05	0.043	<0.013	<0.013	<0.013	0.058	0.069	0.071	0.073	0.044	0.058	710.00
Ce	ppm	0.12	6.52	4.48	3.62	2.96	3	1.16	0.77	0.43	1.95	3.49	6.02	3.59	5.9	8.13	8.86	613
Co	ppm	0.13	101.97	91.47	91.78	88.46	130.44	187	187	187	187	104.78	83.13	95.94	80.15	83.97	81.7	500
Cr	ppm	3	8826.18	12178.76	14094.52	12589.28	60 558 542	159 377 548	287 931 886	286 522 434	290 914 998	14641.88	3152	3760	2545	2585	2877	2650
Cs	ppm	0.013	0.697	0.074	0.05	0.036	0.064	0.043	0.03	0.019	0.026	0.263	0.404	0.29	0.126	0.237	0.135	190
Cu	ppm	1.4	19.7	42.7	39.1	54.5	25.4	19	9.7	7	33.8	80.6	19	41.8	40.8	47.8	30.8	120
Dy	ppm	0.009	1 021	0.853	0.667	0.556	0.637	0.395	0.103	0.081	0.259	0.934	0.924	0.904	0.879	1 032	0.825	246
Er	ppm	0.007	0.747	0.538	0.453	0.405	0.455	0.28	0.056	0.061	0.142	0.677	0.649	0.675	0.579	0.679	0.599	160
Eu	ppm	0.0031	0.0804	0.246	0.2232	0.2029	0.152	0.0587	0.0297	0.0148	0.0747	0.0914	0.136	0.1121	0.3278	0.2697	0.3204	56.3
Ga	ppm	0.04	5.17	6.89	7.26	7.06	16.26	33.43	50.56	51.82	47.13	7.7	4.38	4.17	6.81	5.45	7.1	9.2
Gd	ppm	0.009	0.735	0.78	0.557	0.451	0.519	0.314	0.106	0.071	0.276	0.755	0.766	0.698	0.719	0.933	0.701	199
Hf	ppm	0.14	0.99	0.33	0.22	0.19	0.24	0.23	0.18	0.16	0.22	0.62	0.81	0.9	0.42	0.71	0.54	103
Ho	ppm	0.0025	0.2303	0.1829	0.1527	0.1251	0.1349	0.0839	0.0251	0.0185	0.0527	0.2047	0.2086	0.216	0.1805	0.219	0.1935	54.6
In	ppm	0.0018	0.0298	0.0232	0.021	0.0205	0.0247	0.0287	0.0231	0.022	0.0258	0.0302	0.0265	0.0256	0.0227	0.0262	0.0235	80
La	ppm	0.1	4.04	2.12	1.9	1.61	1.64	0.47	0.41	0.31	0.83	1.52	3.32	1.69	3.13	4.84	5.15	237
Li	ppm	0.4	5	3.6	3	2.8	2.1	1.4	1.2	1.1	1.2	3.7	4.4	4.5	4.8	3.8	4.2	1.5
Lu	ppm	0.002	0.128	0.0869	0.0749	0.072	0.0779	0.0476	0.0112	0.0099	0.0165	0.1155	0.1131	0.1217	0.0936	0.1115	0.1055	24.6
Mo	ppm	0.08	1.73	0.68	1.01	0.92	1.15	1.24	0.63	1.07	0.73	1.05	0.71	0.76	1.74	1.34	1.76	900
Nb	ppm	0.028	1 607	0.32	0.272	0.145	0.207	0.288	0.333	0.368	0.405	0.753	1 387	1 047	0.697	1 230	1 518	240
Nd	ppm	0.06	2.45	2.66	1.85	1.42	1.68	0.81	0.44	0.22	1.23	2.55	3.03	2.42	2.94	3.99	3.13	457
Ni	ppm	0.7	609.2	588.7	588.5	597.2	689.1	857	954.7	933.5	974.4	840.1	553.1	672.7	428.3	471.4	438.2	10500

Client ID	Units	Detect Limit	MG 12	MG 13	MG 14	MG 15	MG 16	MG 17	MG 08+09	MG 10	MG 11	MG 01	MG 02	MG 03	MG 05	MG 06	MG 07	McDonough and Sun
Pb	ppm	0.18	1.7	1.5	1.3	1.5	1.2	1.2	0.3	0.3	0.3	1.6	2.1	1.6	2	2.2	2.6	2470
Pr	ppm	0.014	0.72	0.613	0.462	0.346	0.42	0.17	0.098	0.05	0.283	0.557	0.77	0.562	0.728	1 039	0.921	92.8
Rb	ppm	0.11	14.8	1.17	1.04	0.68	0.72	1.01	1.82	1.58	1.65	6.3	9.01	10.37	2.97	6.45	4.63	2.3
Sb	ppm	0.04	0.25	0.09	0.13	0.11	0.15	0.15	0.07	0.14	0.1	0.15	0.14	0.13	0.19	0.2	0.21	140
Sc	ppm	1.1	31.1	28.1	25.4	24	22.2	17.3	7.9	8.2	10	28.1	27.6	31.5	25.8	26.5	26	5.92
Sm	ppm	0.026	0.6	0.658	0.471	0.327	0.416	0.235	0.105	0.056	0.304	0.659	0.71	0.625	0.66	0.886	0.633	148
Sn	ppm	0.16	0.86	0.47	0.5	0.45	0.5	0.39	0.26	0.27	0.29	0.28	0.5	0.48	0.88	0.75	0.99	1650
Sr	ppm	0.6	3.6	58.8	61.2	65.8	42.7	15.5	7.7	5.1	11.8	3.9	13.9	5.5	88.6	49.6	81.3	7.25
Ta	ppm	0.007	0.129	0.016	0.01	<0.007	<0.007	0.008	0.01	<0.007	0.013	0.059	0.08	0.058	0.038	0.078	0.092	13.6
Tb	ppm	0.0023	0.1382	0.127	0.0974	0.0743	0.0826	0.059	0.0163	0.0123	0.044	0.1307	0.140 7	0.134 6	0.118 5	0.154 5	0.119 8	36.1
Th	ppm	0.018	1 489	0.148	0.116	0.061	0.076	0.073	0.092	0.099	0.132	1 162	1 214	0.797	0.406	0.728	0.576	29
Ti	ppm	7	1936	1334	1311	1080	2736	3879	4549	4479	4128	1605	1646	1742	1233	1531	1445	440
Tl	ppm	0.002	0.073	0.01	0.008	0.008	0.009	0.011	0.002	0.007	0.003	0.075	0.057	0.058	0.017	0.032	0.023	140
Tm	ppm	0.0019	0.1222	0.0845	0.0705	0.0647	0.0666	0.0427	0.0128	0.0155	0.0245	0.1053	0.102 6	0.107 7	0.092 1	0.100 2	0.095 9	24.7
U	ppm	0.011	0.453	0.045	0.032	0.017	0.022	0.011	0.02	0.023	0.032	0.127	0.24	0.122	0.098	0.275	0.289	7.4
W	ppm	0.05	1.06	0.37	0.56	0.47	0.65	0.72	0.34	0.62	0.42	0.64	0.48	0.45	0.93	0.75	1.08	93
Y	ppm	0.05	6.26	4.84	3.93	3.43	3.75	2.23	0.66	0.52	1.29	5.51	5.78	5.92	5	5.89	5.15	1.57
Yb	ppm	0.009	0.825	0.573	0.5	0.458	0.468	0.284	0.063	0.059	0.106	0.729	0.725	0.761	0.634	0.697	0.656	161
Zn	ppm	1.8	90	83	88	86	193	358	526	530	511	97	70	82	68	68	71	310
Zr	ppm	6	38	11	7	6	7	6	<6	<6	7	20	29	33	15	27	20	3.82

Table 9. PGE concentrations of the MG 1 chromitites.

Depth	Client ID	Au	Ir	Pd	Pt	Rh	Ru
	Units	ppb	ppb	ppb	ppb	ppb	ppb
314.86	MG 12	2.05	4.13	5.22	15.8	8.29	13.9
315.23	MG 17	3.02	70.5	90.3	369	133	304
315.3	MG 08+09	1.86	148	166	847	256	586
315.52	MG 11	5.99	124	162	569	190	520
315.9	MG 01	3.99	8.95	84.3	182	44.4	23.7
315.92	MG 02	1.44	0.94	6.05	11.6	1.4	2.5
316.2	MG 05	4.3	0.22	10.9	7.37	0.35	0.6

8.2 Mineral analyses

Table 10: MG 3 Chromite analysis.

Depths	Samples	SiO2	TiO2	Al2O3	Cr2O3	V2O3	Fe2O3	FeO	MnO	MgO	CaO	ZnO	NiO	Na2O	K2O	Total
291.88	43	0.02	1.23	7.06	58.79	0.59	0.26	27.69	0.37	4.04	0.05	0.11	0	0	0	100.21
292.43	44	0.01	1.35	7.27	57.49	0.37	1.37	27.18	0.23	4.46	0.07	0.11	0	0	0	99.91
292.45	45	0.01	1.37	7.56	55.56	0.33	2.85	26.91	0.36	4.55	0.02	0.12	0	0	0	99.64
292.47	46	0.01	1.21	10.02	56	0.34	0.55	25.5	0.28	5.74	0.03	0.1	0	0	0	99.78
292.71	21	0.48	0.93	15.79	53.75	0.36	0	19.2	0.26	8.68	0.01	0.07	0	0	0	99.53
292.87	23	0.01	0.9	15.25	54.96	0.34	0	20.08	0.25	8.21	0	0.06	0	0	0	100.06
292.93	25	0.01	0.91	15.57	50.38	0.31	2.89	23.47	0.27	7.86	0	0.16	0	0	0	101.83
293.16	27b	0.01	0.77	16.34	52.95	0.31	0	21.11	0.3	8.15	0.03	0.07	0	0	0	100.04
293.48	28	0.01	1.16	14.06	54.27	0.45	0	22.47	0.28	7.51	0.01	0.07	0	0	0	100.29
293.7	32	0.02	0.88	13.93	53.19	0.3	0.33	23.7	0.29	7.18	0.02	0.07	0	0	0	99.91
293.73	33	0.02	1.21	10.59	54.65	0.51	1.79	25.49	0.32	5.99	0.03	0.05	0	0	0	100.65

Table 11: MG 3 plagioclase analysis.

Depths	Samples	Normalized	SiO2	Al2O3	MgO	CaO	MnO	FeO	Na2O	K2O	Total	Cations O=8	Si	Al	Mg	Ca	Mn	Fe	Ba	Na	K	Total
291.88	43		49.07622	32.13529	0.020191822	15.76981	0.010096	0.302877	2.523978	0.161535	100		2.247327	1.734334	0.001378	0.773712	0.000392	0.011599	0	0.224093	0.009437	5.002271
292.43	44		48.95465	31.99677	0.020199998	16.07918	0.0202	0.2323	2.524997	0.1717	100		2.244323	1.728833	0.001381	0.789793	0.000784	0.008906	0	0.224 44	0.010042	5.008501
292.45	45		49.04561	31.78622	0.030138638	16.14426	0.010046	0.210 97	2.561784	0.210 97	100		2.249414	1.718161	0.002061	0.793314	0.000 39	0.008092	0	0.227803	0.012344	5.011579
292.47	46		49.04265	32.24597	0.020261372	15.79374	0.020261	0.263398	2.431365	0.182352	100		2.245103	1.739777	0.001383	0.774649	0.000786	0.010084	0	0.215804	0.010 65	4.998235
292.71	21		50.34979	31.54108	0.009994004	14.64122	0.009994	0.199 88	3.078153	0.169898	100		2.296 07	1.695195	0.000679	0.715356	0.000386	0.007623	0	0.272 16	0.009884	4.997354

Depths	Samples	Normalized	SiO2	Al2O3	MgO	CaO	MnO	FeO	Na2O	K2O	Total	Cations O=8	Si	Al	Mg	Ca	Mn	Fe	Ba	Na	K	Total
292.87	23		50.3789	31.54491	0.010104072	14.69132	0.010104	0.202081	2.970597	0.191977	100		2.296997	1.695106	0.000687	0.71679	0.00039	0.007705	0	0.262605	0.011167	4.992336
292.9	24		50.50698	30.97079	0.040156611	14.83787	0.010039	0.250979	3.132216	0.250979	100		2.307069	1.667313	0.002734	0.72617	0.000388	0.009587	0	0.277401	0.014625	5.005288
292.93	25		50.92802	30.57056	0.019640577	14.82864	0.019641	0.196406	3.132672	0.304429	100		2.325092	1.644911	0.001337	0.72534	0.000759	0.007499	0	0.277297	0.017731	4.999967
293.16	27b		49.7733	31.51637	0.141057935	15.35516	0.010076	0.342569	2.629723	0.231738	100		2.276428	1.698828	0.009618	0.75243	0.00039	0.013103	0	0.233192	0.013521	4.997515
293.48	28		51.36309	30.74515	0.020193861	13.79241	0.010097	0.201939	3.735864	0.13126	100		2.337747	1.649221	0.00137	0.67258	0.000389	0.007686	0	0.329674	0.007621	5.00629
293.55	30		49.52821	31.73058	0.020077629	15.51897	0.010038	0.260992	2.780566	0.150572	100		2.266386	1.711256	0.00137	0.76085	0.000389	0.009988	0	0.246696	0.00879	5.005729
293.7	32		49.32645	31.88494	0.010128634	15.56771	0.010129	0.253216	2.785374	0.162058	100		2.258286	1.720443	0.000691	0.76327	0.000393	0.009695	0	0.247246	0.009465	5.009848
293.73	33		48.84428	32.26886	0.030413625	15.96715	0.020276	0.273723	2.43309	0.162206	100		2.238044	1.742586	0.002077	0.78386	0.000787	0.010489	0	0.216152	0.009482	5.00348
295	38		48.60687	32.27578	0.030506406	16.12772	0.020338	0.366077	2.46085	0.111857	100		2.229955	1.745142	0.002086	0.79273	0.00079	0.014045	0	0.218892	0.006547	5.010194

Table 12: MG 3 pyroxene analysis.

Depths	Samples	SiO2	TiO2	Al2O3	Cr2O3	Fe2O3	MgO	CaO	MnO	FeO	Na2O	K2O	Summe:	Cations O=6	Si	Ti	Al	Cr	Mg	Ca	Mn	Fe2	Na	K	Total
291.88	43	53.9255	0.15125	1.0255	0.35175	0	28.95925	0.916	0.161	13.8695	0.01075	0.011	99.3815		1.946686	0.004106024	0.043631	0.01004	1.558209	0.035429	0.004923	0.418719	0.000752	0.000507	4.023002
292.43	44	54.06	0.16	1.09	0.36	0	29.16	1.02	0.2	13.33	0.01	0.01	99.4		1.94689	0.00433321	0.046265	0.010251	1.565271	0.039357	0.006101	0.401472	0.000698	0.000459	4.021098
292.45	45	54.76	0.16	1.14	0.401	0	29.12	0.99	0.21	12.68	0.01	0.03	99.501		1.961235	0.004309339	0.048121	0.011355	1.554513	0.037989	0.006371	0.379791	0.000694	0.001371	4.00575
292.47	46	55.0147	0.1377	1.2561	0.3511	0	30.8283	0.9408	0.1593	11.3099	0.00535	0.0093	100.0126		1.948158	0.003666939	0.052424	0.00983	1.627165	0.035695	0.004778	0.334938	0.000367	0.00042	4.017442
292.71	21	56.26	0.11	1.56	0.39	0	33.32	0.56	0.08	8.78	0	0	101.06		1.944691	0.002859354	0.063553	0.010658	1.716693	0.02074	0.002342	0.253808	0	0	4.015344
292.87	23	55.25	0.1	1.48	0.32925	0	31.12	1.18	0.14	10.79	0.02	0	100.4093		1.944646	0.00264687	0.061395	0.009162	1.632618	0.044499	0.004174	0.317606	0.001365	0	4.018111
292.9	24	54.71	0.1	1.46	0	0	29.88	1.81	0.17	10.15	0.02	0	98.3		1.962348	0.002697328	0.061719	0	1.597448	0.069558	0.005165	0.304463	0.001391	0	4.00479

Depths	Samples	SiO2	TiO2	Al2O3	Cr2O3	Fe2O3	MgO	CaO	MnO	FeO	Na2O	K2O	Summe:	Cations O=6	Si	Ti	Al	Cr	Mg	Ca	Mn	Fe2	Na	K	Total
292.93	25	55.29	0.1	1.35	0.34	0	30.92	1.4	0.17	10.64	0.02	0	100.23		1.949479	0.0026 51528	0.0561	0.009478	1.62498	0.052888	0.005077	0.313742	0.001367	0	4.015764
293.06	27	56	0.1	1.54	0.28	0	32.67	0.59	0.13	9.02	0.03	0	100.36		1.951051	0.0026 20022	0.063236	0.007713	1.696549	0.022024	0.003836	0.262813	0.002027	0	4.011868
293.48	28	55.63	0.14	1.37	0	0	32.59	0.53	0.12	9.69	0.01	0	100.08		1.949065	0.0036 88668	0.056571	0	1.701917	0.019895	0.003561	0.283923	0.000679	0	4.019301
293.55	30	54.1404	0.1561	1.0198	0.1938	0	28.3274	1.2664	0.2008	14.7224	0.0337	0.0044	100.0652		1.949303	0.0042 26541	0.043275	0.005517	1.520202	0.048853	0.006124	0.443298	0.002353	0.000202	4.023352
293.7	32	55.91	0.1	1.39	0.1836	0	32.02	0.53	0.15	9.75	0.01	0	100.0436		1.959116	0.0026 35087	0.057404	0.005087	1.672356	0.019898	0.004452	0.285716	0.000679	0	4.007343
293.73	33	54.53344	0.120778	1.183778	0.275778	0	29.45533	1.349556	0.176667	12.84311	0.027222	0.011778	99.97744		1.948294	0.0032 44912	0.049845	0.00779	1.568528	0.051659	0.005346	0.383726	0.001886	0.000537	4.020855
295	38	52.78	0.21	1.03	0.284625	0	26.37	1.04	0.2	17.99	0.05	0.01	99.96463		1.934246	0.0057 87433	0.044488	0.008247	1.44042	0.040835	0.006208	0.551357	0.003553	0.000468	4.035609

Table 13: MG 1 chromite analysis.

Depth	Samples	SiO2	TiO2	Al2O3	Cr2O3	V2O3	Fe2O3	FeO	MnO	MgO	CaO	ZnO	NiO	Na2O	K2O	Total
315.03	14	0.03	1.42	15.09	53.21	0.19	0	24.36	0.24	5.66	0.02	0.05	0	0	0	100.27
315.11	15	0.03	1.57	13.81	52.88	0.22	0	25.86	0.34	5.02	0.02	0.09	0	0	0	99.84
315.27	8	0.02	0.95	15.41	56.64	0.28	0	17.85	0.3	9.29	0.01	0.05	0	0	0	100.8
315.52	11	0.02	0.8	15.24	57.11	0.28	0	18.67	0.29	9.16	0.01	0.04	0	0	0	101.62
316.16	5	0.03	1.65	9.49	55.03	0.66	0	29.34	0.34	3.26	0.01	0.08	0	0	0	99.89

Table 14: MG 1 plagioclase analysis.

Depth	Samples	SiO2	Normalized	SiO2	Al2O3	MgO	CaO	MnO	FeO	BaO	Na2O	K2O	Total	Cations O=8	Si	Al	Mg	Ca	Mn	Fe	Ba	Na	K	Total
315.03	14	50.73		50.88775	30.89578	0.030093289	14.43475	0.010031	0.160498	0	3.380479	0.200622	100		2.32029	1.660289	0.002046	0.705173	0.000387	0.00612	0	0.298851	0.011 67	5.004826
315.11	15	51.96		52.14773	30.0281	0.02007226	13.39823	0.010036	0.210759	0	3.944199	0.240867	100		2.371324	1.609307	0.001361	0.652771	0.000387	0.008015	0	0.347745	0.013973	5.004882
315.2	16	50.3		50.89548	30.97238	0.02023677	14.28716	0.030355	0.212486	0	3.440251	0.141657	100		2.319861	1.663845	0.001375	0.697728	0.001172	0.0081	0	0.304033	0.008237	5.004351
315.23	17	49.53		50.48415	31.1589	0.020385282	14.59586	0	0.132504	0	3.506268	0.101926	100		2.303946	1.675927	0.001387	0.713682	0	0.005057	0	0.310248	0.005934	5.016182
315.27	8	45.58		45.99395	34.30878	0.020181635	17.97175	0.010091	0.232089	0	1.442987	0.020182	100		2.120263	1.864017	0.001387	0.88764	0.000394	0.008947	0	0.128973	0.001187	5.012808
315.3	9	45.31		45.4099	34.47585	0.020044097	18.75125	0	0.320706	0	1.002205	0.020044	100		2.09817	1.877417	0.001381	0.928278	0	0.012392	0	0.089783	0.001182	5.008603
315.52	11	45.16		45.56094	34.49354	0.1109 76594	18.29096	0.010089	0.353107	0	1.170299	0.010089	100		2.103108	1.876 56	0.007637	0.904614	0.000394	0.013631	0	0.104 74	0.000594	5.011279
316.16	5	50.75		51.15412	30.82351	0.020159258	14.051	0.020159	0.191513	0	3.568189	0.171354	100		2.330087	1.654738	0.001369	0.685735	0.000778	0.007295	0	0.315128	0.009957	5.005087

Table 15: MG 1 pyroxene analysis.

Depth	Samples	SiO2	TiO2	Al2O3	Cr2O3	Fe2O3	MgO	CaO	MnO	FeO	Na2O	K2O	Summe:	Cations O=6	Si	Ti	Al	Cr	Fe3	Mg	Ca	Mn	Fe2	Na	K	Total
315.03	14	54.58725	0.12625	1.29275	0.37875	0	29.30575	1.82 05	0.14925	11.477	0.05275	0.00 75	99.19775		1.95523 9	0.00340067	0.05457 4	0.01072 6	0	1.56458 2	0.06986 5	0.00452 8	0.34379 3	0.00366 3	0.00034 3	4.01071 3
315.2	16	55.181	0.12788 9	1.07044 4	0.314	0	30.77067	1.22466 7	0.14044 4	11.33756	0.03578	0.00655 6	100.209		1.95175 7	0.00340167 9	0.04462 3	0.00878 1	0	1.62222	0.04641	0.00420 8	0.33536 3	0.00245 4	0.00029 6	4.01951 4
315.23	17	55.46015	0.09761 5	1.29407 7	0.32130 8	0	32.42515	0.89669 2	0.13661 5	8.87230 8	0.02315 4	0.01007 7	99.53715		1.95063 2	0.00258188 5	0.05364 3	0.00893 5	0	1.69985 9	0.03379 1	0.00407	0.26097	0.00157 9	0.00045 2	4.01651 3
315.27	8	55.75	0.12	1.32	0.36	0	32.94	1.16	0.11	7.93	0.02	0	99.71		1.95014 3	0.00315665 6	0.05442	0.00995 6	0	1.71744 2	0.04347 5	0.00325 9	0.23198 2	0.00135 6	0	4.01519
315.36	10	55.82073	0.11690 9	1.42627 3	0.41863 6	0	33.14936	0.64372 7	0.115	7.27527 3	0.01063 6	0.00218 2	98.97873		1.95715 7	0.00308249 8	0.05893 8	0.01160 5	0	1.73237 6	0.02418 2	0.00341 5	0.21332 4	0.00072 3	9.76E-05	4.00 49

Depth	Samples	SiO2	TiO2	Al2O3	Cr2O3	Fe2O3	MgO	CaO	MnO	FeO	Na2O	K2O	Summe:	Cations O=6	Si	Ti	Al	Cr	Fe3	Mg	Ca	Mn	Fe2	Na	K	Total
315.52	11	55.1	0.16	1.43	0.33	0	33.47	0.59	0.11	7.73	0	0	98.92		1.93971	0.00423575	0.05933	0.00918	0	1.75621	0.02254	0.00328	0.22757	0	0	4.02179
315.9	1	54.49246	0.15361	1.46223	0.32015	0	30.60277	0.90738	0.12438	10.73869	0.01646	0.00953	98.82769		1.94760	0.00412880	0.06159	0.00904	0	1.63028	0.03474	0.00376	0.32097	0.00114	0.00043	4.01372
315.92	2	54.50429	0.16457	0.81242	0.28328	0	29.23423	1.20242	0.12785	13.43757	0.03842	0.011	99.80529		1.95136	0.00443940	0.03434	0.00803	0	1.56247	0.04621	0.00388	0.40311	0.00267	0.00050	4.02082
316.11	4	54.774	0.22263	0.85881	0.27545	0	29.21536	1.32963	0.16927	13.76936	0.03045	0.01054	100.6555		1.95164	0.00596550	0.03606	0.00776	0	1.55158	0.05076	0.00510	0.41029	0.00210	0.00047	4.02176
316.16	5	54.59325	0.18262	1.01275	0.3155	0	29.15238	1.40412	0.163	13.27913	0.02062	0.00775	100.1311		1.95149	0.00490922	0.04267	0.00897	0	1.55324	0.05377	0.00493	0.39697	0.00142	0.00035	4.01869